

REPORT DOCUMENTATION PAGE

AFRL-SR-AR-TR-05-

The public reporting burden for this collection of information is estimated to average 1 hour per response, including gathering and maintaining the data needed, and completing and reviewing the collection of information. Send comments regarding this burden estimate or any other aspect of this collection of information, including suggestions for reducing the burden, to Department of Defense, Washington Headquarters (0704-0188), 1215 Jefferson Davis Highway, Suite 1204, Arlington, VA 22202-4302. Respondents should be aware that any person who provides false or misleading information may be subject to criminal sanctions (including fines and imprisonment) and/or civil sanctions (5 U.S.C. 552a).
PLEASE DO NOT RETURN YOUR FORM TO THE ABOVE ADDRESS.

0017

es,
tion
orts
ill be

1. REPORT DATE (DD-MM-YYYY) 12142004		2. REPORT TYPE Final Report		3. DATES COVERED (From - To) 15 Dec 2002 - 14 Dec 2004	
4. TITLE AND SUBTITLE High-Temperature, High-Bandwidth Fiber Optic Pressure and Temperature Sensors for Gas Turbine Applications				5a. CONTRACT NUMBER	
				5b. GRANT NUMBER F49620-03-C-0010	
				5c. PROGRAM ELEMENT NUMBER	
				5d. PROJECT NUMBER	
6. AUTHOR(S) Robert Fielder				5e. TASK NUMBER	
				5f. WORK UNIT NUMBER	
7. PERFORMING ORGANIZATION NAME(S) AND ADDRESS(ES) Luna Innovations Incorporated 2851 Commerce Street Blacksburg VA 24060				8. PERFORMING ORGANIZATION REPORT NUMBER	
9. SPONSORING/MONITORING AGENCY NAME(S) AND ADDRESS(ES) USAF/AFRL AFOSR 801 N. Randolph Street Arlington VA 22203 NA				10. SPONSOR/MONITOR'S ACRONYM(S) AFOSR	
				11. SPONSOR/MONITOR'S REPORT NUMBER(S)	
12. DISTRIBUTION/AVAILABILITY STATEMENT Distribution Statement A. Approved for public release; distribution is unlimited.					
13. SUPPLEMENTARY NOTES					
14. ABSTRACT This technical report summarizes the R&D effort for the Phase II STTR program titled "High-Temperature, High-Bandwidth Fiber Optic Pressure and Temperature Sensors for Gas Turbine Applications". Luna Innovations and Virginia Polytechnic Institute and State University (Virginia Tech or VT) have teamed together for this effort. This research program has developed accurate and reliable pressure and temperature instrumentation that can operate within extremely high-temperature combusting flows. The sensors developed during this project has been tested in a gas turbine engine measuring the pressure differentials that occur as the turbine blades rotate during operation.					
15. SUBJECT TERMS					
16. SECURITY CLASSIFICATION OF:			17. LIMITATION OF ABSTRACT	18. NUMBER OF PAGES 104	19a. NAME OF RESPONSIBLE PERSON
a. REPORT	b. ABSTRACT	c. THIS PAGE			19b. TELEPHONE NUMBER (Include area code)
UU	UU	UU	UU		

20050125 138

RECEIVED DEC 21 2004

High-Temperature, High-Bandwidth Fiber Optic Pressure and Temperature Sensors for Gas Turbine Applications

Phase II Air Force STTR – Draft Final Report
Contract #: F49620-03-C-0010

To: Dr. Thomas Beutner
AFOSR/NA
4015 Wilson Blvd., Room 713
Arlington, VA 22203

Reporting Period: 9.2.02 – 12.14.04

Date: 12.14.04

Principle Investigator: Robert Fielder

Prepared by: Robert Fielder, Matthew Palmer, Dr. Wing Ng, Matthew Davis, Aditya
Ringshia, Bo Song

Luna Innovations Incorporated
2851 Commerce St.
Blacksburg, VA 24060



1. Table of Contents

1. Table of Contents	2
2. Executive Summary	3
3. Sensor Operation and Demodulation	3
3.1 Fiber Optic Sensing System Operation	3
4. First Generation Sensor Design and Development	22
4.2 Active Cooling System	24
4.3 High Temperature Bonding Methods	28
4.4 First Generation Testing	32
4.5 High Temperature Testing	37
Test Results	39
5. Second Generation Sensor Design and Development	51
5.1 Sensor Operation	52
5.2 Development of the Fused Ferrule Design	75
5.3 Material selection	78
5.4 Related Work: Optical Fiber High Temperature Survivability	79
6. Sensor Construction Procedures and Challenges	80
6.1 Hermetic testing	80
6.2 Welding development	81
6.3 Sensor Construction	83
7. Sensor Testing	86
7.1 Fiber Optic Pressure Sensor Engine Testing	95
7.2 Results	96
7.3 Second fiber optic pressure sensor testing	97
8. Conclusion	104

2. Executive Summary

This technical report summarizes the R&D effort for the Phase II STTR program titled "High-Temperature, High-Bandwidth Fiber Optic Pressure and Temperature Sensors for Gas Turbine Applications". Luna Innovations and Virginia Polytechnic Institute and State University (Virginia Tech or VT) have teamed together for this effort. This research program has developed accurate and reliable pressure and temperature instrumentation that can operate within extremely high-temperature combusting flows. The sensors developed during this project have been tested in a gas turbine engine measuring the pressure differentials that occur as the turbine blades rotate during operation.

During this SBIR Phase II STTR development effort the following specific tasks were accomplished:

- High-temperature pressure sensors were constructed and tested,
- High-temperature ceramic-metal bonds were performed and tested,
- High-temperature fiber to housing construction methods were developed and tested,
- Generation 2 (or gen2) sensors were constructed to test assembly procedure and bond resistance to thermal cycling,
- A Hyperscan dual-wavelength fiber-optic sensor instrumentation system was used during sensor calibration and engine testing,
- The VT Pratt and Whitney JT-15D-1 engine turbine blade ports were interrogated with Luna Instrumentation, and
- Compressor blade passing frequency was measured with the Hyperscan system and a fiber-optic pressure sensor with a Sapphire diaphragm.

3. Sensor Operation and Demodulation

Two generations of high temperature pressure sensing probes were developed under this program. The first generation development led to improved high temperature bonding methods and the introduction of an active cooling method to allow for the sensor to survive in environments that exceeded the material capabilities of the sensor components. These developments led to a second generation fiber optic pressure sensor which incorporated and refined the methods and developments realized during the first generation experiments. The second generation high temperature pressure sensor was ultimately used for measuring pressure fluctuations in between the first and second stage turbines in a Pratt & Whitney JT-15D-1 gas turbine engine.

3.1 Fiber Optic Sensing System Operation

The high temperature pressure sensor is designed to interpret very slight pressure changes in a surrounding environment at a high sampling frequency. This sensor uses a sapphire diaphragm to translate the pressure changes into a proportional deflection of the diaphragm face. The

Hyperscan system then interprets this deflection into pressure measurements through the use and demodulation of two independent laser sources passed through the optical fiber.

3.1.1 Luna Innovations Fiber Optic Sensors

Luna Innovations has many patents and much experience with respect to fiber-optic sensors and sensing techniques. The sensor developed for this program is based on one of Luna's patented technologies, Extrinsic Fabry Perot Interferometry (EFPI).^{1,2} EFPI-based sensors use a distance measurement technique based on the formation of a low-finesse Fabry-Perot cavity between the polished end face of a fiber and a reflective surface, shown schematically in Figure 1. In the case of the pressure sensor, there is a thin (typically 30-150 μ m) air gap between the end of the fiber and reflective surface that moves with changes in pressure. Light is passed through the fiber, where a portion of the light is reflected at the fiber/chip interface (R1). The remaining light propagates through the chip and is reflected back into the fiber from the chip/air interface (R2). These two light waves interfere constructively or destructively based on the path length difference traversed by each. In other words, the pressure-dependent path length through the air gap modulates the interaction between the two light waves. The resulting light signal then travels back through the fiber to a detector where the signal is processed to produce a measurement. Several different methods exist to process the return signal.

Typical EFPI readout systems operate at a near-infrared wavelength of around 830 nm. The choice of this wavelength region was driven primarily by cost and availability of components. The source is typically a broadband super luminescent diode (SLD), with a wavelength bandwidth of around 50-80 nm. The return signal is generally analyzed using a grating spectrometer, which uses a grating to disperse the wavelengths in the incoming signal across a linear silicon charge-coupled device (CCD) photodiode array. The spectrum is then read from the CCD array, with each pixel detecting light in a narrow wavelength region.

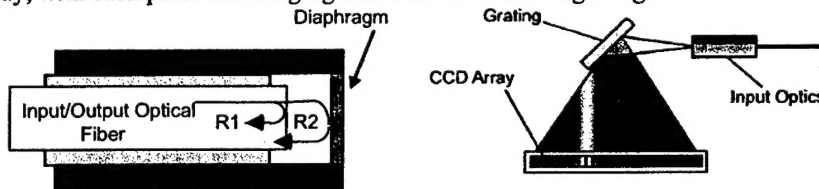


Figure 1. Extrinsic Fabry-Perot Interferometer concept (left) and Grating spectrometer arrangement (right).

¹ Murphy et al., *Extrinsic Fiber Optic Displacement Sensors and Displacement Sensing Systems*, United States Patent #5,301,001

² Murphy, K., Gunther, M., Vengsarkar, A., and Claus, R., "Quadrature phase-shifted, extrinsic Fabry-Perot optical fiber sensors," *Optics Letters*, Vol. 16, No.4, February 1991, pp. 273-275

3.1.2 High Speed Method of Demodulation

A single wavelength demodulation system, shown conceptually in Figure 2, has a sinusoidal transfer function. The main disadvantages of this approach are the non-linear transfer function and directional ambiguity of the sinusoidal output. As shown in Figure 3, if the transducer changes occur at a peak or valley in the sinusoid (π , 2π , 3π , ...), the change will not be detected because the slope of the transfer function is zero at those points. The sensitivity of the system correspondingly decreases to zero at points near multiples of π . If the direction of diaphragm of a pressure sensor movement changes at a peak or valley, that information is lost. This causes directional ambiguity in the signal.

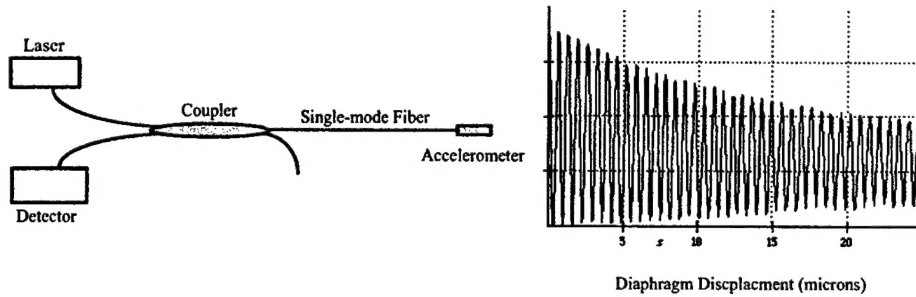


Figure 2: Simple single wavelength optical sensor demodulation system.

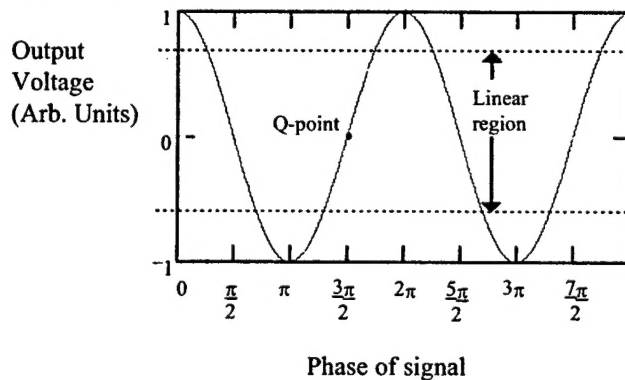


Figure 3: Interferometric signal output.

One approach to solving the aforementioned problems is to design the sensor head so that the signal does not exceed the linear region of the transfer function (Figure 3) for the full scale of the sensor. This places difficult manufacturing constraints on the sensor head by requiring the initial optical path length to be positioned at the Q-point of the transfer function curve, and limits the operational range of the sensor.

To solve the non-linear transfer function and directional ambiguity problems, Luna Innovations has developed the Hyperscan instrumentation system, a dual wavelength demodulation system [i]. Example dual wavelength architecture is shown in Figure 4. The design utilizes two quadrature optic channels to provide unambiguous, accurate, high frequency measurements. Two lasers of appropriate output wavelength are selected to generate quadrature phase shifted signals for a given sensor air gap. A quadrature signal is defined as two signals that are ninety degrees out of phase.

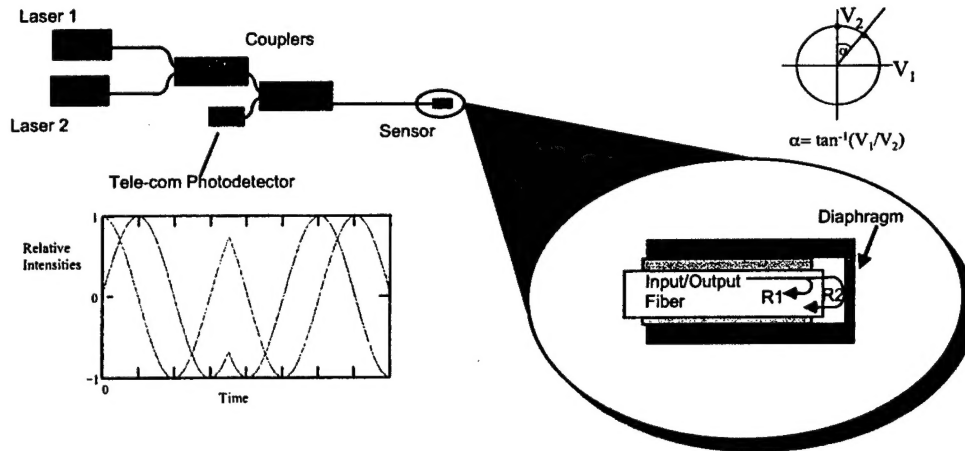


Figure 4: Two wavelength EFPI sensor interrogation.

Figure 5 shows a theoretical plot of the reflected intensities that can be obtained with this system. As seen from the graph, when one signal is at a peak or valley, the other signal is in the linear region. In this way, one signal always has a linear response with the change in gap. By monitoring the phase lead/lag relationship between the signals, the direction of gap movement is unambiguously determined. An output showing the phase lead/lag relationship at a direction change, or turnaround, is shown in Figure 6.

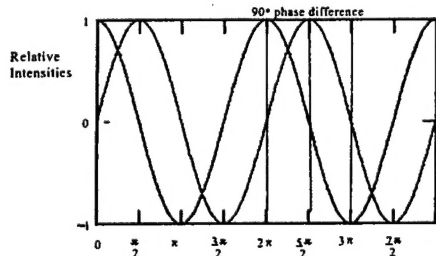


Figure 5: Theoretical outputs of quadrature signals obtained from a dual wavelength system.

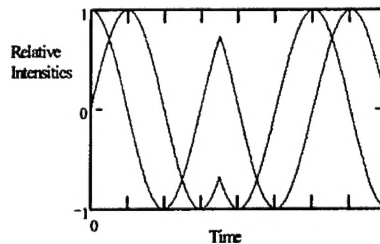


Figure 6: Two wavelength system theoretical output showing the phase relationship at a direction change.

Figure 7 shows a simulated sinusoidal disturbance to an EFPI sensor. Figure 8 shows the corresponding response of both of the quadrature signals as would be received by the optical detector.

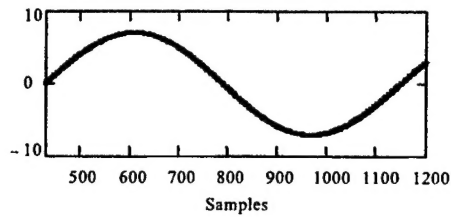


Figure 7: Sinusoidal perturbation of the EFPI sensor.

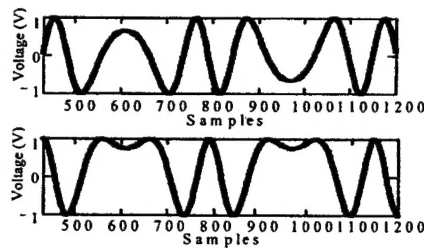


Figure 8: Quadratic response from two wavelengths.

As the perturbation drives the sensor through a quadratic fringe, the Lissajous plot traces a revolution on the circle in Figure 9. One revolution around the circle is the equivalent to going through one “fringe”, and by tracking the perturbation around the circle one can track the change in gap. The perturbation is tracked around the circle by monitoring the change in α , which is given by the arctangent of V_1/V_2 .

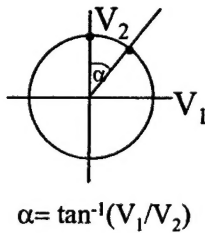


Figure 9: Lissajous plot from the two wavelengths.

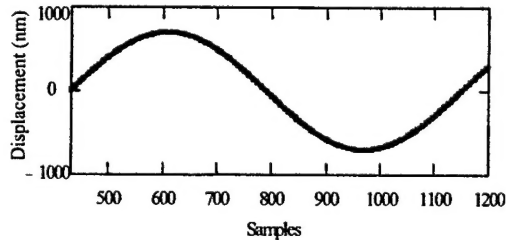


Figure 10: Sinusoidal perturbation as measured by two-wavelength measurement system.

3.1.3 Hyperscan Specifications

The Hyperscan system uses two lasers at wavelengths of 1541.4 and 1546.1 nm to generate two optical signals that are 90 degrees out of phase with each other, called quadrature for an air gap of approximately 62.5 μ m. The two laser wavelengths are separated temporally by switching the lasers on and off alternately, so that only one laser is on at a time allowing for the capture of the sensor response to each laser wavelength separately. The lasers are switched on and off at least 3 times as fast as the fastest expected change in the sensing system. The optical signals are then received by a single PIN diode and amplified. The optical signals from the sensor in response to both lasers are output on the same electrical connection alternatively. A clock signal is also generated and available on another front panel connection for synchronization of the data acquisition. Figure 11 illustrates the block diagram of the system.

After the data is collected by the user's data system, the software separates the two signals and converts the data to gap change. The conversion utilizes normalizing math, trigonometry, logic and transforms.

The sample speed is adjustable from 5,000 to 1 Million samples/second (8 selections). A full "fringe" is normally required for the post processing algorithm to convert the optical signal into gap change, so therefore the system frequency response can be defined as up to 333,333 fringes/second. Such a gap change is equivalent to a 257,250 $\mu\text{m}/\text{second}$ velocity. In relation to sensor design, a 1000 psi full scale sensor can be designed for 2 fringes of full scale range. Therefore, the sensor will be able to resolve changes of 0 to 1000 psi at a frequency of 167kHz.

An assembly drawing of the Hyperscan is shown in Figure 15. This system has been designed to fit into a standard rack mount chassis already utilized by Luna. Figure 16 is a Photograph of the completed electronics board. The prototype has been completed and is shown in Figure 13. The factory set-up and test procedures have been developed for this system. All electrical and optical circuits passed these tests. Figure 17 shows a detailed schematic for this system. The lasers and laser driver used in this system is shown in Figure 14. There are 4 optical channels, with a separate gain and offset setting for each channel. There are two modes of operation. Not only is the dual-wavelength mode of operation possible, but a single-wavelength mode of operation is also available. The single wavelength mode will enable the most flexibility for utilizing sensors for measurements that do not generate a full fringe.

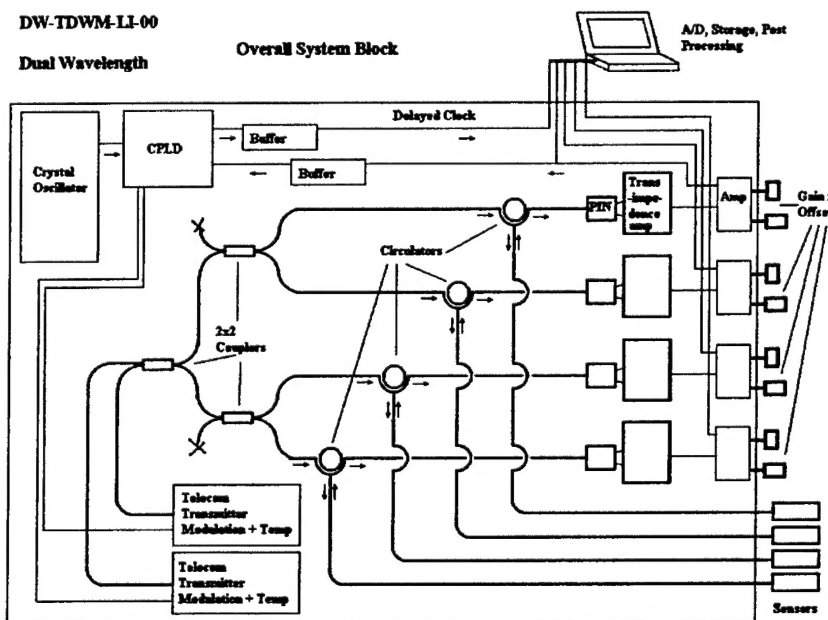


Figure 11: Hyperscan system block diagram.

3.1.4 Hyperscan Construction

A prototype has been constructed with adjustable sampling speed and adjustable gain to sample 4 optical channels simultaneously for this development program. Figure 12 shows the electronics for this program under construction as well as the mechanical assembly.

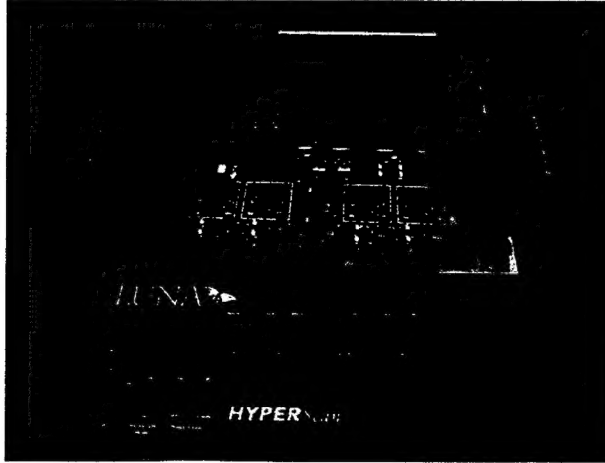


Figure 12: Dual-wavelength prototype instrumentation.

Factory set-up and test procedures for this system were completed for both the optical and electrical circuits after construction was completed. The pc used for data capture is also shown in Figure 13. This system was used with the pressure sensors during this development effort.

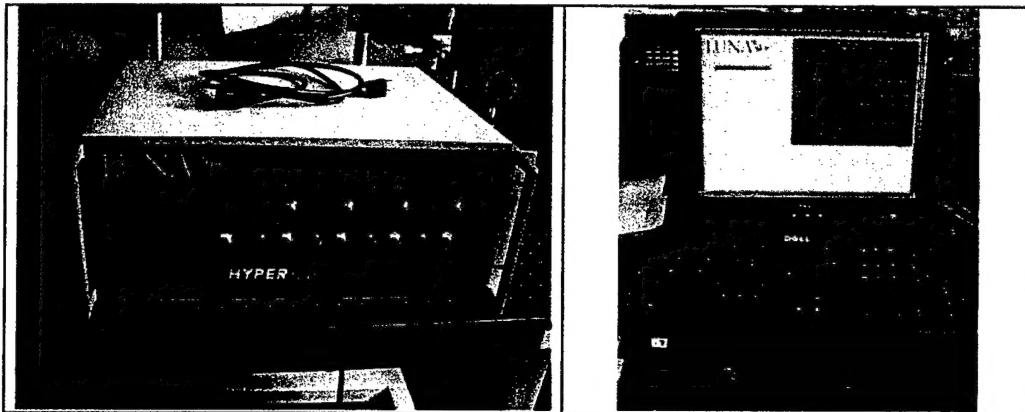


Figure 13: Hyperscan system (left) and data collection pc (right).

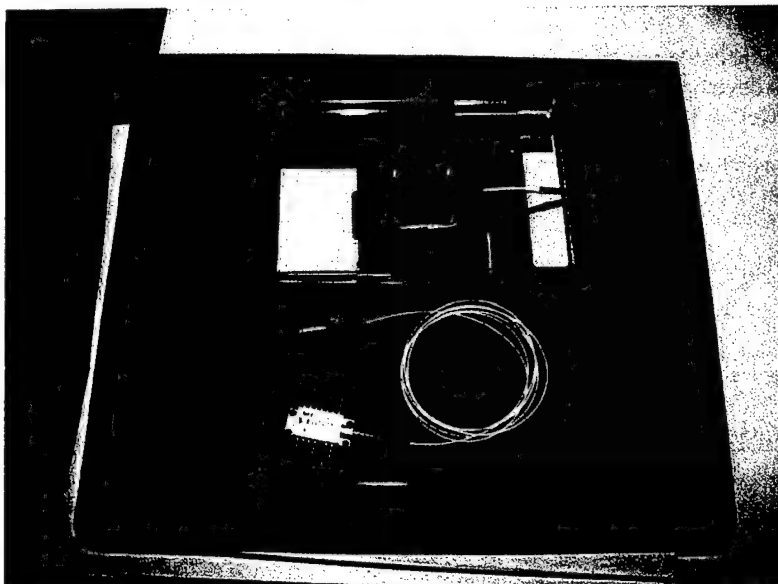


Figure 14: Laser and driver circuit.

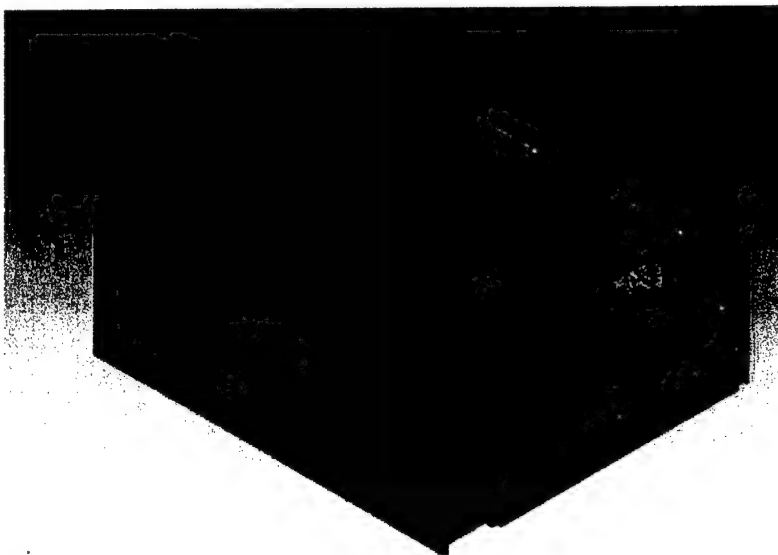


Figure 15: Hyperscan assembly drawing (dual wavelength system).

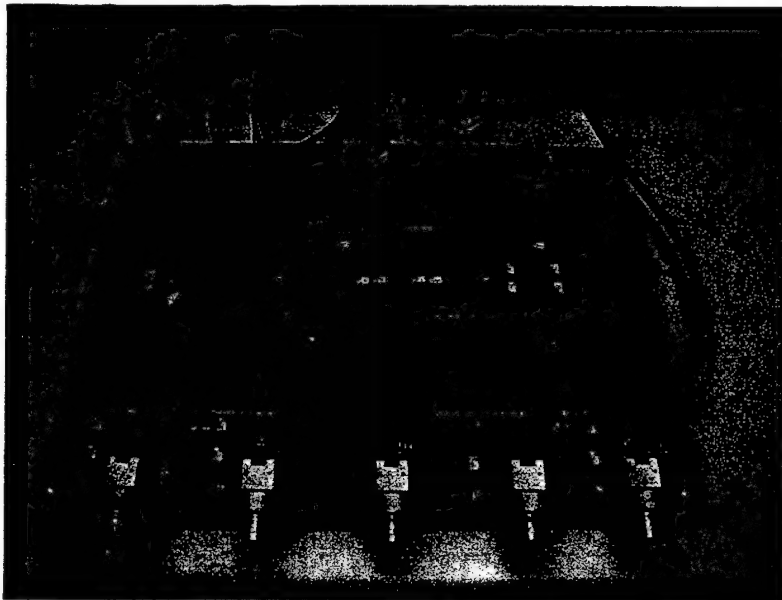


Figure 16: HyperScan electronics circuit board.



Figure 17: Detailed schematic of one channel of the Hyperscan system. All channels are identical.

3.1.5 Software Development

During the development of the Hyperscan system on another program, software was developed for post processing the data captured from the sensors. A series of screen captures are shown in Figure 18, Figure 19, Figure 20, and Figure 21. The software is designed to process data from a data from a comma separated value (*.csv) text file. The software allows processing the data with or without a calibration file. A calibration file is necessary if the data captured during the measurement does not contain a full fringe as illustrated in Figure 19. As the system cannot ascertain the starting absolute gap of the sensor, the processed data is always normalized such that the sensor gap is zero at the beginning of the test.

As shown in Figure 20, the two sinusoidal signals returned from the optical fiber sensor (Figure 18) are transformed from a noisy ellipse (shown in Figure 19) to a clean unit circle. The unit circle facilitates the conversion of the optical signal to gap change by use of an algorithm that utilizes an arctangent. The sensor gap change is calculated and displayed by the software. The software allows saving of the sensor data in comma separated variable format (*.csv) for direct import into standard data manipulation programs.

The software also enables the processing of sensor data when the sensor has not moved through a single fringe. This is enabled by saving of a calibration file containing parameters needed to convert the data to a portion of a unit circle. The calibration file must be generated from a data set captured while the sensor is manipulated to move through a full fringe. This technique was used to process some of the data reported in the sensor specific portions of this report. At this point in the development of the software, the offset and gain settings for a sensor cannot be changed between a calibration of the sensor and the actual measurement, as this will adversely affect the sensor measurement.

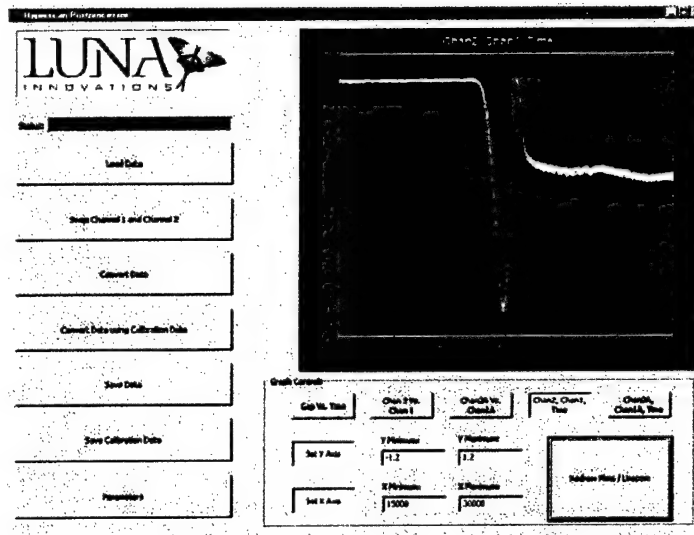


Figure 18: Sensor data for Laser 1 and Laser 2 vs. time showing the sinusoidal shapes and the phase relationship (quadrature).

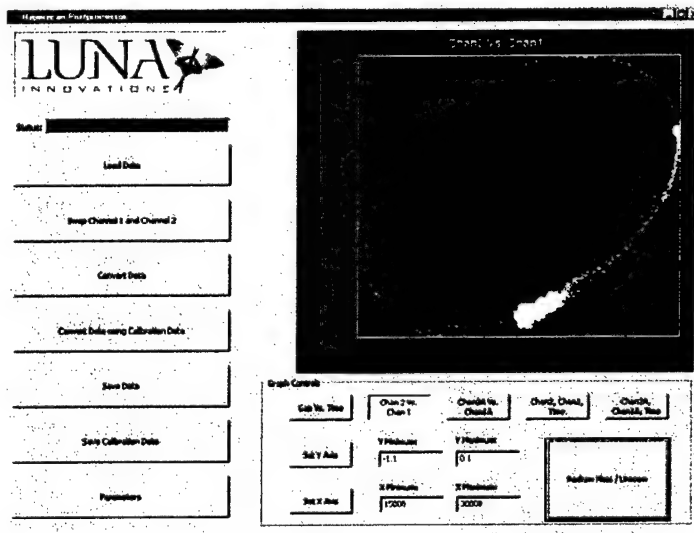


Figure 19: Sensor data from Laser 2 plotted vs. Laser 1 data, showing the elliptical shape of a single fringe.

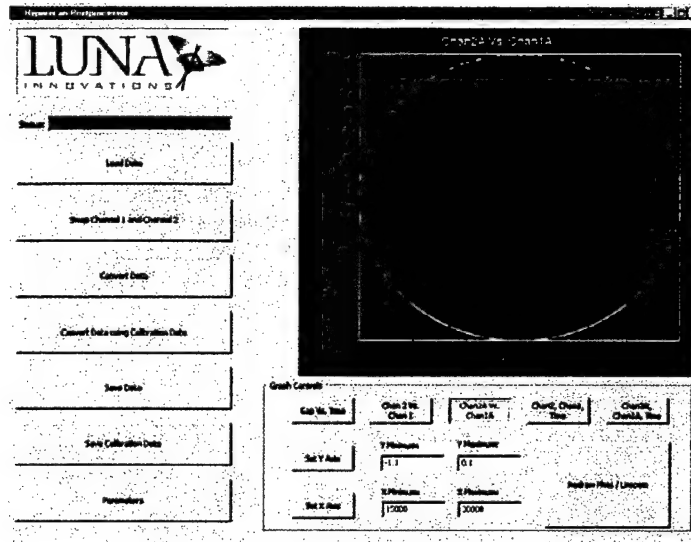


Figure 20: Data transformed to a unit circle.

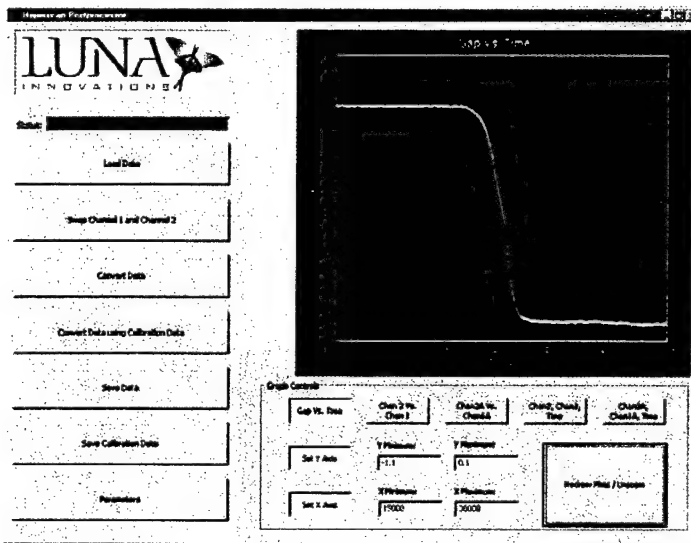


Figure 21: Calculated sensor gap change.

3.1.6 Hyperscan Testing (Related Work)

Prototype System Testing

To test the performance of the pre-alpha prototype leading to the Hyperscan development, the Luna researchers piggy-backed a test performed by the U.S. Navy during the development, again on another program. The Luna team instrumented the structure with a fiber optic strain gage near a foil gage for direct comparison, as shown in Figure 22 for shock testing a structure by an underwater explosion. Figure 23 shows the actual test in progress.

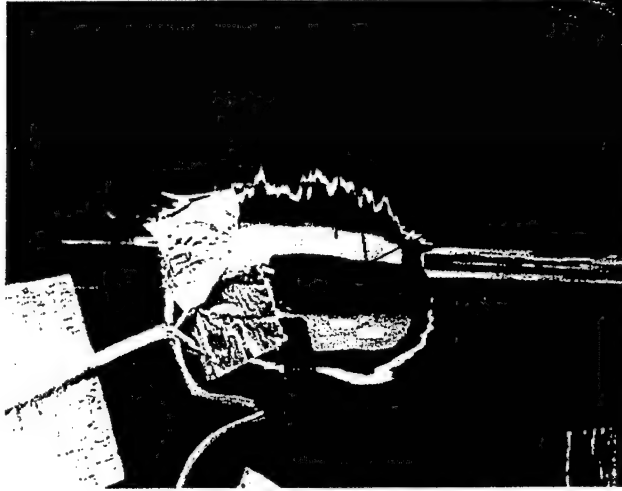


Figure 22: Sensor implementation.

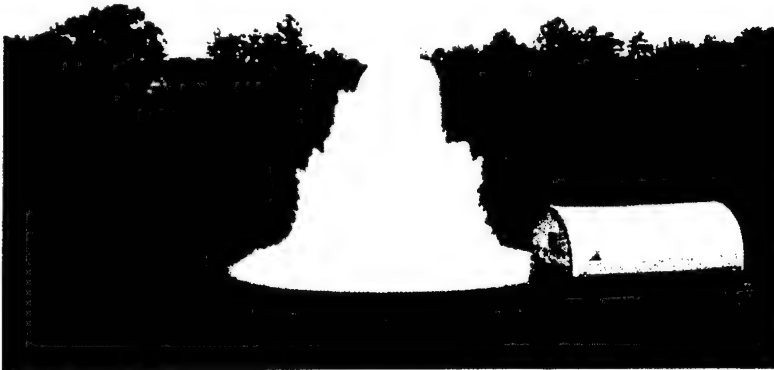


Figure 23: Shock test.

Luna captured data at 100kHz with two systems, a FOSS-1 commercial optical fiber strain measurement system, which requires significant effort to reduce the data, and the prototype

system. The data is presented in Figure 24 and Figure 25. The Hyperscan prototype system performed very well, comparing very well with the two proven measurement systems (Foil gage and FOSS-1 system). As shown in Figure 24, the prototype system had much lower noise content in the signal than the foil gage and did not show any sensitivity to the electrical pulse used to detonate the charge at -0.02s, nor the anomaly at 0.28s captured by the foil gage. This reiterates the advantages of fiber over electrical gages in EMI resistance. In addition, Figure 25 shows that the unfiltered data from the prototype system and fiber response (Dual Wavelength, red trace) is much cleaner than the foil gage (blue trace) even after the foil gage is filtered with a 250Hz low pass filter. In comparison, the FOSS-1 data (Fabry-Perot, pink trace) is not as accurate as the foil gage for the same test.

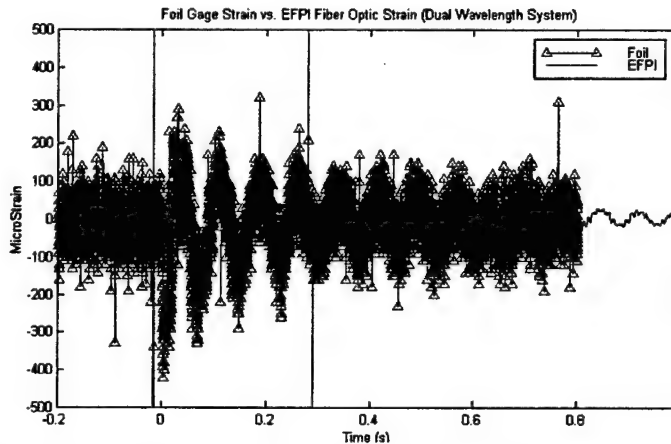


Figure 24: Comparison of unfiltered responses of foil gage and prototype system with fiber optic strain gage.

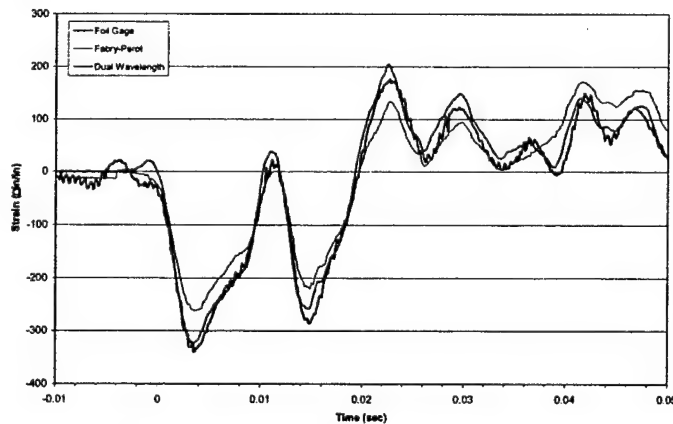


Figure 25: Comparison of filtered foil gage response to fiber gages monitored with foss-1 system and prototype system.

3.1.7 Error Estimation

To ascertain the error in gap measurement made by the Hyperscan system, an experiment was designed to test the drift and error in the voltage output over a 97 hour period. The results of the testing is shown in Figure 26. The average error in the measurement over the 97 hour period is approximately 0.018 volts, peak to peak (p-p). To assess effect of the voltage error in the calculation of the sensor change, a series of simulated data sets were generated with 0.018vp-p random noise. The data sets simulated a linear sensor change with a full dynamic range from 1 μm to 21 μm . The error was then calculated as the difference between the change in sensor gap calculated by the Hyperscan post-processing software, and the gap change input into the data simulation. Figure 27 shows the maximum error in terms of direct error in μm , and in terms of error relative to the full scale range of the measurement (%FS).

The system error is good considering the interrogation speed. The error seems to be optimal when the full scale of the sensor is near 7-8 μm of gap change. This equates to approximately 10 "fringes". Unfortunately, the sensor algorithm does not have the capability to discern one fringe from another. Therefore, once a sensor moves past one fringe, the algorithm cannot tell which fringe the sensor is on. Therefore, to ensure that the prototype sensor is capable of making absolute pressure measurements for the Air Force needs, the sensor's full scale range must be limited to one fringe or less. These requirements and the system limitations therefore limit the sensor accuracy to 1.6% FS, which equates to about 100 psi in the 2nd generation sensor design for the VT P&W JT-15D-1 engine test..

The error calculation assumes that the sensor optical output is too large for the next gain setting, limiting the Hyperscan output to 0.83 volts fullscale before clipping. As can be seen in the data, the absolute error in the gap change measurement increases as a linear function with respect to number of "fringes" of the sensor measurement. However, the increase in resolution enabled by multiple fringes actually enables a decrease in %FS error, also shown in Figure 27. The increase in error is due to the operation of the post processing algorithm. As the number of fringes increases, the variability of the shape of each fringe increases the error in the calculated gap change. This change in shape can be seen in Figure 28 and Figure 29 for sensor gap changes of 3.9 and 14.1 fringes.

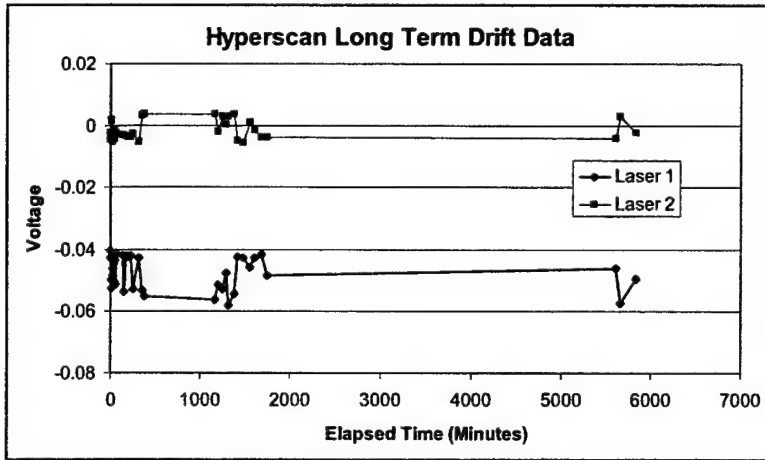


Figure 26: Hyperscan drift data.

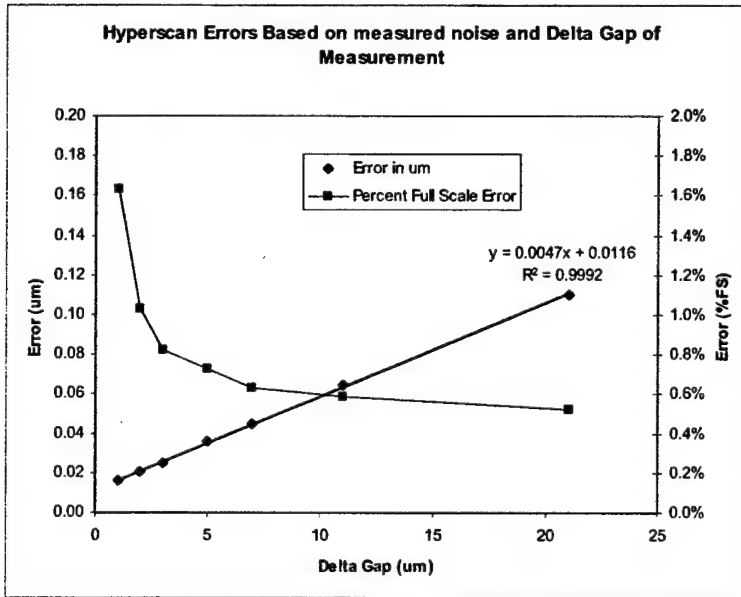


Figure 27: Error estimated for various full-scale gap changes from 1µm to 21µm.

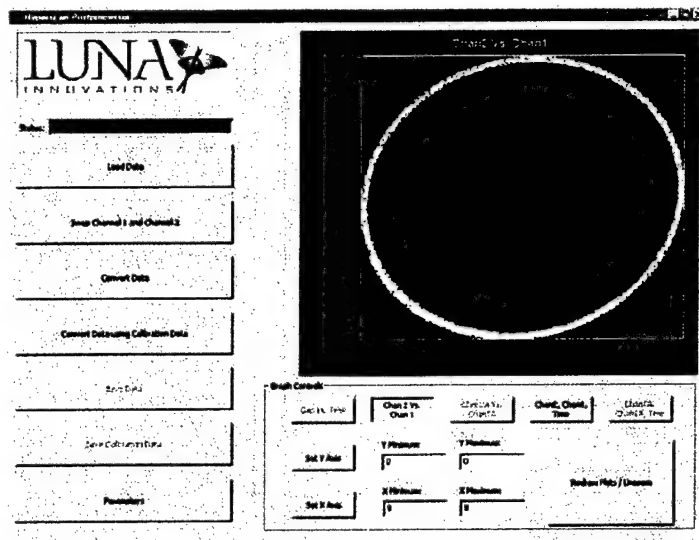


Figure 28: Lissajous plot for 3um of gap change (3.9 fringes), simulated data.

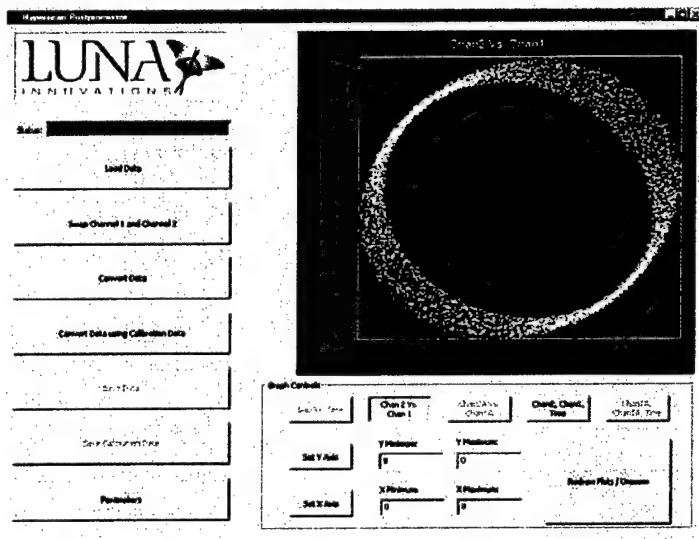


Figure 29: Lissajous plot for 11um of gap change (14.1 fringes), simulated data.

3.1.7.1 Hyperscan Pressure Testing

In addition to the sensor data collected on this program, the Luna Innovations researchers have collected high speed data from a variety of medium temperature sensors on other development programs. Figure 30 shows data collected from the calibration of a fused EFPI pressure sensor to 625psi.

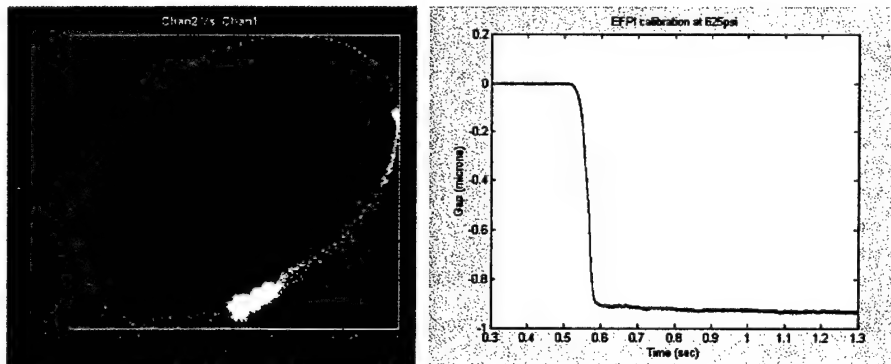


Figure 30: Ellipse formed by the two wavelength optical returns from the efpi sensor during 625psi calibration (from postprocessing software, left) and calculated sensor gap change for EFPI sensor during 625psi calibration (right).

4. First Generation Sensor Design and Development

The design of the first generation of high temperature pressure sensors was based on a similar, lower temperature design developed previously at Luna Innovations. This design (shown in Figure 31) was capable of measuring pressures at 850°C.

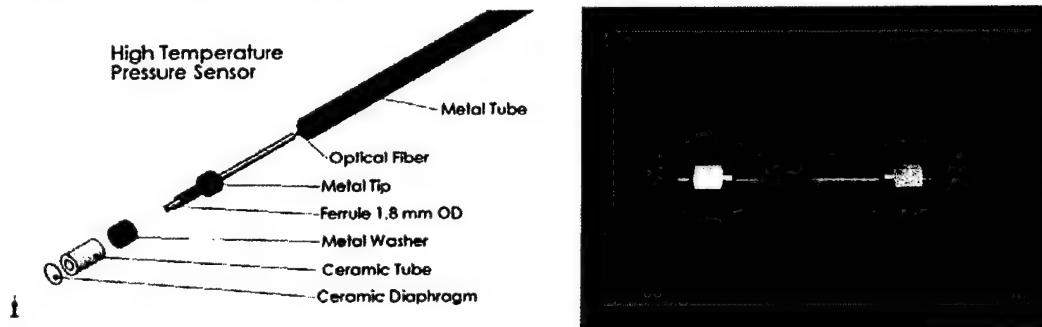


Figure 31. First Generation Sensor Design and Prototype

The first generation design was built for low temperatures and used to test the demodulation system and the sensitivity of the sapphire diaphragm assembly. Several attempts were made to create a fully assembled high temperature probe using the first generation design shown above. The high temperature version of the first generation sensor utilized Solderglass SCC-7 as the primary bonding agent between the diaphragm, Alumina tube, and the Kovar probe material. The bond between the diaphragm and the Alumina tube on several tested probes, similar to that on the probe shown in Figure 32, passed the construction stage. However, nearly all failed prior to testing. Delamination occurred in the solder glass bond between the housing and the alumina assembly.

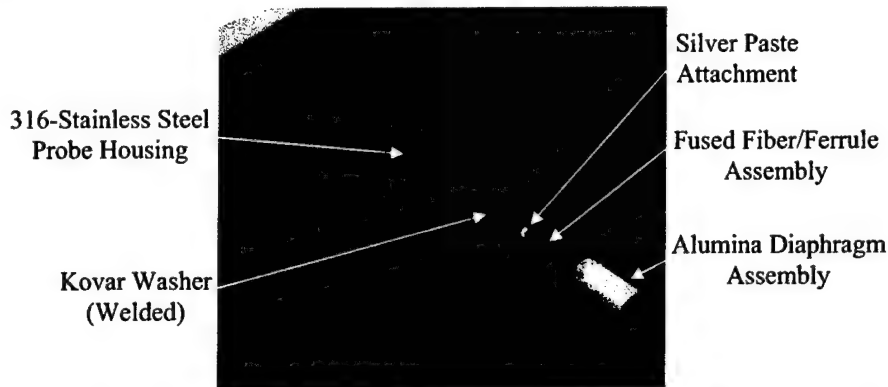


Figure 32: High-temperature pressure probe assembly. HeNe laser light being projected through the fused fiber/ferrule assembly. The alumina diaphragm assembly is detached from the probe housing in this image.

It was speculated that this was due to the thermal expansion of the fiber/ferrule assembly versus the diaphragm assembly. The common link between these two critical components is the probe housing. The farther apart these assemblies are attached with respect to each other, the more pronounced the thermal expansion will appear. A brief test was performed on one of the stainless steel capillary fiber/ferrule assembly probes. The results of this test are shown in Figure 33. This verifies the suspicion that there was a reasonable gap change between room temperature and 800°C. However, this does not fully prove that the thermal expansion caused the solder glass bond to fail. Further studies with other parallel construction methods were explored in order to establish a high temperature method of bonding and construction that produced an acceptable yield.

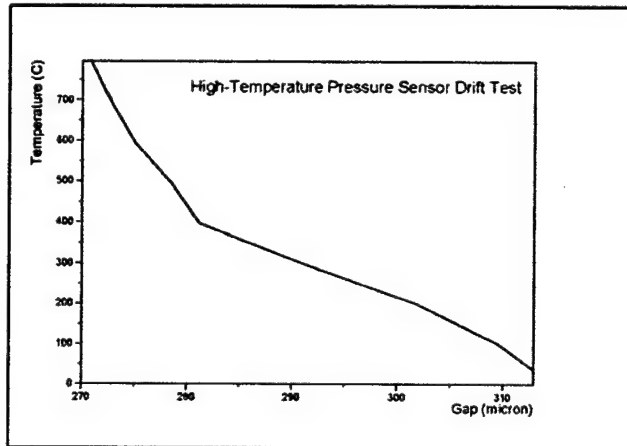


Figure 33: Temperature drift test on the stainless steel capillary fiber support design.

4.2 Active Cooling System

The sensor tip design shown in Figure 34 is designed to keep the temperature of the optical fiber and bonded sections of the sensor at 700°C or below. This is accomplished by interrogating the sensor with an inert gas that will remove the heat from the optical components while the sensor is operating. The gas flows down a small stainless steel tube surrounding the optical fiber to the sensor tip. It is then routed through the sensor tip out exhaust ports that are vented away from the turbine.

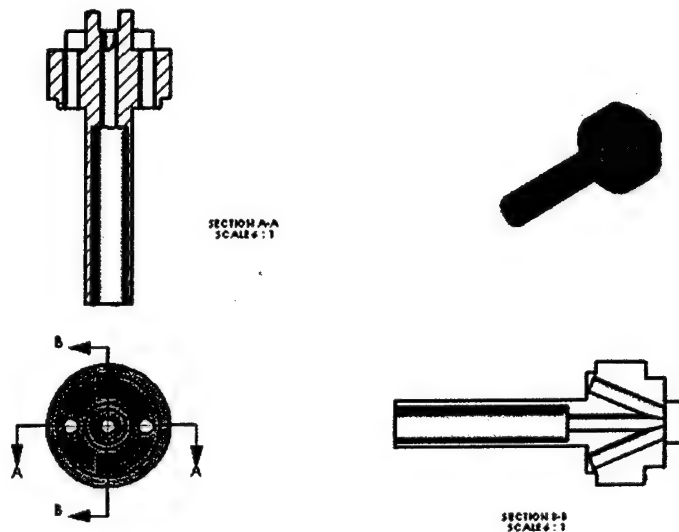


Figure 34. First Generation Cooled Sensor Tip

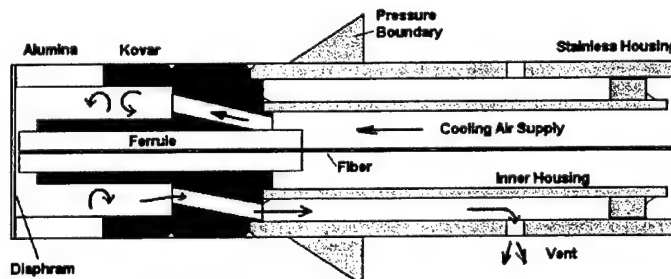


Figure 35. Cooling Air Flow Concept

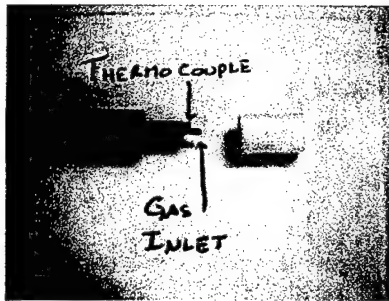


Figure 36. Gas-cooled sensor demonstrator

A proof of concept experiment was designed around the first generation sensor body. A stainless capillary tube was inserted in the housing to introduce cooling gas at the back of an alumina diaphragm diffusion bonded to an alumina tube. The alumina assembly was bonded to stainless steel housing with SCC7 solder glass. A thermocouple was inserted alongside of the air inlet tube but slightly recessed to measure the internal temperature of the demonstrator (Figure 36).

During proof of concept testing three experiments were performed. The first experiment consisted of elevating the sensor to a temperature and then passing nitrogen at 15°C and 10psi through a capillary tube and past a thermocouple positioned where the fiber would be in a working sensor. This cooled the probe assembly down and data readings were taken when the temperature stabilized within the diaphragm assembly. The data is shown in Figure 37.

This resulted in an average temperature difference of 150°C between the inside of the housing and the environment directly outside the bond between the Kovar and the ceramic tube. The temperature was increased until the sensor failed.

The second experiment was performed by using the same set up and running the cooling gas continuously while the temperature surrounding the housing was increased. The data indicates that the same amount of cooling was not achieved as in the first experiment, maintaining an average difference in temperature of approximately 75°C. This reduction in cooling reduction may have been due to the thermocouple partially blocking the cooling gas flow.

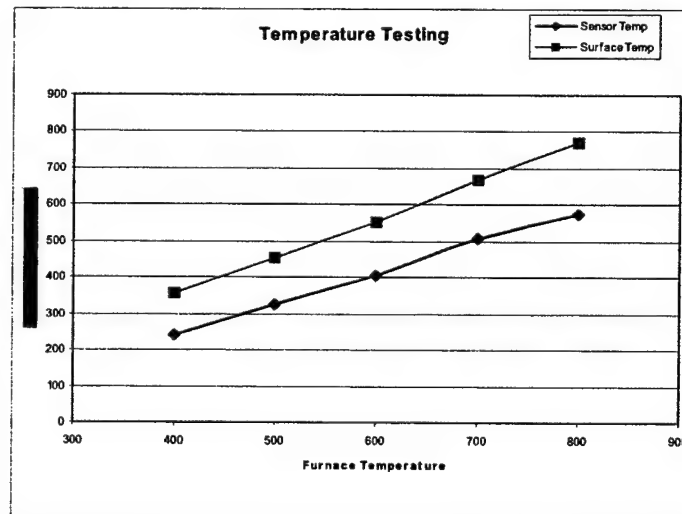


Figure 37 Gas-cooled sensor experiment 1.

A different approach was taken for the third test. A SiC temperature sensor was used in place of a thermocouple. The SiC temperature sensor has a smaller diameter than the thermocouple, leaving an open passage for the cooling gas flow. The sensor housing constructed for this test was accomplished by connecting stainless steel tubing to the first generation tip. The assembly is shown in Figure 38.

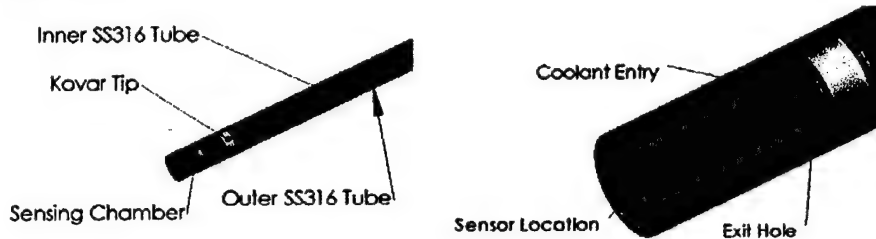


Figure 38. Third Housing tested for cooling efficiency

The sensor housing was attached to the furnace door with a swedgelock fitting placing the sensor tip in the heat affected zone and the vent outside of the heating environment. A K-type thermocouple was secured to the door housing in a position to give the temperature reading at a point outside of the housing. This provided the data to establish the temperature difference between the sensor chamber and the external environment. Figure 39 illustrates the position of the sensor relative to the thermocouple inside of the furnace chamber.

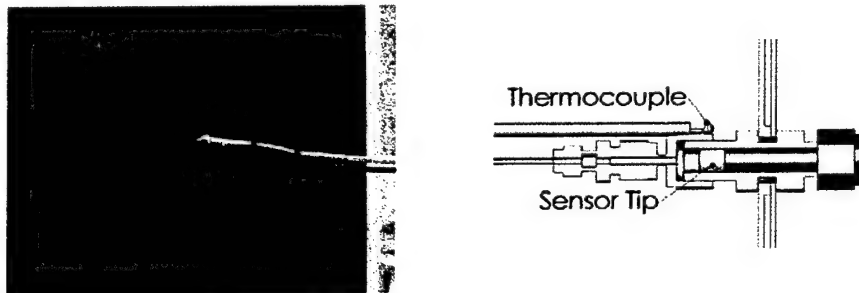


Figure 39. Test Setup for third cooled sensor housing experiment

The silene sensor was calibrated to relate the measured gap as seen by the FiberproUSB to the temperature inside of the furnace. Calibration was performed by increasing the temperature of the furnace to 600 °C in increments of 50 °C and the gap measurements recorded. From these measurements a second order equation was derived using the curve-fitting feature in Microsoft Excel to relate the optical gap to temperature. Equation 1 relates the measured gap to the temperature of the thermocouple secured to the furnace door.

$$T_s = -89.912 X_g^2 + 7554.5X_g - 157856$$

(1)

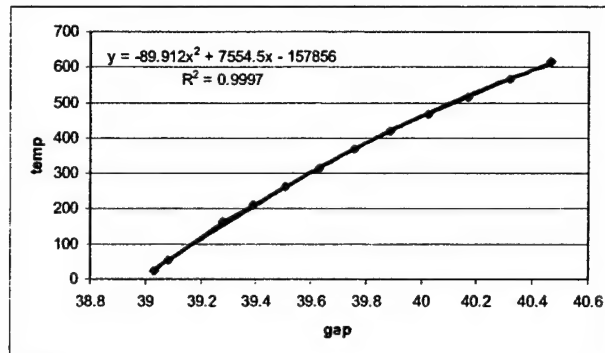


Figure 40. Calibration data and curve for SiC Temperature sensor

In this equation T_s is the temperature inside of the sensor housing and X_g is the gap registered by the silene sensor. This was used to define the temperature inside of the sensor chamber once the coolant flow was added and the furnace temperature was increased. After a furnace temperature of 600 °C was reached, N_2 was slowly added to cool the sensor chamber by regulating the pressure supplied with a Ruska Pressure Control System until a pressure drop of 10 psi was achieved. The furnace temperature was then increased to 900 °C in increments of 50 °C and the optical gap recorded at each step. At a temperature reading of 889 °C the sensor gap was 40.1550 μm equating to a temperature of 518.7 °C in the sensor chamber. At a furnace temperature of 900 °C the pressure drop was increased to 20 psi in order to achieve greater cooling of the sensor chamber. This resulted in a gap of 39.182 μm and a temperature of 291.1 °C.

The data collected during the test resulted in an average temperature difference of 330 °C between the sensing chamber and the environment. Figure 41 displays the data collected. A temperature difference of 370 °C was observed between the inside of the pressure sensor and the outside environment when using a supply pressure of 10 psi. A temperature difference of 591 °C was observed by using a higher supply pressure of 20 psi.

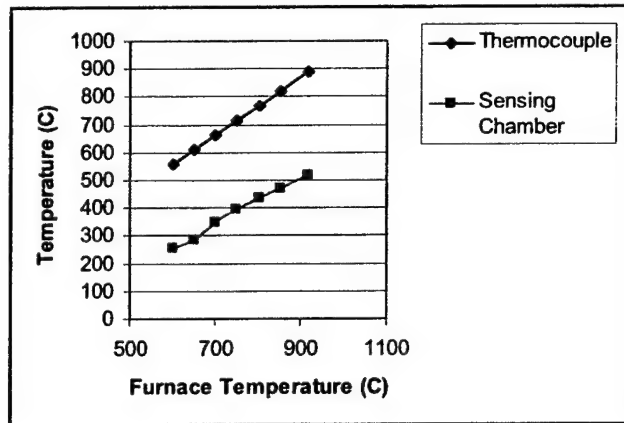


Figure 41. Sensing chamber and thermocouple temperatures vs. Furnace Temperature

4.3 High Temperature Bonding Methods

The sensor design calls for three bonds between dissimilar materials that are raised to elevated temperatures. Methods under consideration for these bonds were diffusion bonding between the sapphire diaphragm and the Alumina tube, a high temperature silver adhesive and active metal brazing. All of these methods were tested for material compatibility and utilized where they would be successful.

4.3.1 Glass-Ceramic and Silver Bonding

Luna has been working closely with Virginia Tech to develop a rugged medium temperature (800°C) bond between the Kovar and the Al_2O_3 . This design utilizes multiple layers of glass-ceramic, silver, and silver-palladium. These layers are fired at temperatures just below the respective melting temperatures. The metals and glass-ceramic material is sintered to each part. Finally a silver or silver-palladium bond is used to join the two parts. The experiments so far have focused on developing the bond between two alumina tubes to minimize cost involved with the development of the technique. Two assemblies were tested to 500psi without failure or hermeticity issues. Figure 42 shows one assembly which failed before 100psi was achieved. To further analyze the bond quality, SEM photographs are being analyzed of a sectioned bond (Figure 42).

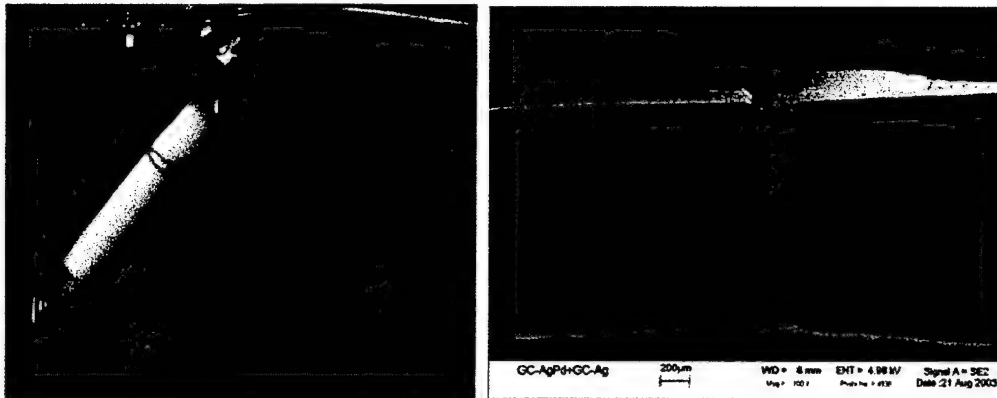


Figure 42. Hermeticity Testing (left) and SEM image of GC/AgPd+GC/Ag/Ag bond.

One assembly was tested to failure in a 3 point bend. Failure mode appeared to be ductile failure of the silver intermediate bond. The maximum recorded load to failure was 170 N. The longitudinal stress on the tube was tensile opposite the location of the applied force with the maximum stress at the outermost wall. Based on the tube wall thickness, the maximum stress, σ_{max} , is 67.9 MPa. It should be noted that the maximum tensile stress of silver is 140 MPa and yielding should occur at a lower stress. Using the inner tube area, the maximum estimated sensor pressure to cause failure at room temperature is around 2700 psi, assuming the bond is hermetic.

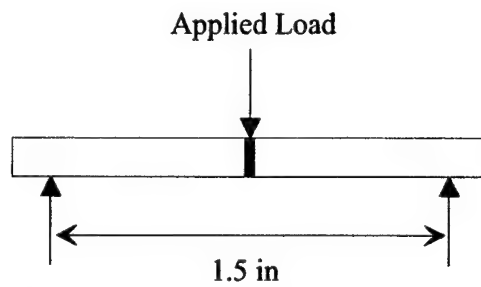


Figure 43. Schematic of the 3-point bend test used on the butt joint.

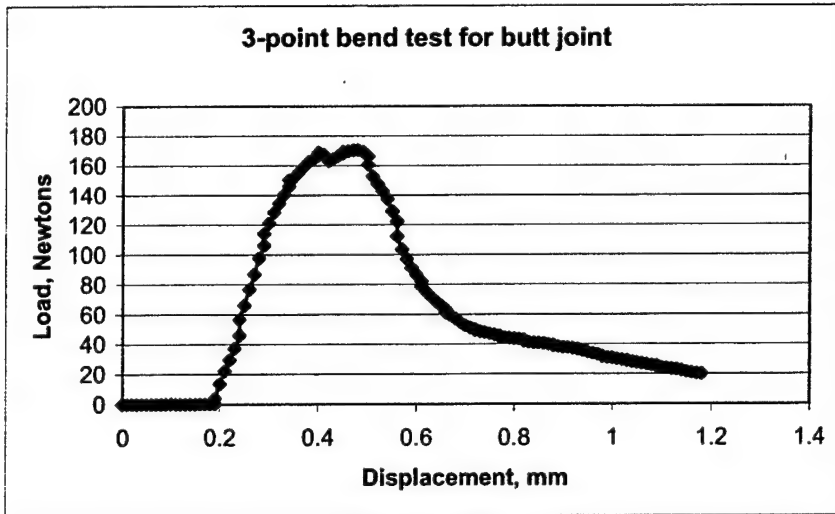


Figure 44. Loading curve on the test specimen during the 3-point bend test.

4.3.2 Diffusion bonding at Virginia Tech

Diffusion bonding experiments were conducted at Virginia Tech progressing down two parallel paths. The initial method was to stack the pieces to be bonded inside a high temperature furnace and hold at a temperature of 1600 °C for 5-8 hours. This method produced an average of a 50% yield. Alternatively, a pressure-assisted diffusion process was developed. This process included the addition of pressure on the pieces to be bonded by a custom fixture activated by a press. A custom furnace was also designed and constructed to enclose the fixture.

Technical issues that were being addressed by Virginia Tech included the operation of the custom furnace and polishing of the parts for bonding. A uniaxial press was used to apply pressure to the alumina tube and diaphragm samples at elevated temperatures. A universal joint has been employed to aid in alignment of the samples. Bonding took place under uniaxial stress at a temperature of 1000°C. However, this process was not dependable and the initial samples showed adhesion but not hermeticity above 100 psi.

To obtain a strong, uniform bond between a high-purity alumina tube and an alumina diaphragm, both substrates are highly polished to yield planar surfaces. A diamond grinding media has been identified to better polish the samples as compared to the previous supplies. Samples were cut and polished using diamond grinding paper to obtain a fine surface finish. In previous experiments, bonding occurred when a weight was placed on top of the alumina diaphragm. However, the weight applied also caused significant warpage in the diaphragm, and bonding occurred between the weight and the diaphragm. By placing the tube on top of the diaphragm, the weight of the sample itself can be used advantageously to promote strong bonding. With an excellent finish on both surfaces, this method can be highly effective at a temperature of 1600°C.

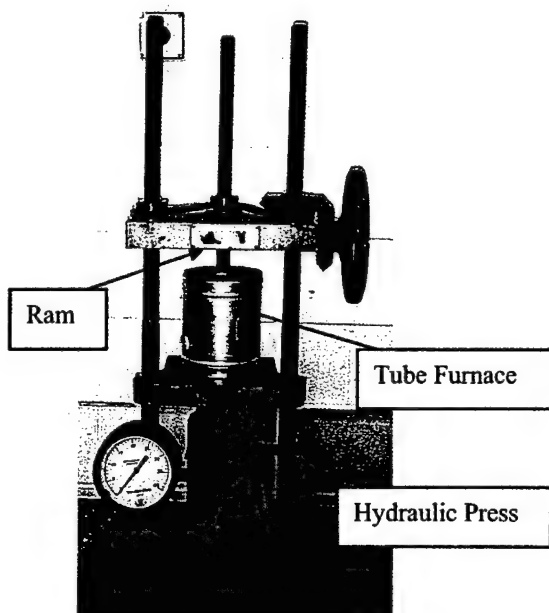


Figure 45: Pressure-assisted heated press for diffusion bonding.

alumina pieces from the metal ram which acts as a heat sink. Likewise, alignment of the samples proved to be very difficult. Therefore the team investigated alternative attachment methods.

4.3.3 High Temperature Silver Adhesive

Previously, investigation into the use of a high temperature silver adhesive paste was carried out to be used as the bond between the fiber and the ferrule and the sensor tip as shown in Figure 46. With the utilization of fusing the fiber into the capillary tube as a means for attachment, the use of high temperature silver adhesive was utilized only as a method for securing the fused ferrule assembly into the sensor housing. The silver adhesive is capable of withstanding 1000°C and will adhere to ceramics and metal alloys with strongly attached protective oxide layers.

Large amounts of oxidation developed on the surface of Kovar at elevated temperatures. In house development efforts on related work found that it was possible to deposit a thin layer of nickel onto the Kovar tips to passivate and prevent oxide development. The nickel plating allowed the high temperature silver adhesive to develop a permanent hermetic bond between the fused ferrule assembly and the Kovar tip. Cooling channels were introduced to the sensor tip to maintain a temperature inside of the sensor tip lower than the melting point of the silver adhesive.

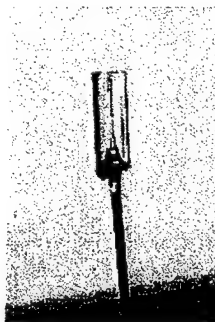


Figure 46. Silver potted fiber/ferrule assembly.

At a temperature of 1000°C and soak time of 1 hour, some bonding was achieved. One of the two samples bonded with the diaphragm, while the other did not. The sample that did not bond had a poor surface finish compared to the sample with the polished surface. All three of the alumina pieces exhibited cracking similar to that seen before. In this case, the cracking did not cause total failure in the samples. It is believed that this cracking was caused by thermal shock to the ceramic, not by the compressive force applied. Upon cooling, a tensile hoop stress is applied to the outer portion of the tube, causing it to crack. This will be addressed by insulating the

4.3.4 Active Ceramic and Metal Brazing

The most promising bond developed during this development effort is utilized between the sapphire diaphragm and the Kovar tip and was developed by Aegis Scientific for Luna. This bond is capable of remaining hermetic at temperatures of 1400°C and is capable of joining the Alumina to Kovar and the Alumina to sapphire materials. The bond and a concept of the bond placement are shown in Figure 47. The process used to make this bond consists of placing a proprietary ceramic solder frit, consisting of all oxide materials, around the sections to be bonded and curing the material in a vacuum furnace. Several of these bonds were produced for high temperature testing at Luna Innovations.

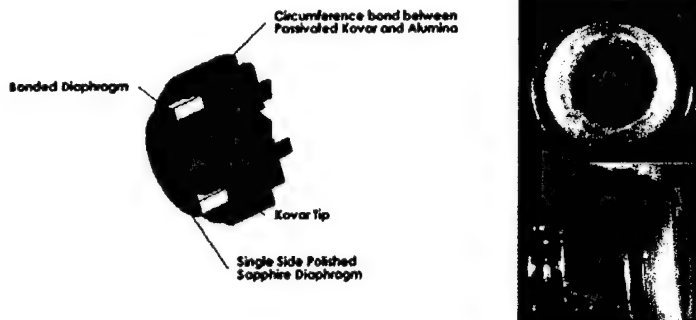


Figure 47. Sensor tip bonded by Aegis Scientific

The bonds were subjected to the flame produced by a propane oxygen torch. This experiment was conducted to test the bonds in a flame environment under high temperature conditions. A thermocouple was placed at the Alumina – Kovar interface and the tip was heated to 1400°C. Inspection of the bond upon completion of the test revealed that it had remained intact. Figure 48 shows the test in progress.

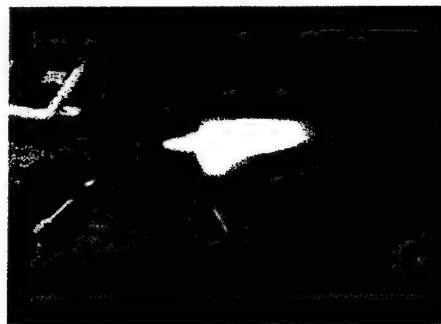


Figure 48. Aegis Scientific bond being subjected to Oxy-Propane Torch.

4.4 First Generation Testing

An experiment was designed to show the frequency response of a fiber optic pressure sensor and to demonstrate the Luna Innovations Hyperscan instrument. The Luna and Virginia Tech (VT) researchers modified a Garret F109 medium bypass turbofan gas turbine inlet shroud for instrumentation with a Luna fiber-optic sensor. This implementation is shown in Figure 49. This particular sensor was constructed using medium temperature adhesives since the high

temperature bonding work had not been completed. The goal of this experiment was to demonstrate that a sensor constructed from alumina or sapphire materials could detect the small pressures caused by blade passage.

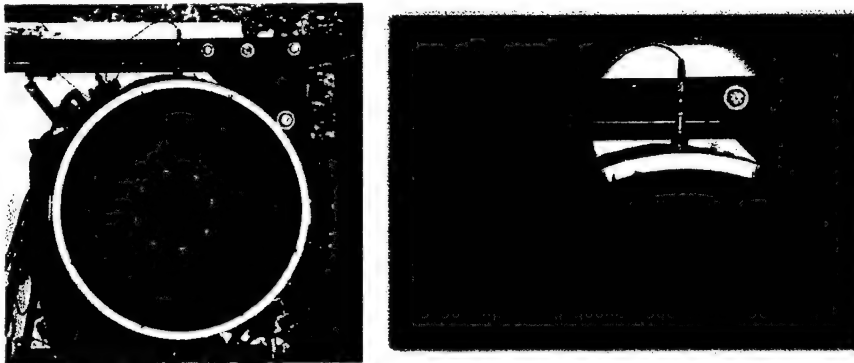


Figure 49: VT Garret F109 gas turbine with Luna sensor installed (left) close-up (right).

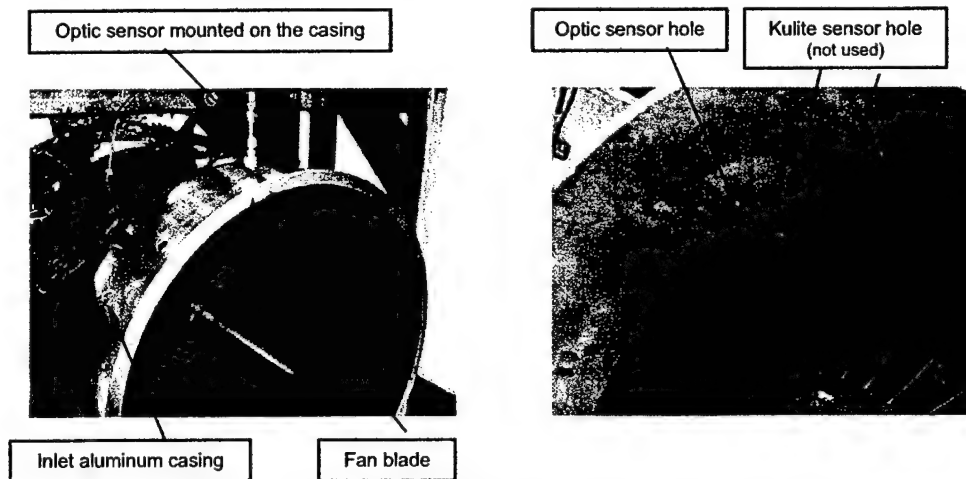


Figure 50: F109 Engine with the optic sensor mounted at the Inlet

The sensors were calibrated on sight before installation and testing to ensure good data. Figure 51 shows one of the calibrations of a fiber-optic sensor used in this test which had a Sapphire diaphragm 0.003" (75 μ m) thick. The sensor was installed in the intake of the engine, approximately 4 inches in front of the fan of the Garret engine. The fan of this engine has 30 blades and has a maximum speed of 17,200rpm. The engine laboratory is at an altitude of 2000ft above sea level, and test conditions were 84°F and more than 60% relative humidity. Therefore the maximum attainable speed of the fan in this engine during the test was 80.4% or 13,827rpm.

Figure 51 shows $\frac{1}{4}$ of one revolution of the inlet fan in a sample of data captured from the fiber-optic sensor showing pressure changes from blade passing at max attained speed.

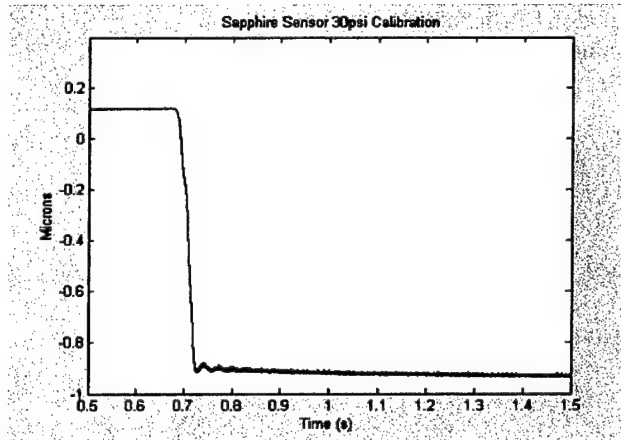


Figure 50. Sensor calibration

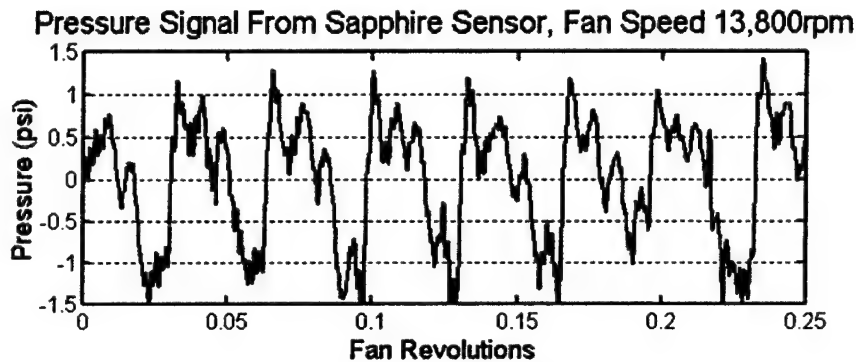


Figure 51: Fiber optic sensor and gas turbine data (right).

This data compares very favorably with data collected on this particular engine for a student's dissertation³. The data was collected by a student utilizing a Kulite™ style pressure sensor, also placed in front of the inlet of the Garrett F109 engine in approximately the same location. The data is shown in Figure 52. The Luna sensor data is clearer than the Kulite data, and has very little ringing. In addition, the Luna sensors have measured pk-pk pressure fluctuations of ± 1.5 psi while the Kulite sensor only measured fluctuations of ± 1.1 even though the fiber sensor was located farther from the fan at approximately 1.7 inches than the Kulite, which was located closer to the fan at 1.2 inches. This could be an indication that the Kulite sensor's frequency response was attenuating the measurement. The fact that the fiber sensor has a higher pressure

³ "Investigation of Inlet Guide Vane Wakes in a F109 Turbofan Engine with and without Flow Control", Jeffrey D. Kozak, Ph.D. dissertation, Virginia Polytechnic Institute and State University department of Mechanical Engineering, August 2000, Blacksburg VA., copyright J.D. Kozak, 2000

measurement suggests a higher frequency response in the fiber optic sensor with regards to current off the shelf capability.

13 k rpm

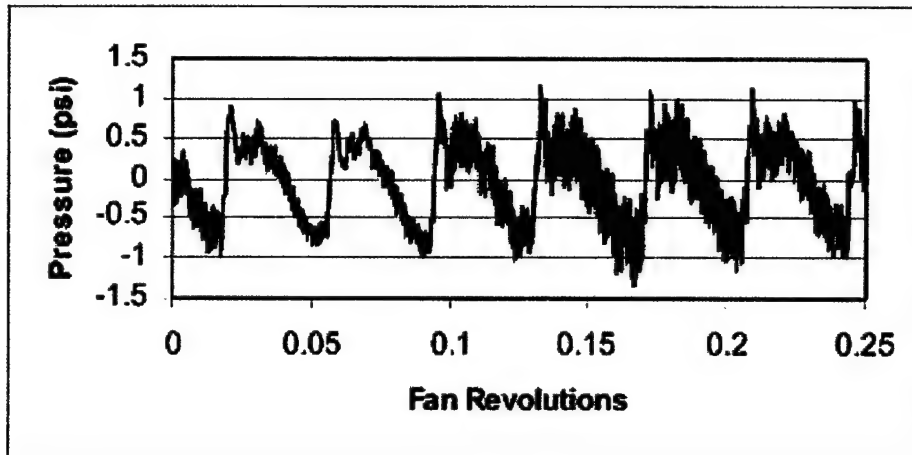


Figure 52. Kulite pressure sensor data from Garrett F109 engine taken from VT Master of Science thesis.³

Due to the relatively long distance between the sensor and the fan (approximately 1.7 inches), the sensor was not sensitive to blade passing at blade speeds below supersonic. At 13,827 rpm and 12,783 rpm the fan blade tips achieved 1162 fps and 1032 fps respectively. These speeds correspond to blade passing frequencies of 6914 Hz and 6392 Hz. Data was captured from the sensor at both of these fan speeds, and a Fourier analysis performed to extract the frequency data. Figure 53 shows a frequency peak of 6897 Hz in the data collected from the sensor while the engine fan was rotating at 13,827 rpm. The expected frequency from blade passage is 6914 Hz. The measured value is therefore only in error by 0.25%. Similarly the data collected while the engine fan was rotating at 12,783 rpm has a frequency peak at 6348 Hz vs. an expected frequency of 6392 Hz. The error in the second frequency measurement is only 0.7%.

Also marked in these frequency spectra is a peak frequency of 141 kHz. The first fundamental frequency of mechanical resonance of this sensor was calculated using standard formulations circular diaphragm with a clamped edge.⁴ For a Sapphire diaphragm of 1.6 mm active radius, the first fundamental frequency is approximately 138 kHz. As can be seen in both of the Fourier analyses, this resonant frequency is being excited by the engine and being measured by the Hyperscan instrument with an error of only a 2% error, demonstrating that the Hyperscan system is making very accurate time response measurements.

⁴ Di Giovanni, Flat and Corrugated Diaphragm Design Handbook

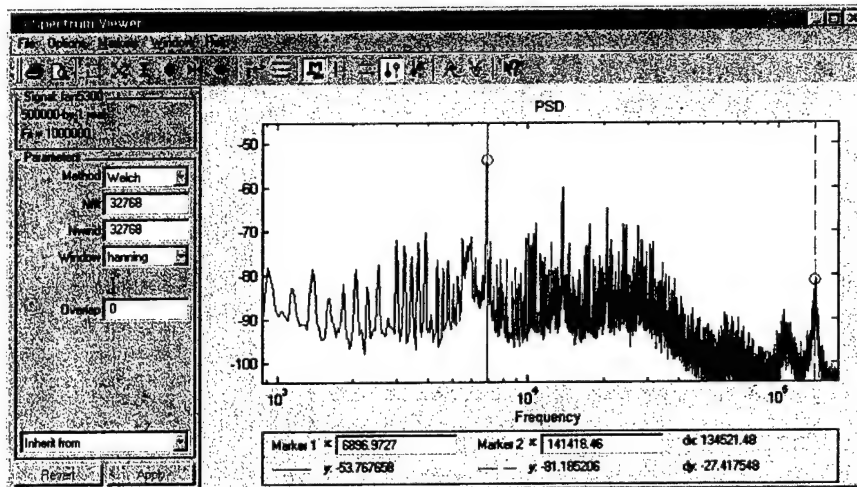


Figure 53. Frequency analysis of data recorded by fiber sensor with the engine fan rotating at 13,827 rpm.

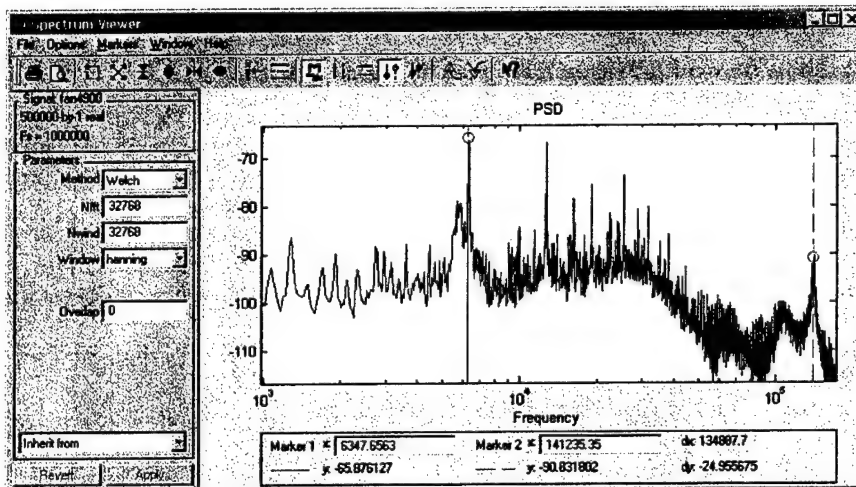
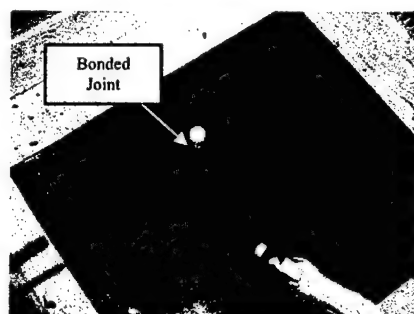


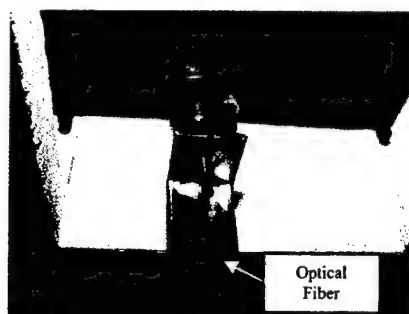
Figure 54. Frequency analysis of data recorded by fiber sensor with the engine fan rotating at 12,783 rpm.

4.5 High Temperature Testing

In parallel with another development effort, high temperature testing was conducted to verify that the sensor design would be able to survive and operate at temperatures in excess of 1100°C. To safely conduct the high temperature testing, a custom furnace door was designed at Luna to produce a temperature barrier between the front and rear sections of the sensor probe and to act as a holder for the sensor. This door was designed to simulate a turbine engine combustor and the thermal gradients between the interior of the hot zone and the exterior of the engine. Figure 55 illustrates the operation of the furnace door.



a) Top View: Sensor probe inside the furnace



b) Bottom View: Sensor probe portion outside the furnace for cooling

Figure 55: Custom furnace floor for a more controlled firing process.

Testing Strategy and Setup

In order to test the pressure sensor at elevated temperatures, a custom furnace door was fabricated at Luna. The concept was to allow for the transducer head to reach the maximum temperatures and pressures, while the rest of the probe remains at ambient pressures and lower temperatures. The door, seen in Figure 56 and Figure 57, was designed with an air gap to create a sharp temperature drop between the interior of the furnace and the exterior. The probe is held in the door with Swagelok fittings. The fittings were also designed to introduce pressure specifically to the transducer in the heated zone. The portion of the probe exterior to the furnace was monitored with a thermocouple to verify this temperature drop, as seen in Figure 57.

To test the setup, a dummy probe was installed which contained a thermocouple in place of the optical fiber. The bead of the thermocouple was located in the expected hot zone of the fiber next to the diaphragm. The test was run to ~1000°C with the dummy probe. Temperatures were measured inside the probe and on the probe outside the furnace as shown in Figure 58. The image labeled A in Figure 58 shows the setup prior to the test. The image labeled B is at the peak temperature during the test. Note the temperature of the probe is reading at 988°C, while the probe outside the furnace is reading at 305°C. Additionally, there was a thermocouple located inside the furnace next to the probe tip, external to the probe.

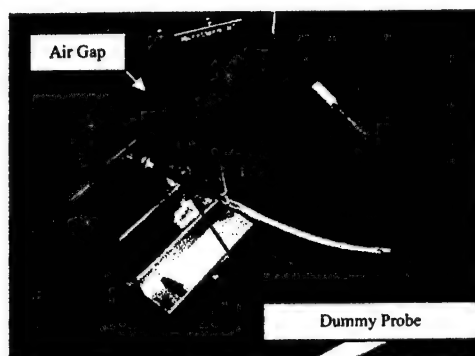


Figure 56: Custom test assembly with dummy probe for high-temperature pressure evaluations.

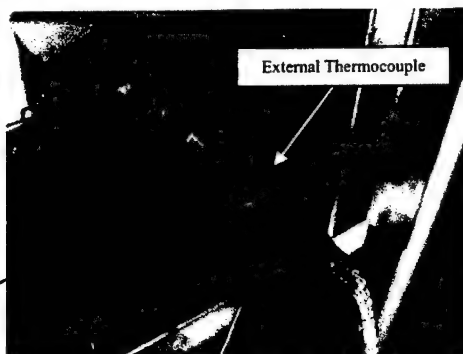
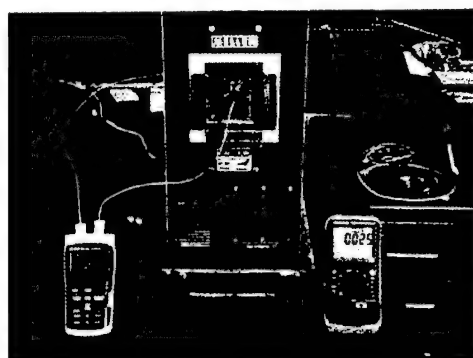
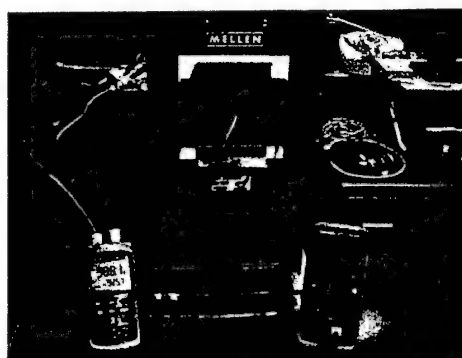


Figure 57: A thermocouple was used to monitor the portion of the sensor outside of the furnace during testing.



a) at room temperature



b) at temperature, 988°C

Figure 58: Test assembly evaluation, left is the probe temperature inside the furnace and right is the external probe temperature.

The dummy sensor was tested as the metal probe without the alumina diaphragm (alumina cap) and again with the diaphragm. Temperature measurements were taken at three locations as mentioned above: inside the probe, inside the furnace, and outside the furnace. These measurements were plotted in Figure 59 to examine the trend and create a calibration curve for testing purposes. Note that the exterior temperature remains below 300°C, which allowed for the epoxy strain relief to survive the tests.

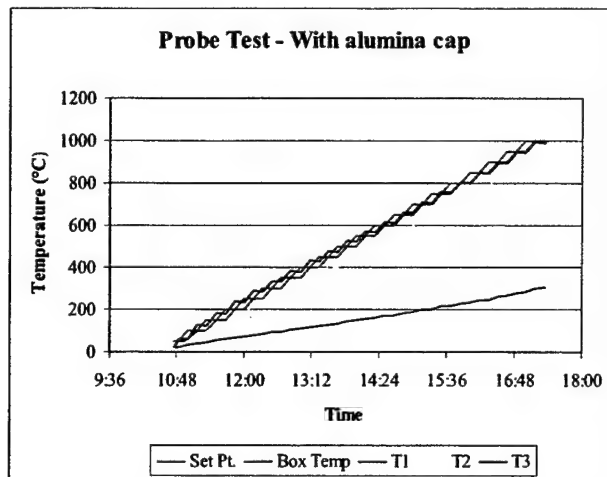


Figure 59: Test Probe Calibration (T1= thermocouple attached to inner fitting inside the furnace, T2= thermocouple inside of the probe, and T3= thermocouple attached to the probe outside of the furnace).

Test Results

Test Set #1

Tests were conducted on a high-temperature pressure sensor. The sensor was constructed with silver paste for the ferrule to Kovar probe bond and solder-glass for the alumina diaphragm to Kovar washer bond. The Kovar washer was welded to the Kovar probe. The limitation was the solder-glass, which has a nominal reheat temperature limit of 800°C. Figure 61 illustrates the test setup. A thermocouple was placed inside the furnace next to the pressure fitting. A second thermocouple was placed on the probe outside the furnace to monitor the probe temperature as shown previously in Figure 58. Figure 60 shows the relative locations of the thermocouples and the sensor tip. This setup allowed for accurate readings to be taken throughout the testing process. Figure 62 shows the sharp fringe contrast of the HT-HP sensor prior to testing.

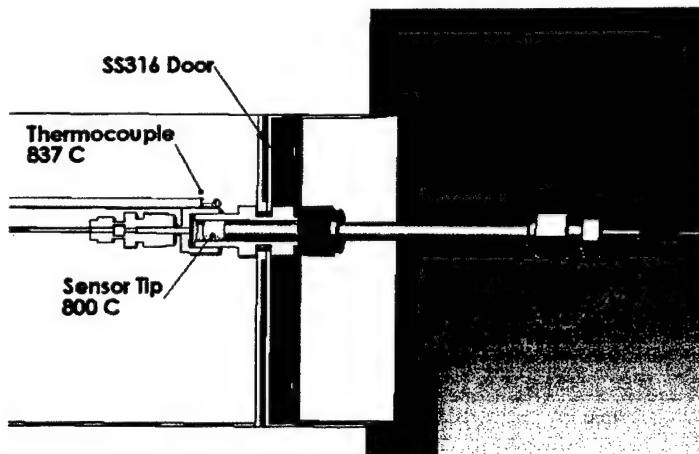


Figure 60: Schematic of test setup for High-Temperature Pressure Probe showing the locations of the thermocouples relative to the sensor tip.

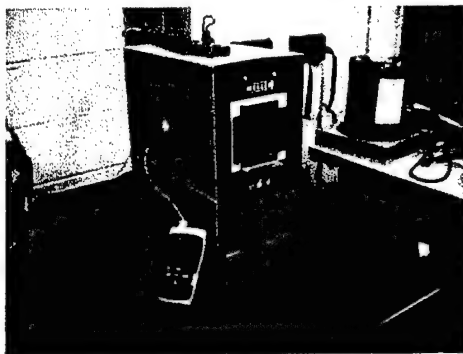


Figure 61: HTP Sensor Test Setup



Figure 62: Fringe Contrast of the HTP Sensor

The tests were conducted with combined temperature and pressure. The temperature was stabilized at a specific set point, at which time the pressure was cycled up and down from 0 psi to 100 psi. The pressure portion of the test was repeated 13 times over two days, and the temperature was cycled from room temperature to 800°C twice over the same time period. Data collected during these tests are shown in Figure 63, Figure 64, and Figure 65.

The pressure changes were recorded as abrupt steps. A Ruska Digital Pressure Controller, recently calibrated with NIST traceable standards, was used to introduce the pressure on the transducer. During the room temperature run shown in Figure 63, the sensor returns to the same values each run. Drift can be seen in the 800°C runs. This drift is due to the thermal conductivity in the probe housing. The stabilizing time between tests was limited to 15 minutes, and the tests, depending on the number of cycles, were allowed to last up to an hour. With time, the probe experienced a slight temperature drift, which was recorded in the gap change. However, the steps between pressure points remained consistent.

A pressure profile (Figure 79) was made to compare the last ten runs illustrated in Figure 65. Notice the linearity and repeatability of the data. Variations in the gap were a result of the temperature drift.

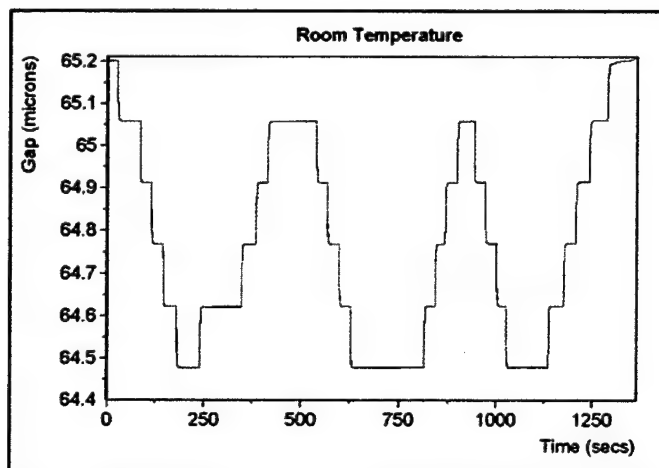


Figure 63: Room temp started at 0 psi, stepped to 100psi then stepped to 20psi. Cycled twice more from 20psi to 100psi then returned to 0psi. Each step is 20psi.

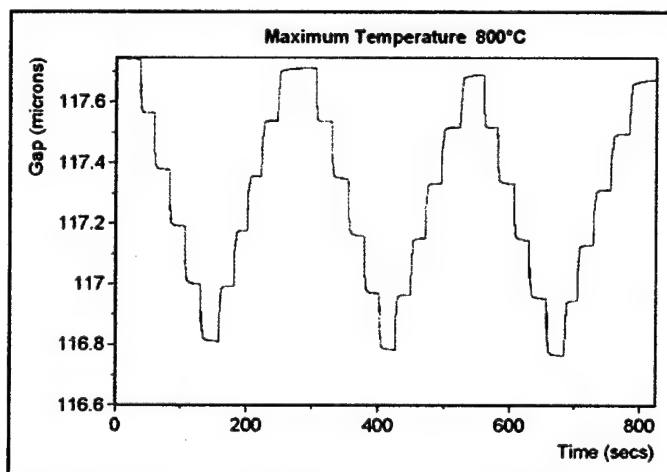


Figure 64: First run to 800°C, started at 0 psi stepped up to 100psi and stepped back down to 0psi. It was cycled 3 times. Each step was 20psi.

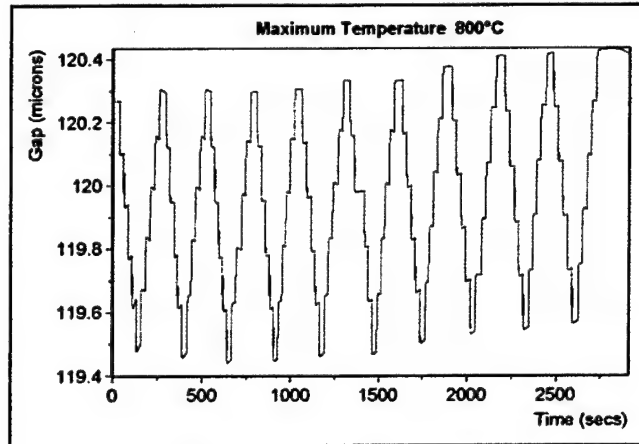


Figure 65: Second run to 800°C the following day. Started at 0 psi, stepped up to 100psi and stepped back down to 0 psi. It was cycled 10 times this way. Steps were in 20psi increments.

Test Set #2

The previous test was repeated with a second sensor keeping all test parameters the same. Starting at room temperature the sensor was cycled twice to 100 PSI using the same increments as before. The sensor was ramped up in temperature to 200°C and cycled to the 100 PSI three times. The temperature was increased to 600°C and the sensor was cycled another three times. Finally the sensor was ramped to the maximum temperature of 800°C and cycled ten times. The sensor output from the first ten cycles at 800°C can be seen in Figure 66.

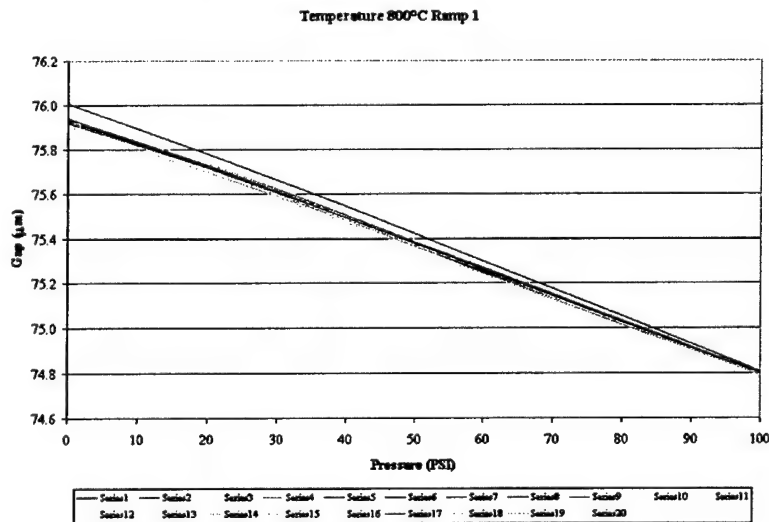


Figure 66: Gap output from 10 pressure cycles on the first ramp to 800°C.

The sensor and furnace were allowed to cool down overnight back to room temperature. The sensor was ramped up to 800°C for a second time and run through ten cycles. After ten cycles the sensor was once again allowed to cool down before being ramped back up to 800°C for the third time at which point it was cycled ten more times. This process was repeated up until the sixth ramp up to 800°C. On the sixth ramp the number of pressure cycles applied to the sensor was increased to seventeen. The sensor was ramped up for a seventh time and then once more for the eighth and final time. Data from the seventh ramp to 800°C with seventeen cycles can be seen in Figure 67. At the close of the eighth ramp to 800°C the sensor had went through over 100 pressure cycles up 100 PSI and was still fully operational. The decision was made to move on with testing to a different demodulation system.

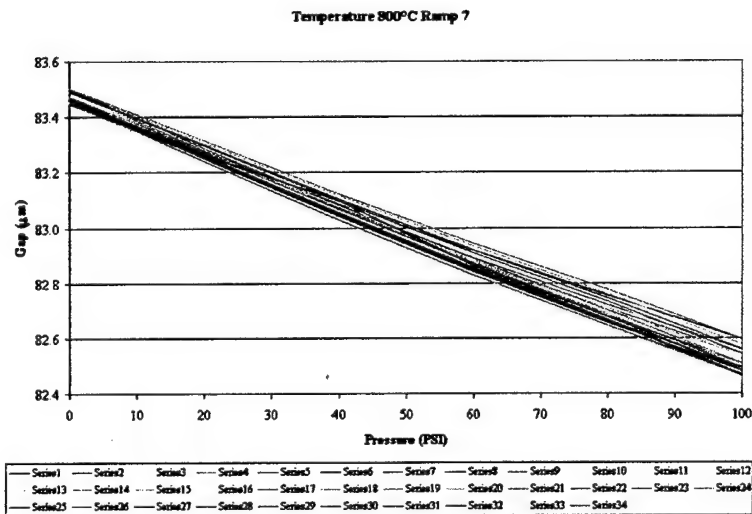


Figure 67: Gap output from 17 cycles on the seventh ramp to 800°C.

Test Set #3

Testing of a high-temperature pressure sensor was also conducted using the Hyperscan demodulation system. In contrast to the FiberPro-USB that shows an absolute gap measurement, the Hyperscan will read a relative gap change in the sensor. The test using the Hyperscan encompassed a pressure range of 0 PSI to 500 PSI. The pressures used were increments of 20 PSI up to 100 PSI, 50 PSI up to 200 PSI followed by 100 PSI increments up to 500 PSI. After each pressure was applied the Ruska (a NIST calibrated pressure unit) was allowed to vent back to atmospheric instead of stepping the pressure up to the next data point. This was because of the nature of the relative measurements taken by the Hyperscan. A sensor was cycled three times each at room temperature, 500°C and 800°C, shown in Figure 68.

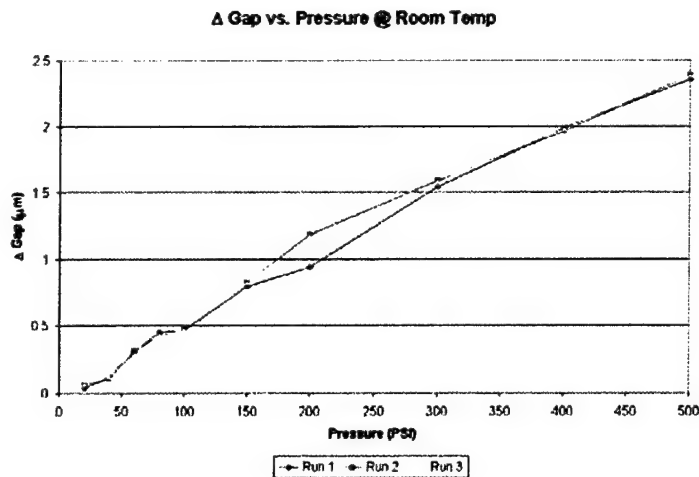


Figure 68: Gap change over three runs from 0psi to 500psi at room temperature

In Figure 68 the points at the low pressures do not follow the same linearity as the rest of the data. There are two reasons why this can occur. First, the Hyperscan provides optimum results when the initial sensor gap is 63 μm . In this case the initial sensor gap was below 63 μm , towards the lower end of the Hyperscan's range. Secondly, at low pressures the sensor did not move through a full fringe, which the system needs for an accurate calibration of true gap.

Figure 69 shows the sensor output on the Hyperscan from the test done at room temperature to 40 PSI. The partial ellipse means that the gap change did not moving through a full fringe with only 40 PSI. A calibration file was used in conjunction with this data to give better results. A calibration file lets the Hyperscan know how a sensor moves or changes when pressurized through a full fringe. The calibration was applied to the data in

Figure 69 and the results are shown in Figure 70. The calibration file used was taken from the test during a later run with higher pressure in which the sensor moved through a full fringe. Thirdly the sensor return signal was very low for this prototype, below that which the Hyperscan gain can be adjusted. Therefore, the sensor signal to noise ratio contributed to the overall error.

Shown in Figure 71 is the output from the run at room temperature with 400 PSI being applied to the sensor. The ellipse can clearly be seen in the upper right portion of Figure 71. This data shows the full movement of the sensor through a fringe and was saved as a calibration file to be used on the lower pressure cycle data.

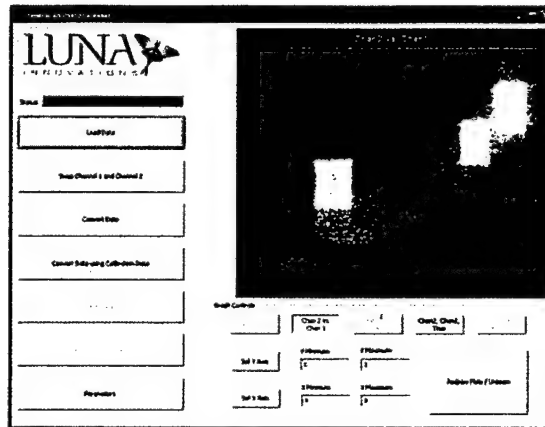


Figure 69: Sensor output on the Hyperscan from Room Temperature test @ 40 PSI.

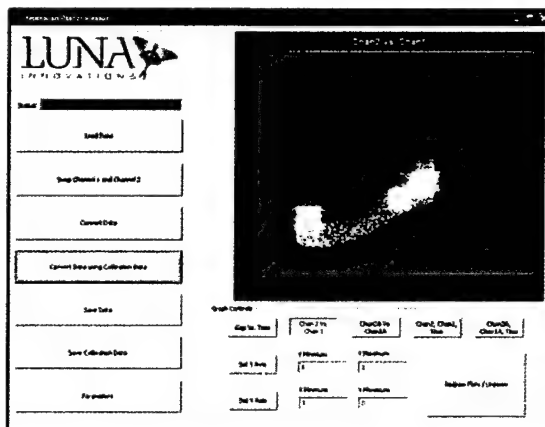


Figure 70: Hyperscan data at room temperature with 40 PSI and with cal applied.

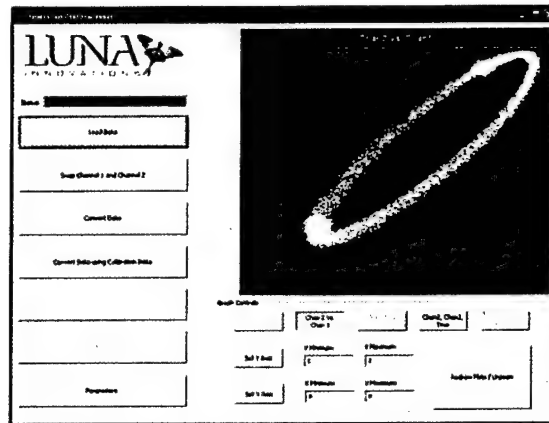


Figure 71: Hyperscan data from room temperature run at 400PSI.

The data at the low pressures improved a during the later runs when the sensor was at 500°C and 800°C, as shown in Figure 72 and Figure 73. This was because of the increase in sensor gap measurement due to thermal expansion and the elevated temperatures. However, there was still an issue with the sensor not having enough movement to roll through a complete fringe at the lower pressures. Figure 74 shows the sensor output while at 800°C with 20 PSI being applied. The data then had a calibration file applied and the result is shown in Figure 75. In Figure 76 we see the output of the sensor during the cycles at 500°C. In this case the pressure applied was 500PSI and a full fringe of movement was achieved. Again, SNR played a significant role in the calibration error.

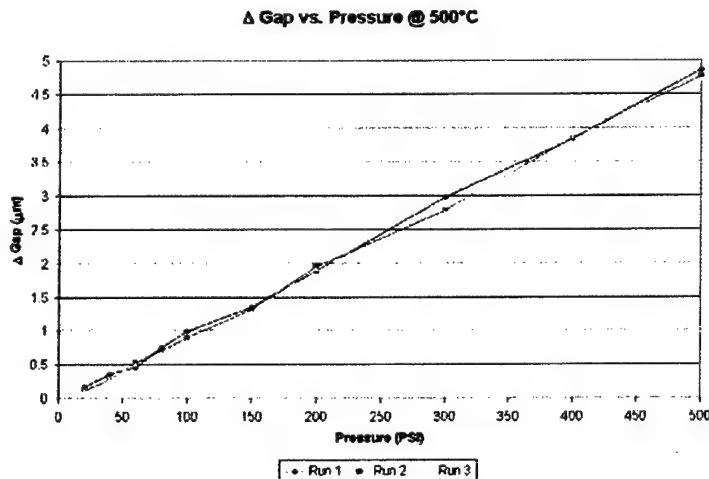


Figure 72: Gap change over 3 runs from 0 PSI to 500 PSI at 500°C.

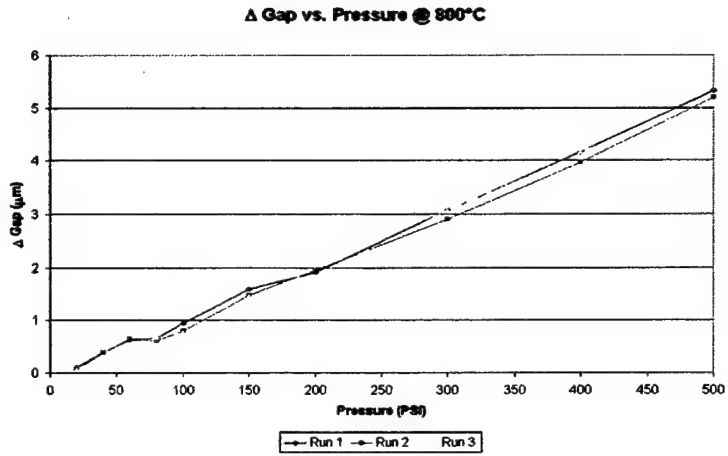


Figure 73: Gap change over 3 runs from 0 PSI to 500 PSI at 800°C

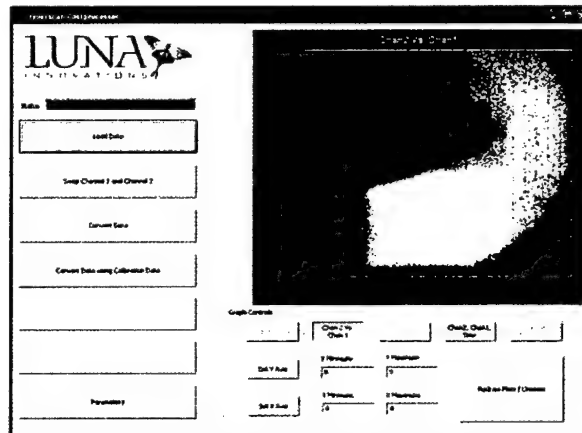


Figure 74: Hyperscan data from 800°C run at 20 PSI.

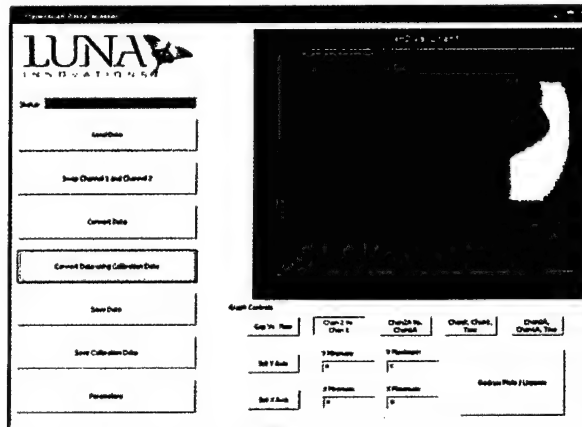


Figure 75: Hyperscan data from 800°C run at 20 PSI with calibration applied.

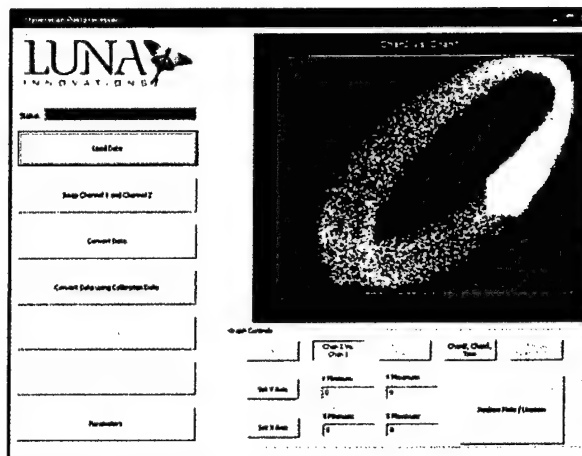


Figure 76: Hyperscan data from run at 500°C with 500 PSI applied.

Test Set #4

Testing was moved back to using the FiberPro-USB for the next sensor, which was built with an Aegis diaphragm assembly as apposed to the alumina diaphragm assembly used previously. The pressure range of 0 PSI to 500 PSI, as well as, the step increments from the Hyperscan test was used for this test. The sensor was cycled once at room temperature then ramped up to 600°C and pressure cycled three times. Next, the sensor was ramped to 700°C and pressure cycled three times as seen in Figure 77. Finally, at 800°C the sensor was pressure cycled three more times and ramped to 900°C. Unfortunately, during the first cycle at 900°C the sensor failed when reducing the pressure from 500 PSI to 400 PSI. The failure occurred because the diaphragm assembly became detached.

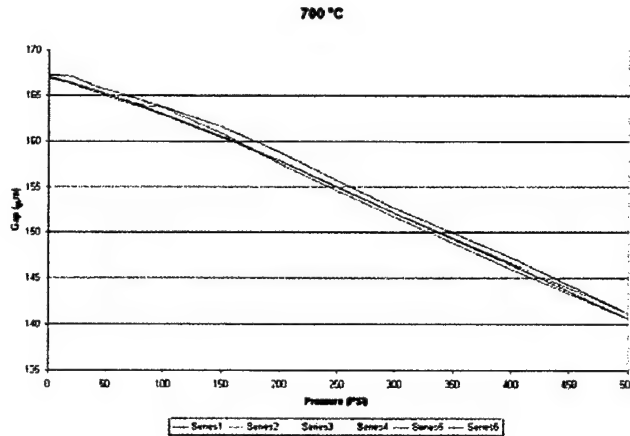


Figure 77: Three cycles at 700°C on sensor with Aegis diaphragm.

Test Set #5

An additional test was conducted with a sensor that was constructed with an Aegis diaphragm to show high temperature survivability. A ceramic door with a small diameter hole was put into the furnace in order to heat the diaphragm assembly end of the sensor. The sensor was inserted into identical fittings as in the previous tests. The sensor in the fittings was inserted into the small hole in the ceramic door and surrounded with ceramic wool. A FiberPro-USB was set to log the sensor's output during the ramp to 1100°C. Figure 78 shows the sensor output from room temperature up to 1100°C, including a 30 minute soak once at temperature. The cause of the erratic data early in the test is unknown at this time. The fringe signals deteriorated between 115°C and 132°C. However, as the temperature increased the fringe signals returned for the remainder of the test as see in Figure 78.

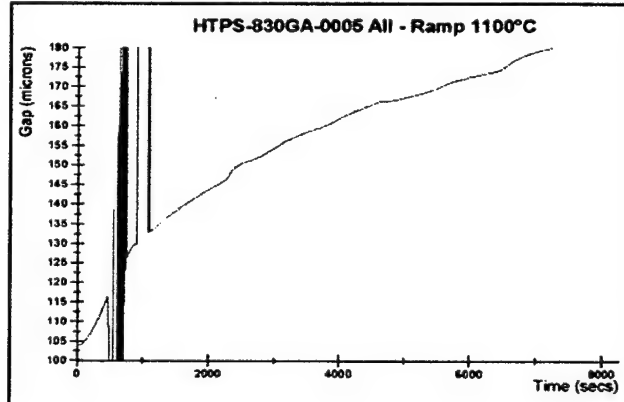


Figure 78: Gap vs. Time data from survivability test on a sensor with Aegis diaphragm.

Testing of the high temperatures pressure sensors revealed a temperature drift caused by characteristics of the furnace illustrated in Figure 65 and Figure 79. It is believed that the furnace could not keep the temperature stable enough during testing to eliminate the drift seen by the sensors.

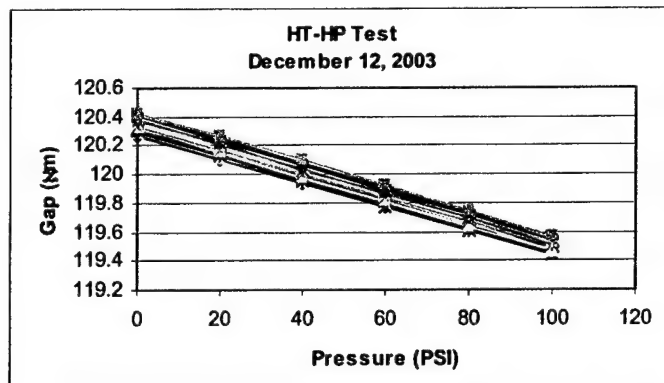


Figure 79: Ten consecutive HT-HP tests at ~800°C.

5. Second Generation Sensor Design and Development

The development of the high-temperature pressure sensor has been guided by testing of several different designs and is a compilation of the advantages and successes of material selections, bonding methods, and construction methods demonstrated during testing. Figure 80 shows the concept for the actively cooled fiber optic sensor for use in gas turbine hot zones for temperatures up to 1100 °C.

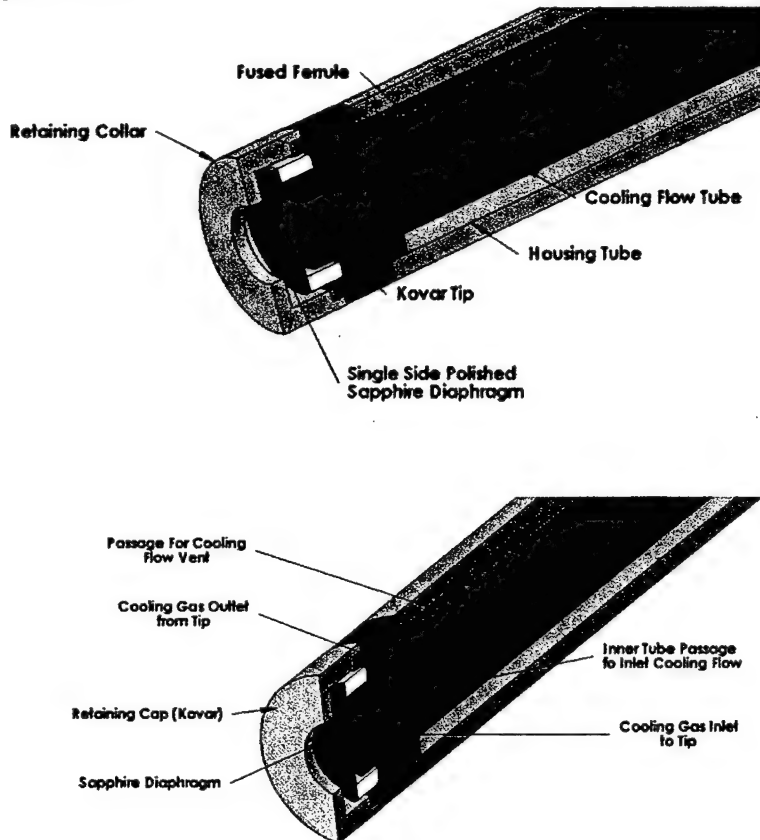


Figure 80. Actively cooled sensor concept combining the advantages of several previous designs

This sensor combines the development of high temperature optical components with an active cooling system to allow for survival in the high temperature harsh environment of a gas turbine engine. The following sections detail the operation and construction procedures developed for this sensor.

5.1 Sensor Operation

The sensor is designed to interpret very slight pressure changes in a surrounding environment. This sensor uses a sapphire diaphragm to translate the pressure changes into a proportional deflection of the diaphragm face as with previous designs. The Hyperscan system then interprets this deflection into pressure measurements by reading the light returned through the optical fiber. The fiber is bonded inside of a fused silica capillary tube through laser fusion. The capillary/fiber assembly is then bonded with silver to the sensor tip containing the reflector, and this assembly is then welded to the remaining components. The sensor design is detailed in the next sections.

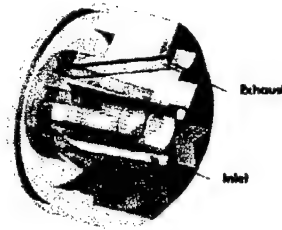


Figure 81. Sensor Tip incorporating active cooling

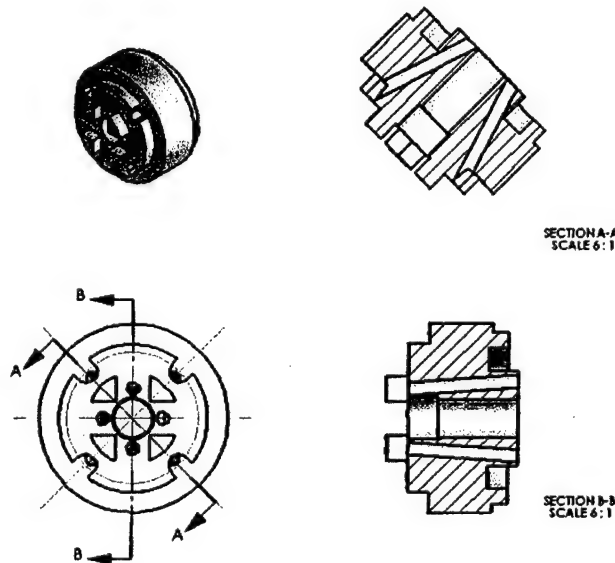


Figure 82. Gen 2 Sensor Design

5.1.1 Absolute Measurement Design

The sensor was initially designed to utilize a collimated design for two reasons. The first was for minimal thermal compensation. By using a collimator to interrogate an assembly consisting of a vented window and a diaphragm to measure pressure, separated by a thin alumina washer, then

the pressure could be measured as the distance between the vented window and the diaphragm. The thermal expansion is then only a function of the expansion of a thin alumina diaphragm. In addition, the fiber and other optical components which could be affected by temperature would be kept relatively cool by distance from the hot zone.

One design feature incorporated in the Gen-II pressure and temperature sensor design is the use of the temperature gradient that exists between the inside of the pressure wall of the turbine engine and the relatively cool exterior of the engine. Using this gradient, a sapphire transducer could be located in the hot zone at $\sim 1400^{\circ}\text{C}$ while the optical fiber resided in a relatively cool region below 850°C only 20mm or so away.

Previous work by Luna Innovations included modeling the temperature profile through a pressure sensor mounted to a turbine casing. The model showed that the transducer could reside in a high-temperature, high-heat flux region ($T = 1400^{\circ}\text{C}$, $J = 1000 \text{ W/m}^2$), while the remainder of the sensor components could reside in a cooler region. The information gained from this model aided the design of the various packaging techniques required. The model assumes a 0.25in diameter alumina probe is housed in a 316 stainless steel housing, and flush-mounted at the inner wall of a 1-inch thick turbine casing. Outside temperature is 150°C (300°F), no cooling air flow is assumed. The model is graphically shown in Figure 83.

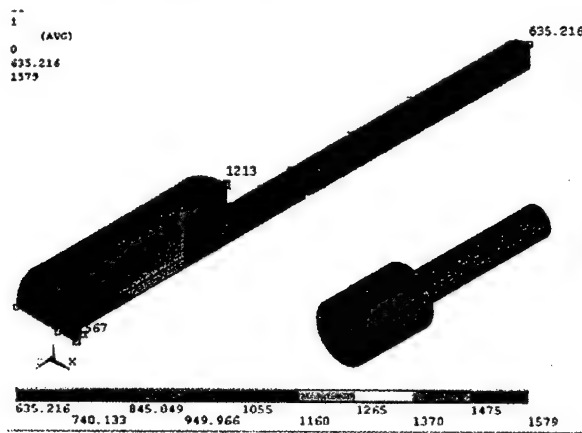


**Figure 83: Thermal modeling of pressure probe mounted at the hot zone ($T=1400^{\circ}\text{C}$, $J=1000\text{W/m}^2$).
Temperatures are shown in Kelvin.**

The various packaging methods of the initial design, and their relative locations within the sensor, are pictured in Figure 84. Note that the sapphire probe tube is solder-glassed or brazed to the Kovar mounting ring which is, in turn, welded to the stainless steel outer housing. The sapphire probe is allowed to slip axially within the outer housing, reducing thermal stresses transmitted to the transducer. Close machining tolerances will minimize cantilever stresses on the braze joints.

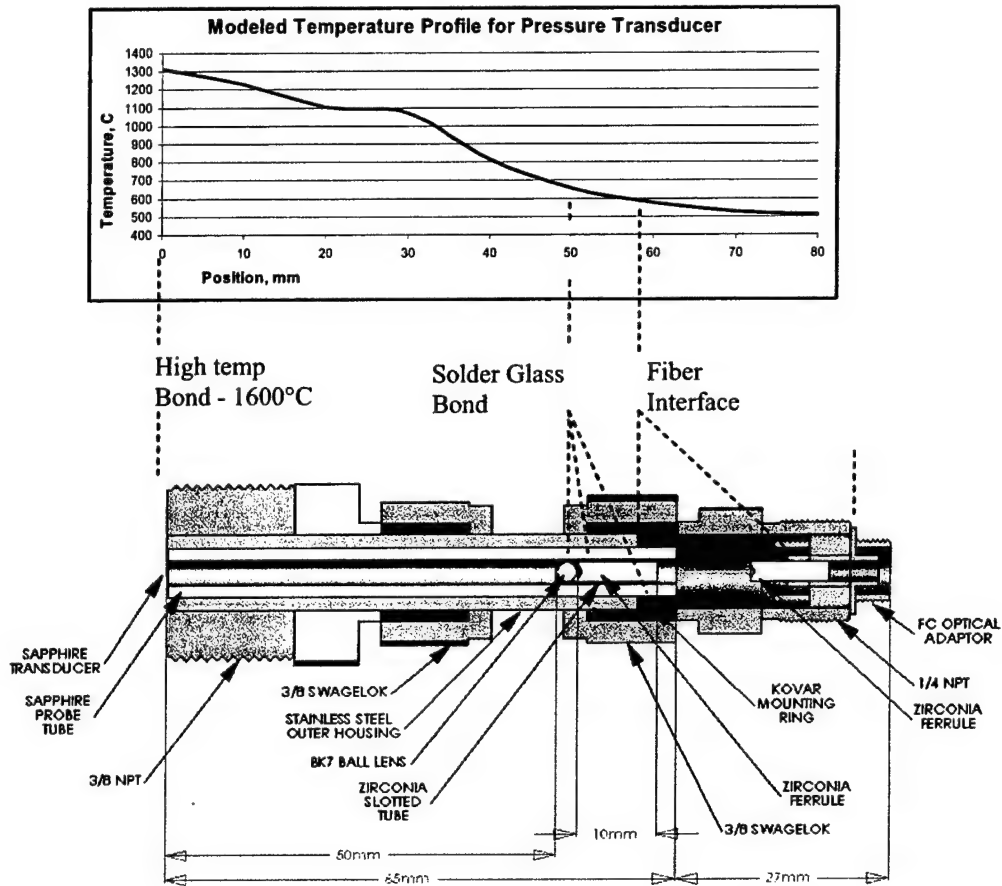


Figure 84: Sketch of the proposed pressure sensor, including locations and expected operating temperatures for the various packaging materials. Upcoming designs will also include high-temperature mechanical fittings.

Unfortunately, the collimator design, when combined with a collimator and a sapphire transducer, caused erroneous output in the Hyperscan system (Figure 85). During the time that this data was taken, the output of the Hyperscan should have been a steady step change in voltage from 2 volts to -0.5 volts lasting 5 μ s. The Hyperscan output is indicated by the blue trace. As can be seen, the return signal from the sapphire diaphragm through the collimator has fringes similar to those from an EFPI sensor in which the gap is changing in time. (Figure 86 and Figure 87).

The Hyperscan system utilizes very narrow bandwidth lasers for wavelength stability. The lasers have very long coherence lengths, and therefore are sensitive to interferometers of long length. It was theorized that the collimator added extra, non-sensing reflections in addition to the transducer reflections. These extra reflections interfere constructively and destructively with the

transducer reflections forming an interferometer that is 50mm long. This interferometer has an optical path length equivalent to nearly 65,000 wavelengths of light making it very sensitive to small change in the interrogation wavelength. A wavelength shift of $1/100^{\text{th}}$ of a nm would equate to an apparent sensor gap change of 650nm, nearly a full fringe. Finally, all semiconductor lasers exhibit small wavelength shifts when the laser drive current is changed rapidly. The wavelength shift is due to very rapid temperature changes within the laser that cannot be controlled in the short time frame. For the sensors developed during this effort the wavelength induced apparent gap change equates to a pressure error of approximately 30-40 psi. Therefore, it was theorized the laser wavelengths of the Hyperscan were changing a small amount during the switch from one laser to another to generate the interference "fringing" shown in Figure 88.



Figure 85. Oscilloscope trace of sensor output.

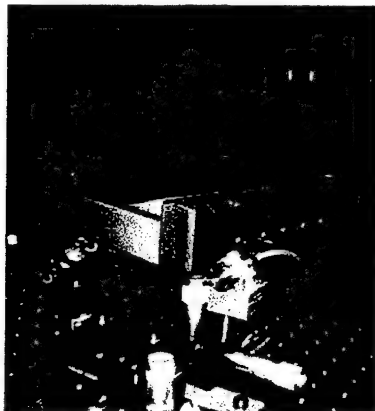


Figure 86: Hyperscan set up for temperature sensor component testing.

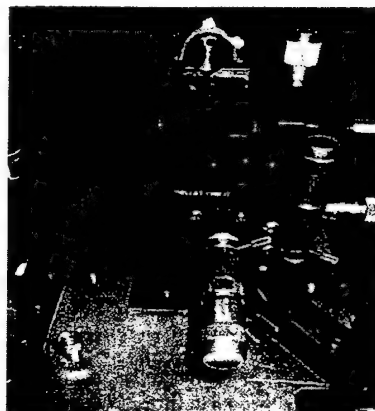


Figure 87: Collimator focused on sapphire diaphragm assembly.

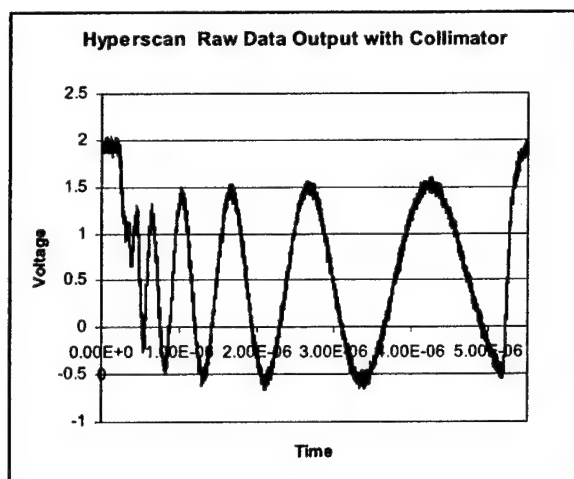


Figure 88: Erroneous Data from Hyperscan System with Collimator.

Luna decided to attempt to redesign the collimator to reduce extraneous reflections. The lens used in the new collimator design incorporates several features to eliminate the extra reflections. The lens features anti-reflection coatings on both optical surfaces. In addition, the lens has an eight-degree flat surface on the side facing the fiber to direct any reflection away from the core of the fiber. In addition, the collimator ferrule is polished to eight degrees to match the lens angle as shown in Figure 89. The collimator lens material and coatings are limited to operational temperatures of less than 409 °C.

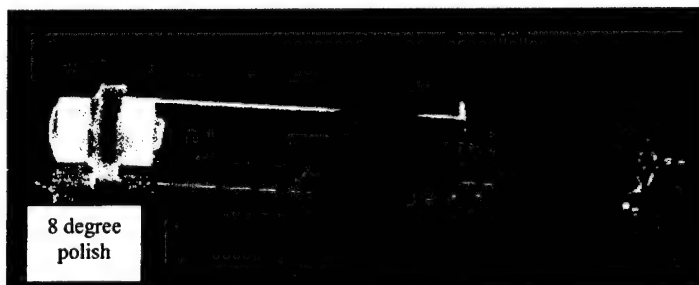


Figure 89: Fused Collimator Components.

The result was a reduction of the extra fringing by nearly a factor of four. The remainder of the extraneous fringing can be removed from the signal using a simple electrical filter. The Luna Innovations researchers investigated this possibility using a digital low-pass filter applied to captured data in post processing. Figure 90 shows the raw and filtered data from the Hyperscan system, interrogating a transducer with the improved collimator design.

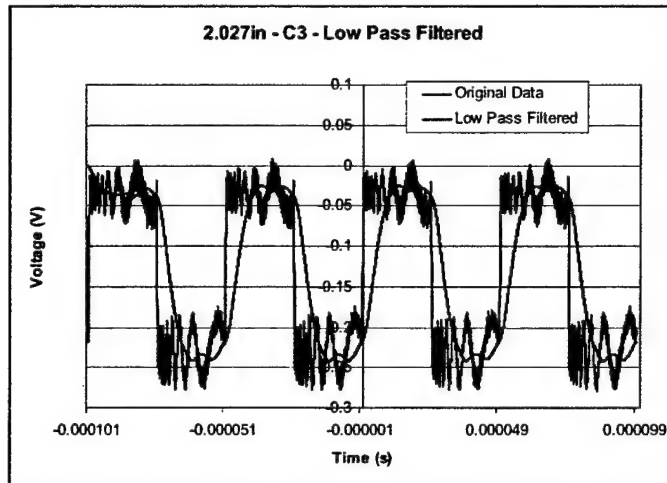


Figure 90: Raw and Filtered Hyperscan Data with Improved Collimator Design.

The new collimator design clearly improved the signal to noise ratio, however there existed enough phase change and ripple left in the data after processing that the researchers felt that too much error would result from taking this approach. The team then investigated multiple anti-reflection coatings for the sapphire diaphragm and fiber collimator components. The team could find no anti-reflection coatings that were operational at temperatures above 1000 °C. MgF, Gold, and layered dielectric coatings were all investigated and found lacking. The team decided to pursue a design without a collimator to simplify the optical approach and to use a ground surface (instead of polished) on the outside of the sensor to eliminate reflections extraneous to the two needed for pressure measurement in the high temperature parts.

5.1.2 Reflection reduction experiments

Goal - Attempt to eliminate two optical back reflections (R4 & R7, See Figure 91) for optimal performance of this remote sensor type with the Hyperscan system. And, to document and demonstrate the difficulty in passing a collimated beam through an unpolished sapphire lens.

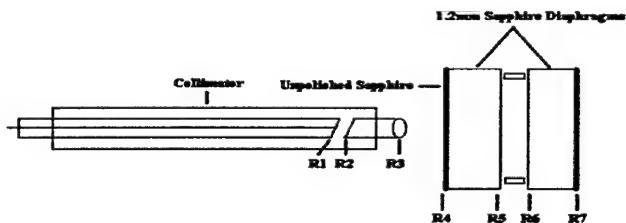


Figure 91. Collimator, window and diaphragm pressure sensor optical assembly

Our first test we determined we could get a quality reflection using a polished sapphire diaphragm with a cleaved fiber as the source lead. We used a diaphragm that was sealed to an alumina tube. (Approx. 150um thick) See Figure 92

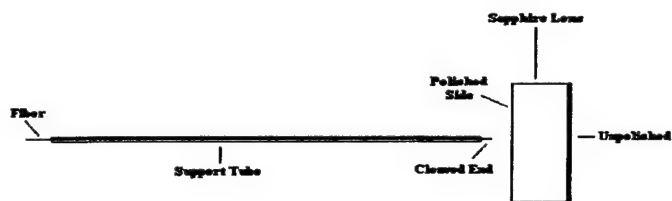


Figure 92. Simplified optics with unpolished (as ground and diffuse) reflector.

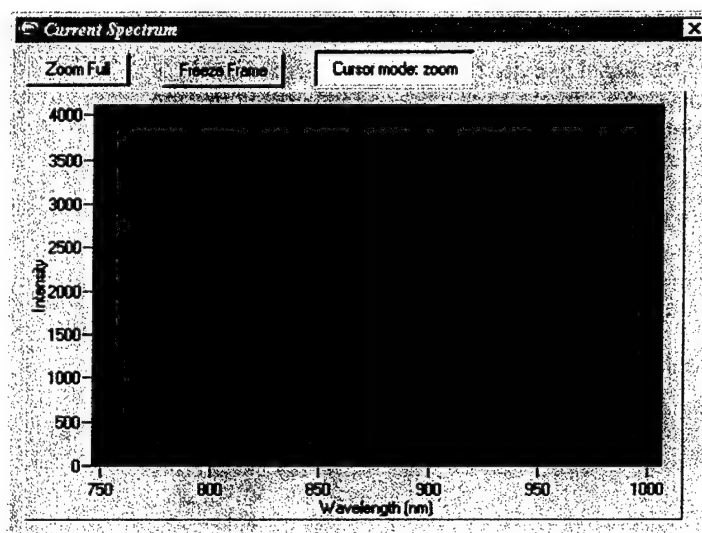


Figure 93. Optical Signal

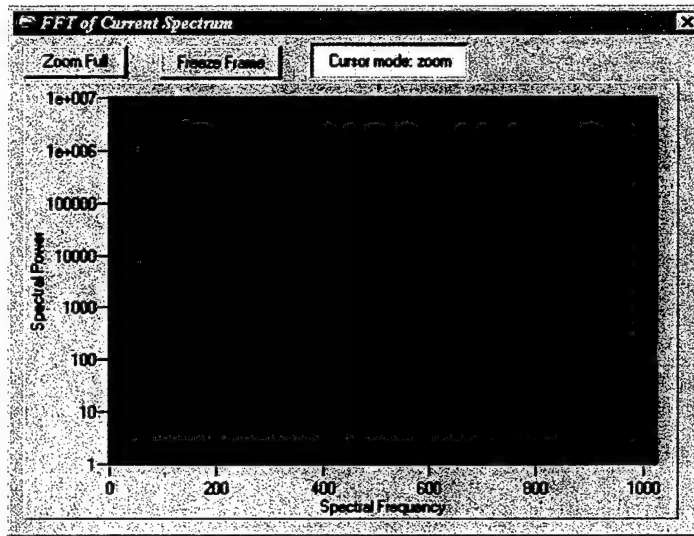


Figure 94- FFT of initial test.

For the second test we used the same procedure but substituted a diaphragm that appeared to have a small amount of crystal growth on the lens which made the surface slightly diffuse and was a byproduct of high temperature bonding attempts at Virginia Tech (Figure 92). Again we did achieve good results. The apparent crystal growth did not appear to have any effect on the fringes. The display was identical to Figure 93 and Figure 94

The third test used a diaphragm that had been scratched using a diamond scribe. Again with the cleaved end face we did produce a quality fringe pattern.

With our fourth test we replaced the cleaved end face with an 830nm collimator and repeated the prior three tests. See Figure 95

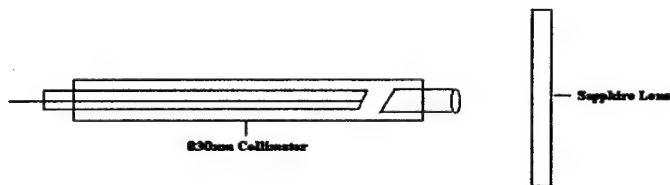


Figure 95. Collimator and scratched sapphire diaphragm

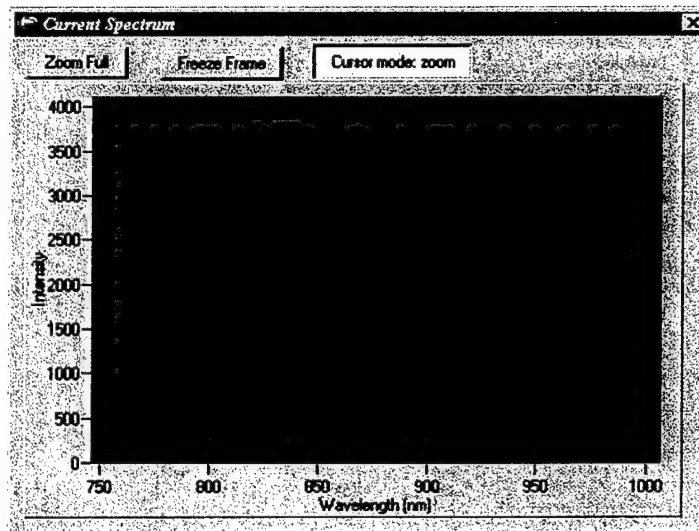


Figure 96. Diaphragm return signal – fourth test

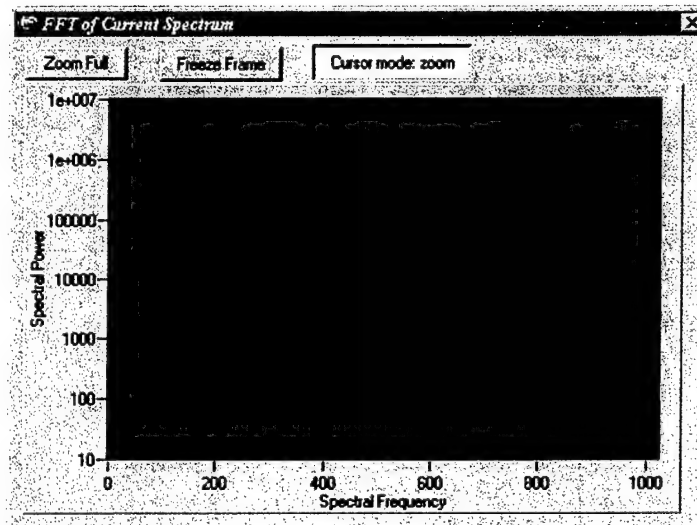


Figure 97 FFT of optical signal – fourth test

The tests using the regular and crystal growth diaphragms worked well (Figure 96 and Figure 97) but the test using the scratched surface did not. We could produce fringes with the collimator and lens nearly touching but the quality was very poor. See Figure 98 and Figure 99.

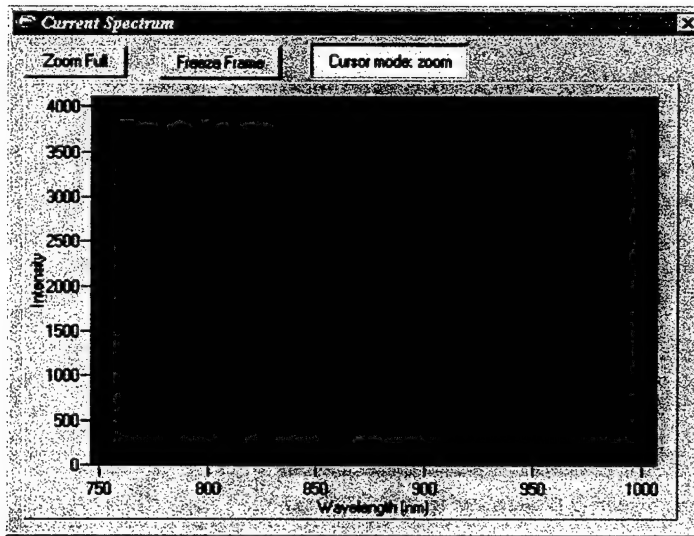
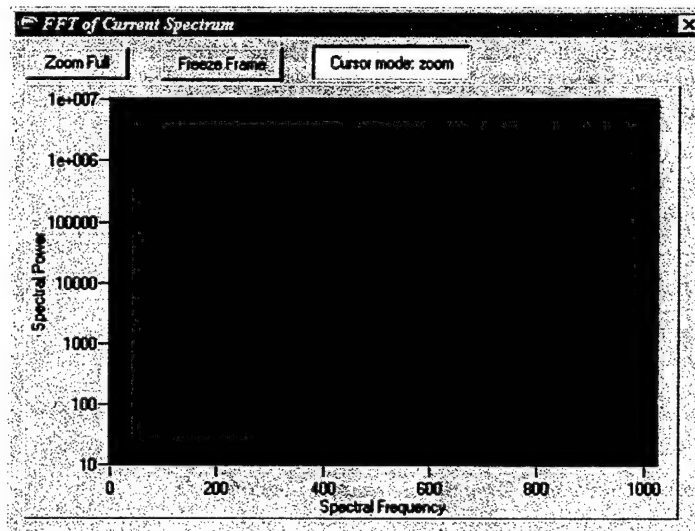


Figure 98. Optical signal return from scratched diaphragm and collimator assembly



In Figure 99 is a picture of the collimated beam used in test 4. Note how concentrated the beam appears when reflected off a polished diaphragm.

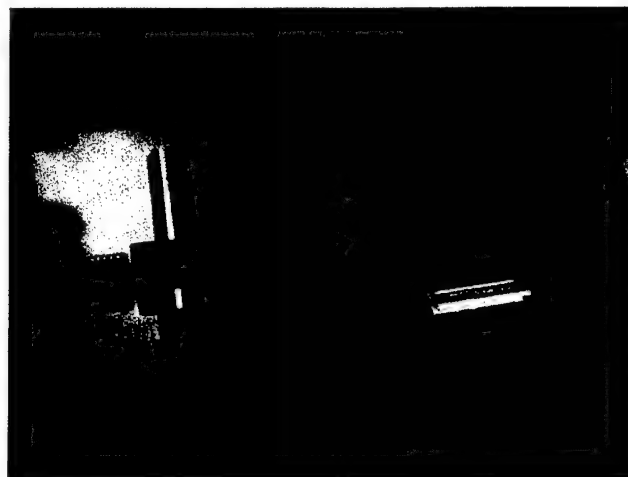


Figure 99. Polished diaphragm assembly illuminated with visible laser

For our fifth test we used the collimator and regular diaphragm leaving enough space between to insert a 1.2 mm thick sapphire wafer, as ground on both surface (unpolished). Figure 100. With the collimator aligned we rested the unpolished wafer on the alumina tube. We immediately lost all fringe contrast. See Figure 101 and Figure 102. When the unpolished wafer was removed the fringe pattern returned. See Figure 96.

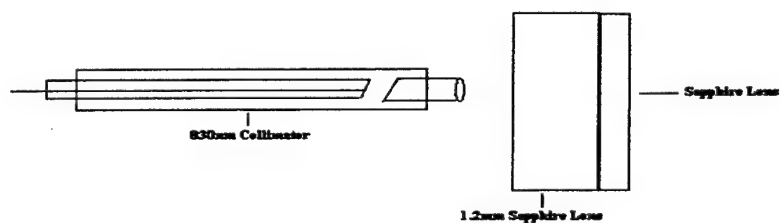


Figure 100. Collimator and diaphragm assembly for testing diffuse (unpolished) filter

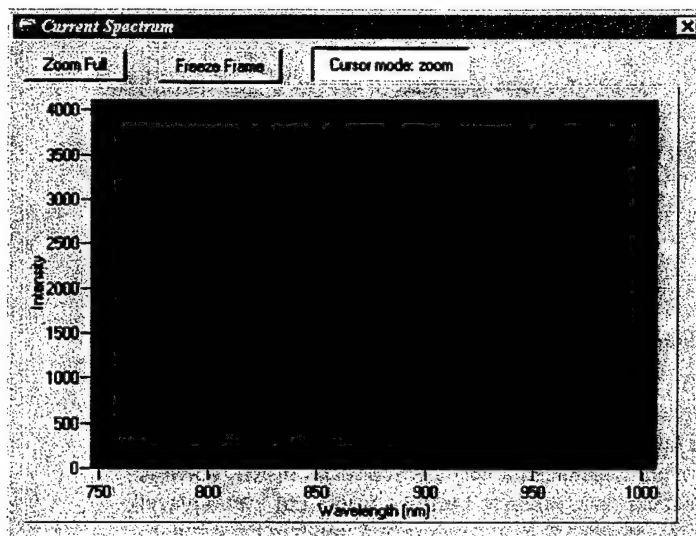


Figure 101 Optical signal – fifth test

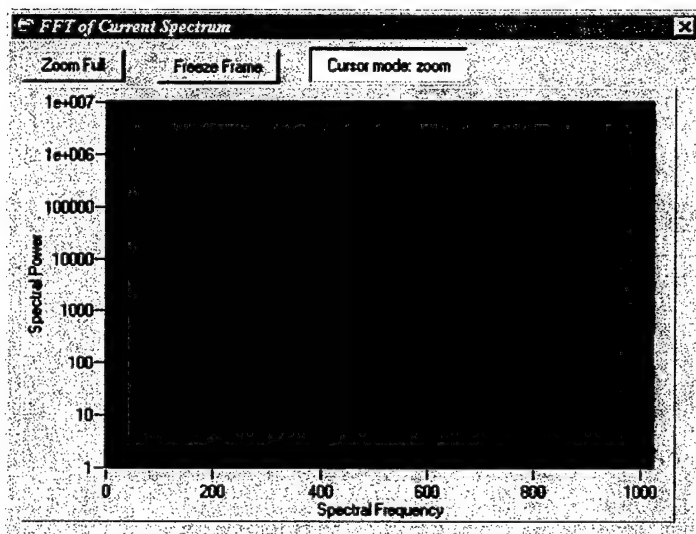


Figure 102. FFT – fifth test

Our sixth test we decided to introduce an air gap between the unpolished and regular diaphragm. We placed a 40um thick spacer between the two sapphire wafers and repeated the test with the same results. Figure 103 When the 1.2mm sapphire wafer is introduced we lost the fringe pattern. Figure 101

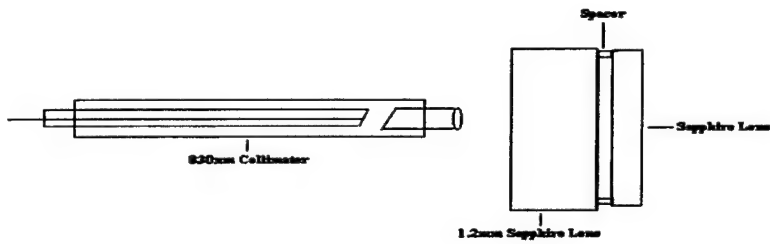


Figure 103. Collimator assembly – sixth test

With our next two tests we attempted to use refractive index liquids (RIL). The goal was to match as closely as possible the index of the sapphire and eliminate one of the diffuse surfaces. We used the same set up as test six but introduced a very small amount of RIL between the spacer and 1.2 mm lens. Figure 104 Great care was taken to limit the amount of liquid placed on the lens. The goal was to only have the RIL on the 1.2 mm sapphire and none on the regular lens. As before, when the 1.2 mm lens is placed between the collimator and the regular lens the fringe pattern is lost. Figure 101 We repeated the test twice with two different IR value liquids but results were the same.

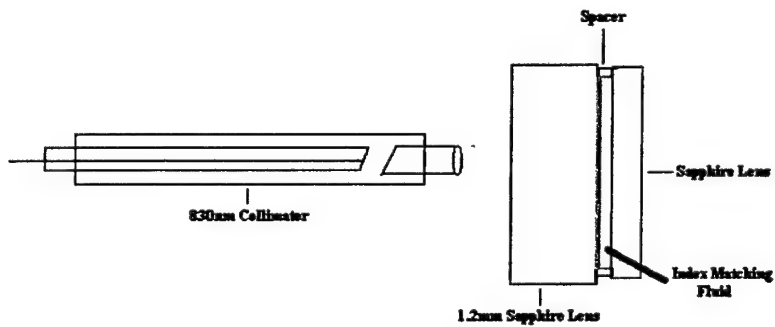


Figure 104. Collimator tests 7 and 8

For a ninth test we have taken several of the 1.2 mm lenses and polished one side until it was clear and smooth. The hope is the polished side will allow the beam to pass and aid in eliminate unwanted reflections. See Figure 105

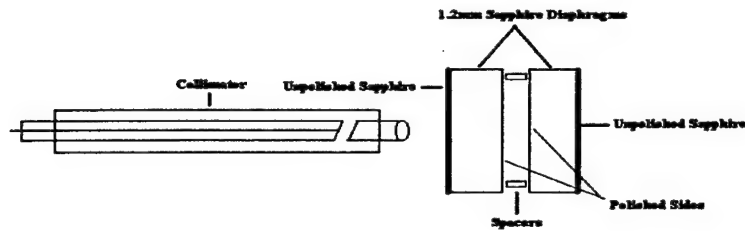


Figure 105. Collimator assembly – ninth test.

In each previous test we aligned the sensor with a polished diaphragm initially to achieve an acceptable fringe pattern. This test we attempted to align our reflection with an unpolished side of sapphire toward the collimator. See Figure 106

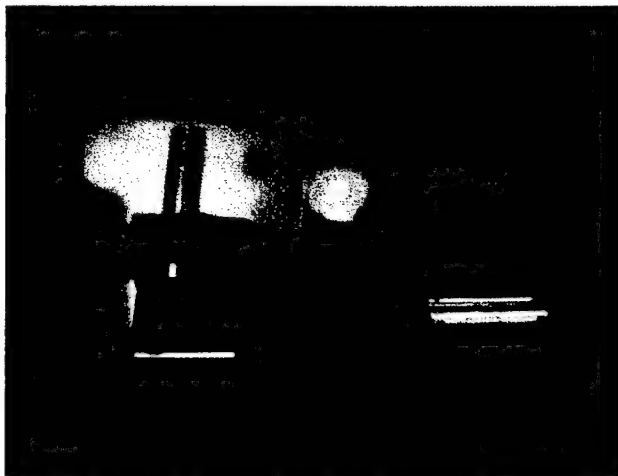


Figure 106. Unpolished assembly illuminated by He-Ne laser

Please note the distinct difference between Figure 106 and Figure 99. In Figure 99, the beam is being reflected off a polished surface. Figure 106 beam is being diffused and scattered off the unpolished wafer. Also note the illumination of the alumina tube in Figure 106. This not as distinct in Figure 99 and is further evidence of how adversely the unpolished sapphire surface effects the propagation of beam.

Many configurations have been attempted using a wide variety setups and methods to remove the unwanted reflections stated in our goal. Unfortunately with each test and many attempts, when an unpolished surface is introduced it simply renders the collimator unable to interrogate the sensor.

5.1.3 Thermal Compensation using Collimators

The use of a collimated system was investigated to remove the effects of thermal expansion on the data provided by the sensor. With a collimator the distance change caused by thermal expansion between the light source and the sapphire diaphragm would not be significant. This is because the system would interpret the displacement of the diaphragm based on a window reference point that is placed behind the pressure transducer.

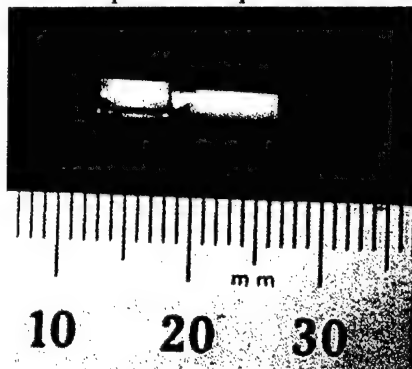


Figure 107. High temperature collimator bonded with silver paste.

Several collimators were constructed using fused silica ball lenses, zirconia sleeves and ferrules, and silver paste for bonding. These collimators are designed to fit snugly in the I.D. of the Sapphire tubes in the sensor design. The construction processes were examined and steps were taken to minimize the process, therefore, minimizing the chance of breakage during construction.

In addition to the two 800°C firing schedules that the collimators see during construction, one collimator was cycled to 800°C three additional times before breakage. The fiber failed at the back of the ferrule. This is the same problem that was occurring with the ferrule to fiber interface and bond in previous work. Figure 107 is an image of a high temperature collimator after

construction.

Luna has developed a method for constructing a fused collimator for the remotely interrogated pressure sensor. A fused collimator is shown in Figure 109. The collimator consists of a 1.8mm, fused silica ferrule and fused silica sleeve. The lens is an off the shelf part designed for telecommunications networks. The fiber is bonded to the fused silica ferrule by laser fusion. Similarly, the lens and ferrule are both bonded by fusion to the outer sleeve. The lens is constructed from high-index glass (high index of refraction). The upper limit of the assembly has yet to be determined, however, the lens of a fused collimator assembly did not survive an unintentional 600°C temperature excursion. This is not considered to be detrimental because the purpose of the collimator is to be set back from the "hot zone." In addition, the collimator ferrule is polished to eight degrees to match the lens angle as shown in Figure 108.

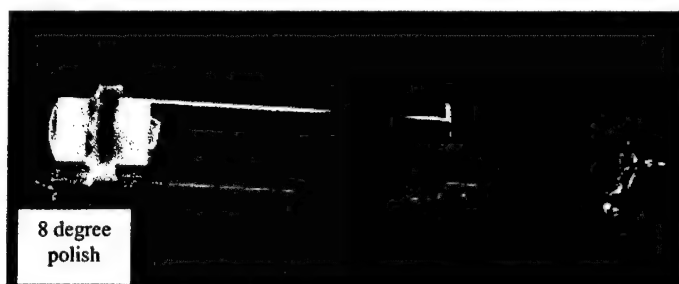


Figure 108: Fused Collimator Components.



Figure 109: Fused collimator assembly.

5.1.3.1 Collimator Testing

Two collimators were tested using an 850 nm source. Images of the projected spot were acquired at a distance of 50 feet and subsequently analyzed to obtain beam profile and spot size information at various ambient temperatures from room to 800°C. The profile of the beam at each temperature is shown in Figure 110 for collimator #1.

The profiles of the beam were fit to a Gaussian function to determine $1/e^2$ spot size. Figure 111 shows spot size vs. temperature for both collimators. Measured data is consistent with the qualitative observation that while collimator #2 appeared to be better collimated at room temperature, it lost collimation at a lower temperature than did collimator #1. From the graph, it appears that indeed, collimator #2 was adjusted for optimum collimation somewhat below room temperature, while collimator #1 exhibited optimum performance between 100 and 200°C.

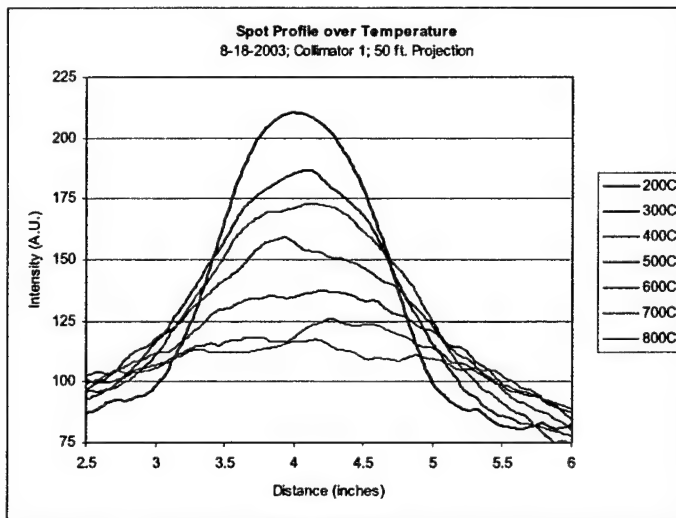


Figure 110. Projected spot profiles (50-foot projection distance) for collimator 1 at various ambient temperatures.

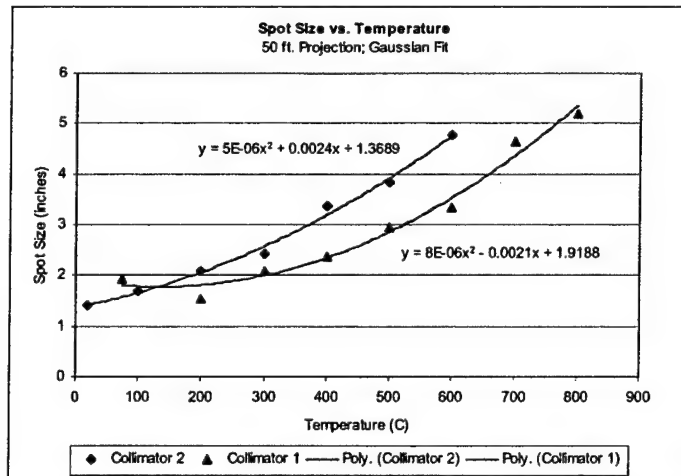


Figure 111. Spot size vs. temperature for 2 collimators, and corresponding quadratic fits.

Several collimators survived high temperature testing where the sensor transducer (Sapphire diaphragm) was taken to temperatures over 1400 °C with a propane and oxygen torch. The transducer assembly was mounted on a stationary stand made of refractory brick so that the diaphragm could be heated. The setup is shown in Figure 112 and Figure 113. An S type thermocouple was utilized to monitor the temperature at the transducer.

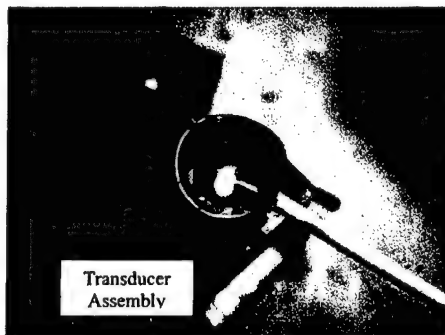


Figure 112: High Temperature Testing of Collimator and Transducer

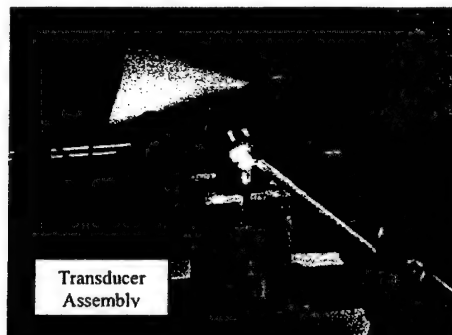


Figure 113: High Temperature Testing of Collimator and Transducer.

Collimator # 6

Collimator #6 was tested in several different manners. To verify the proof-of-concept for measuring temperatures up to 1400°C, the collimator and transducer assemblies were tested without the final attachment. Secondly, because bonding with the epoxies was not successful, glass frit (or solder-glass) was used for the final attachment between the collimator and the alumina tube. The sensor was bonded for the final testing.

Collimator #6 was mounted in the five-stage mount so that it could be actively aligned during the test. This would show the sensor's capability of measuring high temperatures separate from the final packaging. The transducer assembly was mounted on a stationary stand made of refractory brick so that the diaphragm could be heated. The setup is shown in Figure 112.

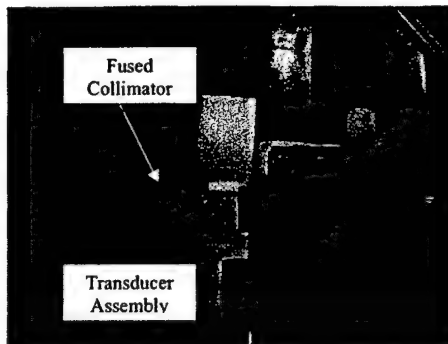


Figure 114: Side view of the non-contact test setup

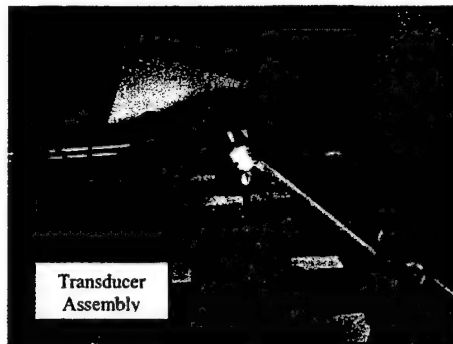


Figure 115: Front view of the non-contact test under way.

Collimator #6 Results

The results from the non-contact tests with collimator #6 are shown in Figure 116 through Figure 118. The red line indicates the thermocouple temperature on the right vertical axis. The blue line shows the gap data collected with the fiber optic sensor, quantified on the left axis. During these tests, the collimator was attached to the five-stage mount so that adjustments could be made during the testing. As discussed earlier, it was noticed while the flame was directed onto the sapphire diaphragm; the fringes would seem to disappear. However, when the heat was removed, dramatic change was observed and the fringes would immediately return. When the thermocouple reading spiked, the gap data would decrease, indicating potential misalignment. Once the heat was reintroduced, the fringes would return to full strength. Examples of the fringe patterns are shown on the graph.

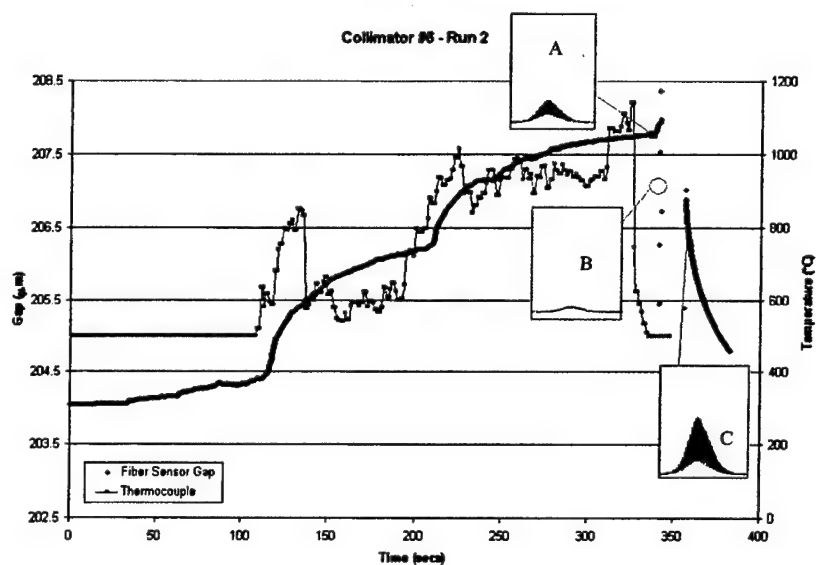


Figure 116: Collimator #6, Run 2. Maximum temperature 1142°C (thermocouple reading).

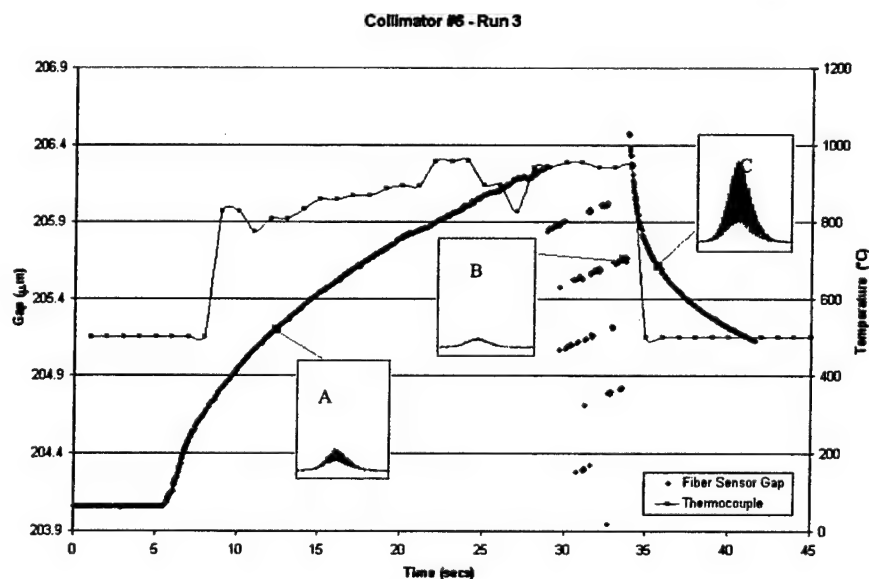


Figure 117: Collimator #6, Run 3. Maximum temperature 959°C (thermocouple reading).

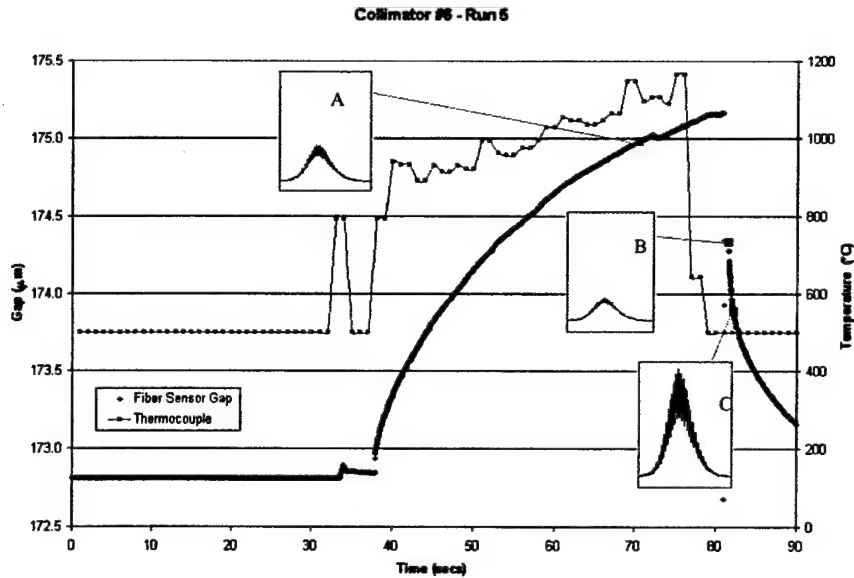


Figure 118: Collimator #6, Run 5. Maximum temperature 1164°C (thermocouple reading).

During Run 8, the collimator was actively aligned by a technician when the fringes decreased in quality. The heat was held on the sensor during the entire test. The thermocouple was used to monitor the temperature during the test. With the active alignment a quality signal was achieved at approximately 1600°C as in Figure 119. However, the complexity of the mounting method and the presence of thermal gradients prevented the collimator assembly from being aligned with the sapphire diaphragm across the entire range of experiment temperatures.

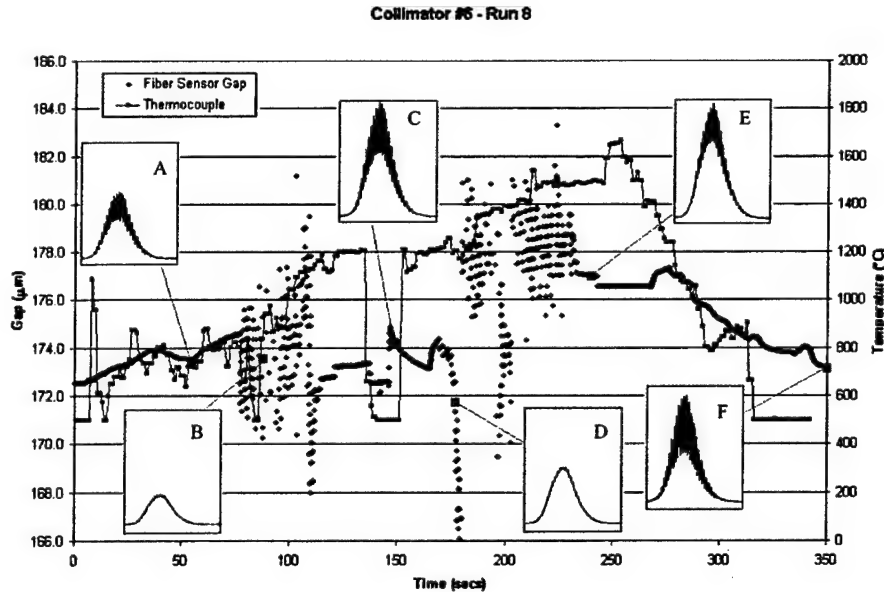


Figure 119: Collimator #6, Run 8. Maximum temperature 1667°C (thermocouple reading).

5.1.4 Thermal Compensation by Means of Material Sizing and Selection

One goal of this project was to design and build a pressure sensor that is thermally compensated for all temperatures. This would make it possible to have reliable pressure data that does not need to be corrected based on differing temperature environments. Research and modeling were extensively used to predict the expected expansion of the materials during an increase in the local temperature of the sensing environment. The materials selected for sensor construction have differing Coefficients of Thermal Expansion (CTE) which will cause different magnitudes of length change as temperatures increase. A model was created to calculate the expansion of the sensor components relative to the change in temperature. The goal of this evaluation is to determine the

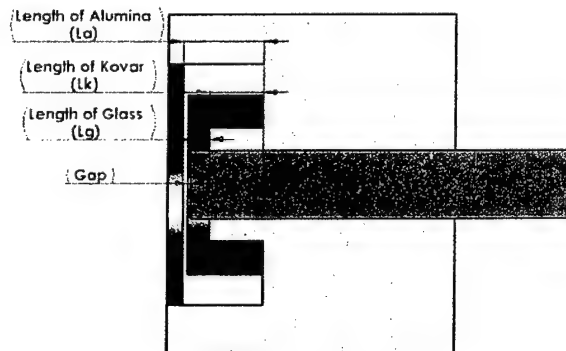


Figure 120. Profile of sensor tip used to calculate thermal expansion

optimal lengths of the components that will minimize the change in the measured gap by the fiber optic sensor. This development if successful, would lead to a thermally compensated sensor that is not affected by temperature changes in the sensing environment. There are three different materials that are being used in the construction of the heat-affected region of the sensor that directly affect the gap between the fiber and the sapphire diaphragm. Figure 120 shows each of the components and their respective locations within the sensor.

The model used to calculate the optimal magnitude of each part length is in the form of a linear equation relating the four distances and setting their sum equivalent to zero. The resulting equation is shown below:

$$(L_a + (L_a)(CTE_a)(T)) - (L_k + (L_k)(CTE_k)(T)) - (L_g + (L_g)(CTE_g)(T)) - Gap = 0$$

When this equation was evaluated using an Excel spreadsheet an optimal length for each material was obtained that would account for material handling capabilities and provide a sustained gap for a predetermined temperature range. The CTE's of the three materials differ significantly at similar temperatures causing a nonlinear progression of the gap to the elevated temperature. Kovar's CTE is also nonlinear and increases above a temperature of 700°C. Figure 121 is a plot of the CTE's of the materials used for the sensor construction.

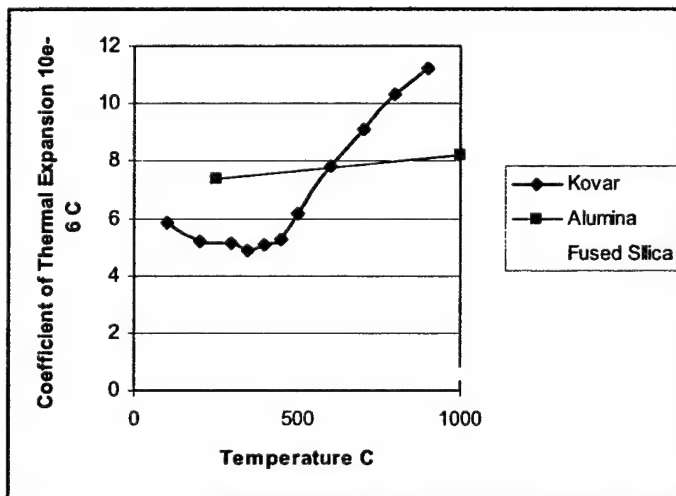


Figure 121. Coefficient of Thermal Expansions for Relative Materials

This causes the Kovar to expand much more rapidly than the Fused Silica of the Alumina resulting in a parabolic curve of the gap between the limits of the temperature range as shown in Figure 122.

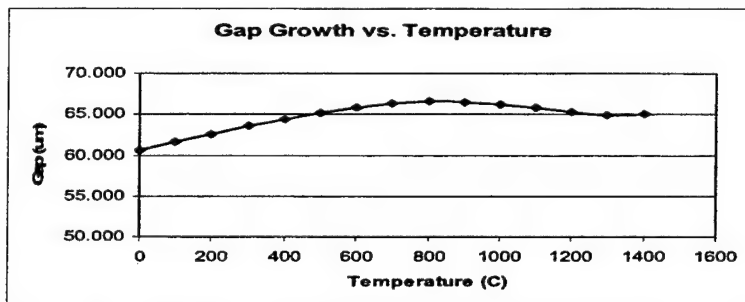


Figure 122. Gap profile for a sensor with a temperature range between 1200 and 1400°C

The final result of the modeling and subsequent testing revealed that it is not physically possible to construct a sensor that is thermally compensated for a large range in temperatures. Instead, it is much more feasible to design the pressure sensor for operation in a specific temperature range that spans approximately 400°C. At significantly elevated temperatures, a smaller temperature range (approximately 200°C) is necessary to account for the exponential increase in the CTE of the Kovar material. Other materials were also evaluated but were not feasible for use in the construction of the pressure sensor.

Therefore, a temperature compensation package for the sensor has been designed utilizing a collocated thermocouple for active temperature compensation. Additionally the Luna team added a fused silica EFPI pressure sensor (capable of 450 °C operation) for static measurement. When the sensor is used in this configuration, the static pressure and temperature can be used in a demodulation algorithm to provide high frequency pressure data that is unaffected by the thermal expansion of the sensor materials. The sensor and thermal compensation package are shown in Figure 123.

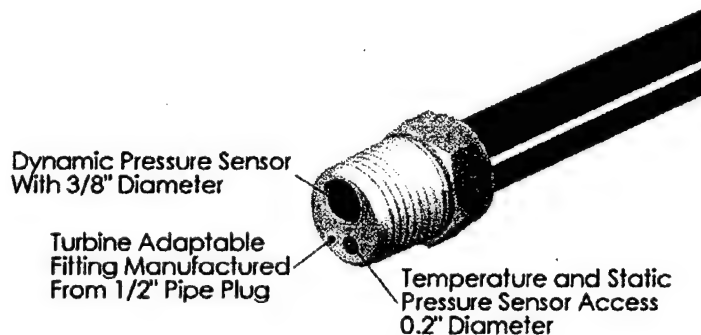


Figure 123. Thermal Compensation Package for high temperature, pressure sensor

This package consists of the dynamic pressure sensor mounted in a 1/2" NPT machined pipe fitting. The pipe fitting also has access for a media isolated thermocouple and a static pressure

port. The pressure port can be configured to match the frequency limits of Luna's FiberProUSB2 (1000Hz) by setting its length to 2.75 inches (69.85 mm).

5.2 Development of the Fused Ferrule Design

The original concept included the use of a high temperature silver adhesive to bond the optical fiber into a small supporting section of fused silica capillary tubing. Extensive testing resulted in a failure of the silver to maintain the integrity of the optical fiber during the curing process.



A
parallel
path
was

Figure 124. Early iteration of the fused ferrule design

investigated using a Propane-Oxygen torch to fuse the optical fiber to the capillary tubing to create an all fused silica collimator. The fused silica collimator will have negligible thermal growth, as the CTE of fused silica is $1/20^{\text{th}}$ of the CTE of zirconia. This proved to be successful and raised the temperature limit of the fiber/ferrule assembly from $\sim 870^{\circ}\text{C}$ with the silver to $\sim 1000^{\circ}\text{C}$. This process was also more repeatable than using high temperature silver adhesive, yielding better results. Figure 124 shows a piece of capillary tubing that was fused to a fiber using the Propane-Oxygen torch.

Further refinements to the sensor design included increasing the length of the fused ferrule assembly. The fusing of longer sections of capillary proved difficult to control with the torch method. Development of a new fusing method was undertaken using a CO_2 laser at MOOG (formerly Northrop Grumman Polyscientific of Blacksburg, Va) this method produced very good results and the fused ferrules manufactured have been used to measure pressure at temperatures of 1000°C during testing for a related project.

5.2.1 CO₂ Laser Fusion Process

A process has been developed that will consistently yield fused fiber/ferrule assemblies using a CO₂ laser. The ferrule is prepared by cutting the capillary tubing to the desired length and cleaning it in an isopropyl alcohol bath. The fiber is then prepared by removing the coating at a length ¼" greater than the length of the ferrule using a plasma cleaning method. The length of cleaned fiber is inserted into the ferrule and potted with Turbo-R high temperature sealing adhesive, adding strength and stability to the fiber-ferrule joint. Once the assembly is secured to the laser platform and aligned, 10 to 12 passes with the laser are made until the fiber and ferrule are fused. This process is repeated on a length 180° around the circumference of the ferrule. After the ferrule assembly is fused the face is polished and the assembly is ready for insertion into the sensor housing. Shows the fused ferrule assembly after it has been fused.

The goal of the second-generation sensor was to build on previous experiments and incorporate a completely fused collimated beam with an alumina tube/sapphire diaphragm assembly and collect data at temperatures of 1200°C and higher.

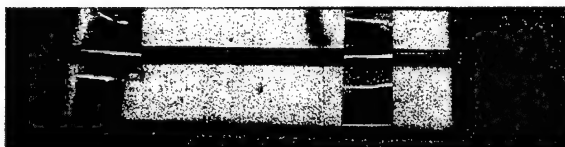


Figure 125. Ferrule and fiber assembly fused using a CO₂ laser

The first step in the process was to insert a fiber into a 1.8 mm diameter silica ferrule. To allow for insertion the pyro-coating was from the fiber using a plasma cleaning process. After inserting the fiber into the ferrule, the fiber was secured in place with a small amount of 353 NDT epoxy. The ferrule was taken to Moog Components, located in Blacksburg, VA, for fusing. At Moog a 50-watt CO₂ fusion lathe welding system was used to fuse the fiber with the ferrule, see Figure 126.

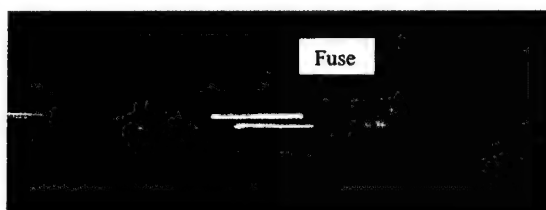


Figure 126: Fiber fused into a silica ferrule.

After successful fusing, the ferrule must have an 8-degree polish. This will direct any reflected light away from the fiber core. To achieve this we use a specialty polishing puck and standard polishing procedures, see Figure 127. After polishing the assembly was checked to ensure quality, the ferrule assembly is examined under a microscope and then attached to a HeNe laser to interrogate the quality of light transmission as in Figure 128. The goal is find the point at which the beam or spot of light is at its smallest and clearest. The two main factors affecting light quality is the distance between the lens and ferrule inside the tube and the rotation of lens. Once the desired insertion distance is found, the tube is gently rotated to the point at which the

beam / spot appears to be the best. At this point, the beam should resemble that of a laser pointer, see Figure 128.

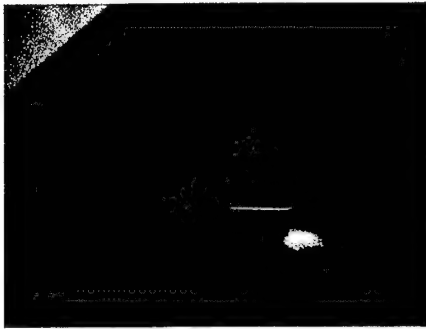


Figure 127: Polishing of the "long ferrules".



Figure 128: HeNe laser was used to verify light transmission and quality.

Each collimator is mounted on a five-axis stage in order to test the collimator performance with a transducer, see Figure 129. Using the micro-position dials on the translation stage, the collimator is gently moved in the X and Y directions. Once the He-Ne spot is close to center of the diaphragm, the sensor can be attached to the FiberPro system, which uses an 830nm light source. The leading and trailing faces of the sapphire diaphragm with respect to the collimator create a fringe pattern. This fringe pattern is related to the interference between the two waves on the return reflection of the two sapphire faces. The sapphire has a fundamental material property, CTE, which is sensitive to temperature. As temperature changes adjacent to the sapphire, the physical and optical distance between the faces will change. This effect can be detected with the FiberPro demodulation system developed by Luna. The collimator is adjusted with the five-stage axis to obtain the best fringe pattern, see Figure 130.

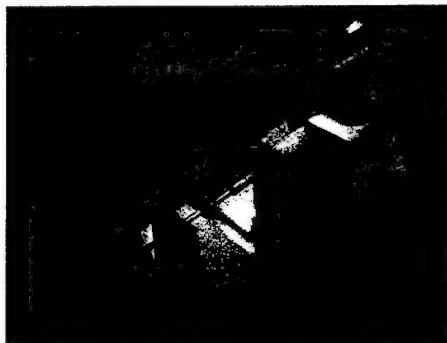


Figure 129: Collimator aligned with the transducer assembly.

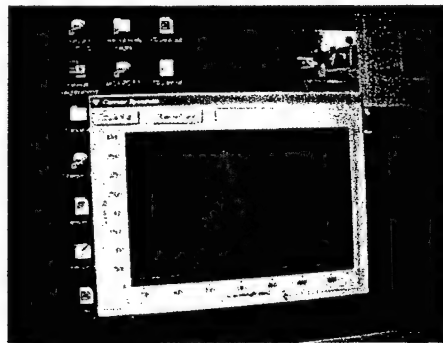


Figure 130: Fringe pattern viewed with the FiberPro hardware and software.

5.3 Material selection

The temperature requirement of 1400°C, the bonding methods and the Mechanical property interactions between the materials were taken into consideration in selecting the appropriate materials for sensor construction. For these reasons, the materials selected for the individual sensor components and the bonds between them must be compatible and capable of surviving in a harsh, high temperature environment. Several materials were considered for use in manufacturing the sensor tip shown in Figure 131. Each of the materials was evaluated based on cost, machinability, and their respective thermal and oxidation properties. The materials under consideration consisted of Kovar, Inconel X750, and PM2000. Table 1 shows a comparison of the different materials.

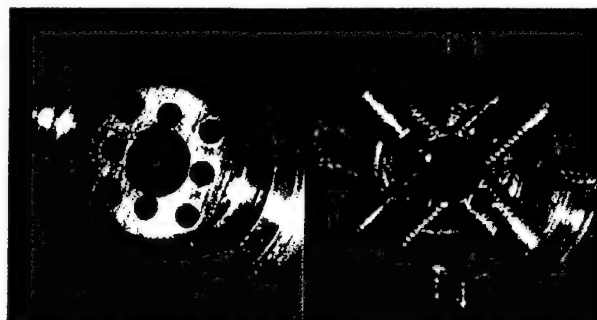


Figure 131. Sensor Tip Front and Rear views respectively

SS316 and Alumina were included in the table as a comparison of thermal properties and bonding capabilities. The ability to form a hermetic bond between the Alumina and the tip material is essential to accurate operation of the sensor. During previous testing it was found that Kovar could not maintain this bond due to the severe oxidation that forms without being

Table 1. Material Selection Chart

		SS 316	Inconel 750	PM2000	Kovar	Alumina
Corrosion Resistance		Poor	Good to 700	Excellent	Good at resisting corrosion good however, oxidizes heavily at elevated temperatures	
Cost			13.76 /ft .25dia	111.76 /ft .236 dia	41.67 /ft .25 dia	
Availability		Easy to Obtain	Easy to Obtain	3-4 week lead time	Available In House	
GTE @ 760C	(/G)	19	14.6	14	9.6	8.4 (3000C)
Machinability		2	3	4		3
Melting Point (C)		1390	1390 - 1430	1483		1450
Thermal Conductivity @760 C	(W/m-K)		35.3	22.5		17.3
Weldability			Excellent	Grainsize 4 ³ Better than 6 ⁴	good possibility of cracking after cycling	
Notes: PM2000 has a strongly adhering layer of Aluminum Oxide form at high temperatures Machinability Scale 1 = easier than SS316 2 = same as SS316 3 = Slightly Harder than SS316 4 = Harder Than SS316						

subjected to nickel passivation. Kovar does however have a similar CTE as Alumina. Consultations with Aegis Scientific yielded that Aegis possessed the capabilities to bond to all of the materials under consideration and that the bond would remain hermetic up to the desired temperature. The PM2000 appeared to be ideal due to its corrosion resistance and the fact that it would not require passivation. This material is very expensive and must be acquired from an overseas vendor. Due to time, cost constraints, and a high minimum order no PM2000 was used in the manufacturing of sensor components. Inconel was ruled out for use due to the large CTE mismatch between the alloy and Alumina. For the reasons stated the Kovar was the best available option to use for sensor construction.

5.4 Related Work: Optical Fiber High Temperature Survivability

In related work, it had been found that SMF-28 fiber began to develop high attenuation during long-term exposure to temperatures approaching 1100°C. Tests were then conducted at 1050°C and 1000°C to form a model of fiber attenuation at various temperatures. This characterization is important, as the next phase of testing involves testing of distributed Bragg sensors at elevated temperatures, and it is necessary to know the contribution of signal degradation due to fiber attenuation at those temperatures.

Curiously, it was found that the 1050°C exposure caused the fiber to degrade more rapidly than the previous test at 1100°C. After careful examination of the testing conditions, it was observed that the temperature in the 1050°C test was ramped directly to the end point much faster than in the previous 1100°C test, for which the furnace arrived at the final temperature after a series of steps with long dwell times at lower temperatures. From these results, it was concluded that degradation of the fiber is a function of three major variables – temperature, exposure time, and ramp time.

To get a better idea of how these variables are related, we performed a series of tests on SMF-28 fiber with controlled ramp times ranging from 1°C/min to 20°C/min, starting at room temperature and ending at a final temperature of 1065°C. At 20°C/min, the degradation appeared to be a function of final temperature. Ramp rate, however, seemed to be the primary factor determining whether the fiber would ultimately fail, as seen in Figure 133. In this graph, there is an anomaly, in that the 3°C/min rate caused failure, while the 5°C/min rate did not. It appears that the threshold of short-term failure is in this ramp range, and that failures occur statistically, as further testing resulted in survival at 3°C/min rates and failure at 5°C/min. Interestingly, after the fiber was tested at 1°C/min and returned to room temperature, it was later ramped at 20°C/min and survived for 24 hours, suggesting that pretreatment of the fiber may enable operation at even higher temperatures.

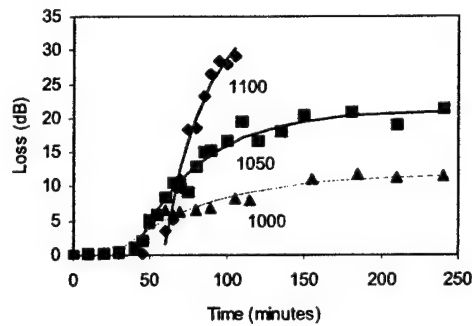


Figure 132: Loss as a function of final temperature for SMF-28 fiber subject to 20°C/min ramp

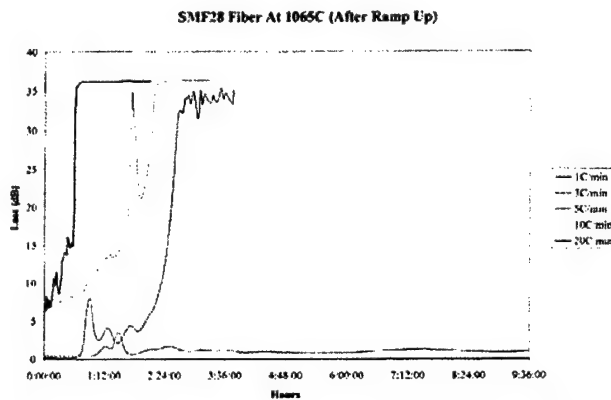


Figure 133: Controlled-ramp high-temperature testing of SMF-28 fiber. Note that time zero is the point at which the set temperature is reached in all cases.

6. Sensor Construction Procedures and Challenges

6.1 Hermetic testing

It is imperative for proper sensor operation that hermetic seals be achieved at all of the sensor joints. The most delicate of the bonds used for the sensor construction is that between the Alumina tube and the sapphire diaphragm. This is also the location that has proven to fail the most often during the construction process. Stresses developed during the Aegis process along with the uneven thermal stress induced during the two circumference welding processes has been known to cause a failure in the bonding material and cracking across the face of the sapphire diaphragm. Either of these failures results in a lack of hermeticity of the sensor and will yield inaccurate data.

The first method to test the sensor tips once received from Aegis, a slight pressure is applied to the back of the diaphragm and the assembly is submerged in water. If there is a breach in the seal between the diaphragm and the Alumina tube, a flow of bubbles will appear to stream from the seal. A second method that has proven to be as accurate as the submergence method is a non-destructive dye test. A small amount of dye is placed around the diaphragm seal and observed under a microscope. The dye will wick into any areas not covered by the bonding agent revealing sections that may not be hermetic. Shows three parts received from Aegis scientific and checked in this manner.

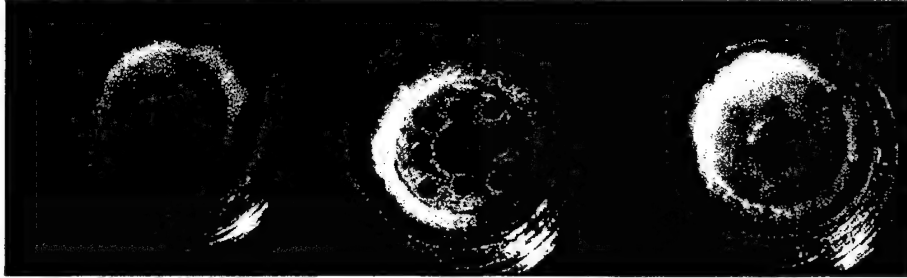


Figure 134. Parts tested for hermeticity using the dye method. 08Aug04

When subjected to the dye interrogation method, the two assemblies on the left revealed several areas that were not hermetic. The assembly on the right proved to have a hermetic seal and could be used for further sensor construction. The cause of the failure on the first two assemblies is believed to have occurred during the initial construction. These parts were manufactured at the same time and the pressure distribution on the face of the diaphragms was not believed to be consistent across the surface area. Further research will be conducted by Aegis scientific to improve the tooling used during construction of these parts in order to have a higher success ratio.

Comment: All the captions and cross-references from here on need to be fixed !!!

In the event that parts are manufactured and are not hermetic, a method of reclamation was developed which places the parts in an acid bath capable of removing the bonding agent while allowing the individual parts of the assembly to remain in tact. This will allow for future recovery of parts and for re-manufacturing capabilities of those parts.

6.2 Welding development

Vital to the construction of a working sensor is the welding of the tip assembly prepared by aegis scientific to the remainder of the housing. During this procedure it was necessary to minimize the heat flux into the part so as not to damage the bond between the sapphire and the Alumina by inducing thermal stresses. The amount of heat flux into the part was controlled by varying the amount of current used to perform the welding process. A water-retaining polymer heat sink was also placed onto the diaphragm and around the housing to absorb the heat energy before it could corrupt the Aegis ceramic solder bond. The procedure that would accomplish this objective consisted of a series of pairs of spot welds placed onto the part 180 ° apart. Each spot weld would then overlap the preceding spot weld and eventually the entire circumference would be welded.

Testing was done to refine and verify the developed procedure that would minimize the amount of heat flux into the part while still achieving the desired weld penetration.

The welding test was conducted by acquiring several bonded test coupons from aegis scientific and varying the amount of current used to perform the spot welding. Hermeticity was then checked by submerging the welded tip in water and applying pressure to the diaphragm. Areas where the tip was not sealed were identified by escaping bubbles from the housing.

The weld current was initially 50 amps for a period of 5 ms. These settings proved to be effective in joining the tip assembly to the 316 stainless steel housing by providing sufficient penetration to ensure a strong weld between the parts. Penetration was inspected by cross sectioning the welded part and submitting it to an etching compound composed of 1 part HNO₃, 1 part HCl, and 1 part De-ionized water.

The weld appeared to penetrate approximately 40% of the wall thickness of the outer housing. Several further trials were conducted on test coupons with sapphire diaphragms bonded by aegis scientific. After each complete weld the assembly was checked for hermeticity. Inspection of the welded assemblies revealed that cracking was occurring causing the seal to be easily permeable by the gas used to check for hermeticity. Evaluation of the process revealed that this cracking was likely being caused by the rapid cooling of the metal pool created by the strong welding

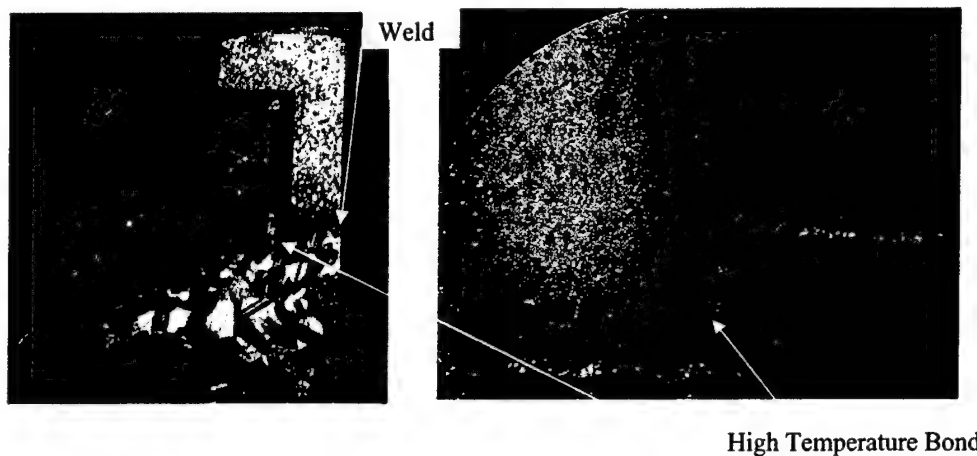


Figure 135. Cross sectioned and etched sensor tip.

current. The rapid cooling constricted the metals forming cracks between the parts. This problem was addressed by increasing the duration of the arc to 25ms. After this change was made in the procedure, future welds did not experience the cracking phenomena. From this testing it was found that the ideal current to apply the spot welds was 50 amps for a period 25 ms. Each spot weld overlapped by 60% the previous weld to ensure hermeticity. This process was used to weld the actual sensor parts.

6.3 Sensor Construction

The sensor was constructed by temporarily assembling the sensor and measuring its overall length of 8.74". A mark was made on the outer housing tube to indicate the maximum allowed length and the outer tube was cut using a precision lathe. A supporting washer was placed 1.5" from one end of the inner tube and spot welded as shown in Figure 136.

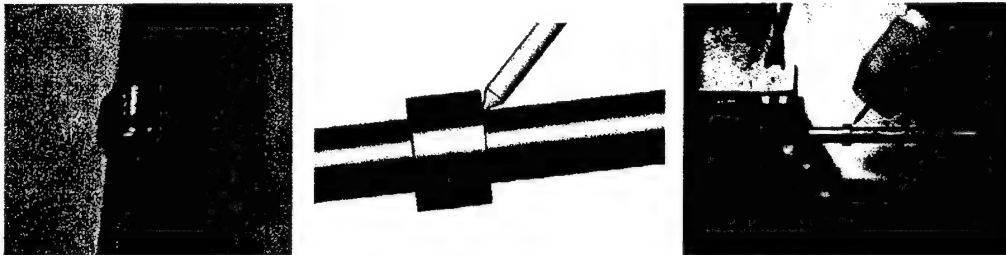


Figure 136. Welding of the inner tubing supporting washer.

For this weld a current of only 30 amps was necessary to achieve the strength between the two parts due to the reduced thickness of the inner tubing compared to that of the outer tubing. The welding torch was also placed at a 45 angle so that the tip could strike an arc on the side of the washer and allow the molten metal to flow and mix on the stainless steel inner tube. The washer was spot welded on one side in eight equally spaced places.

The next step was to weld the inner tube to the sensor tip assembly. This was done in the same manner as the washer was welded with time provided for the assembly to cool completely before attempting to place another spot weld. This ensured that the part would not overheat and the bonds would remain intact. Figure 137 shows the tip welded to the inner tubing.

Once the inner tube had been welded the assembly was fitted into the outer housing tube. Care was taken to ensure that the parts fit to a close tolerance to increase the quality of the finished weld. The outer housing was placed into the welding lathe and the diaphragm assembly was liberally covered with the water retaining polymer. Figure 138 shows the welding process with specific attention paid to the location of the torch tip at the point where the two materials meet.

The housing was tested for hermeticity after the tip was welded by submergence in water and having pressure applied to the rear. The pressure was applied beginning at 0.5 psi and increased in increments of 0.5 psi until a maximum of 5 psi was reached. Further increases in pressure would place the diaphragm assembly at unnecessary risk of failing under tension, a condition which it would not normally see during operation.

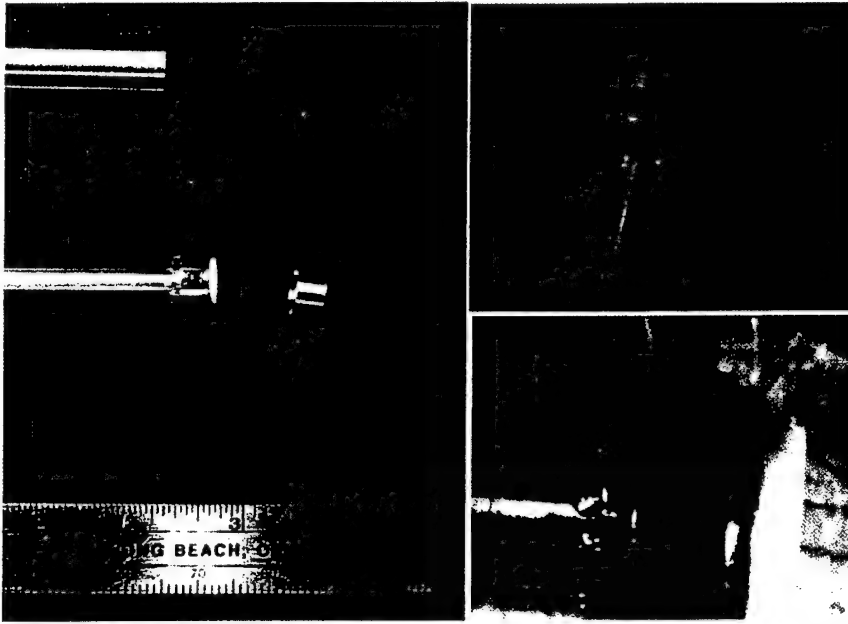


Figure 137. Clockwise from the left: Sensor components before assembly, Tip assembly welded to the inner tube rear view and side view.

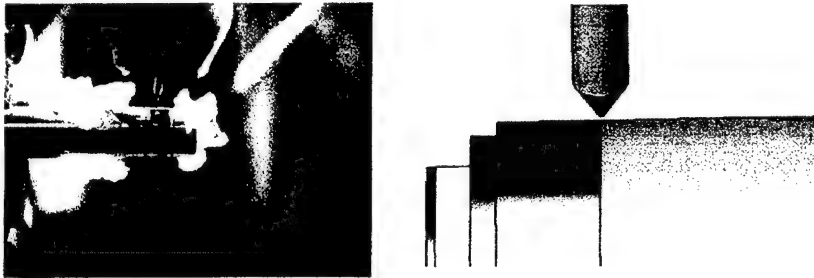


Figure 138. Welding setup of the tip assembly to the outer tube.

A retaining cap was then welded to the sensor assembly that serves as a safety retaining component in the event that any of the ceramic-to-metal or Alumina-to-sapphire bonds fail. This feature would prevent the ceramic assembly from traveling through the engine turbines in case of failure, but would not significantly affect frequency response. This weld was performed identically to the weld performed between the sensor tip and the outer housing. The sensor was checked again for hermeticity before the ferrule was inserted (Figure 139).

The final step in the construction process was to insert a silica ferrule that has 2 m of 1300 nm fiber inserted and fused inside. The fiber is reinforced with 353 epoxy at the rear where the

ferrule and fiber interface initially. The ferrule is inserted into a section of stainless steel tubing and secured with phenylsalicilate. The tip of the ferrule is coated with a silver bonding paste and inserted into the sensor housing. The silver paste is then cured according to an optimized, factory provided curing schedule. Successful completion of this step finalizes the construction of the sensor and readies it for testing at the Luna facilities and then in a turbine engine.

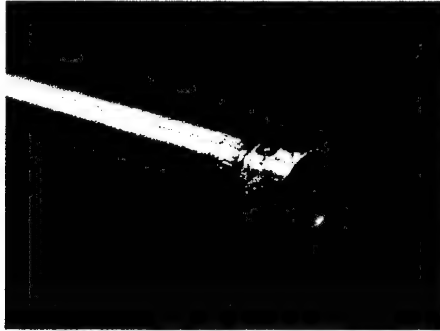


Figure 139. Completed sensor illustrating diaphragm retaining cap.

Sensor construction challenges

Several challenges were overcome during the first several attempts to construct a sensor. The first difficulty that was identified was the failure of the hermetic seal between the sapphire diaphragm and the Alumina tube. Temperatures generated during the welding process degraded the bond and caused micro holes in the bonding material. The initial solution for this was to place silver paste around the section of the Alumina tube where it encountered the sapphire diaphragm. The silver paste was then cured and the sensor re-checked. Luna researchers were able to seal the diaphragm assembly before the retaining cap was welded on. To alleviate this problem on future sensor constructions, the welding parameters were adjusted and more heat-sinking material was placed around the diaphragm. Several sensor housings have been manufactured since this process revision that maintains the hermetic seal without requiring the use of silver paste.

The second area for construction improvement came after the silver paste was cured in the high temperature kiln. Upon removal of the tube used to assist the insertion of the ferrule, the fiber suffered a failure at the point where it interfaced with the ferrule. Inspection of the tubing and the fiber revealed that burning of the polyimide coating on the fiber along with the phenylsalicilate bonded the fiber to the inside diameter of the stainless steel tubing. This was fixed by placing only the necessary section of the sensor tip containing the silver paste into the kiln, removing the polyimide coating from the heat affected zone and eliminating burn off of the coating.

The final issue causing sensor failure that has been addressed is the sensor failure during turbine engine testing. The first successful test of a working sensor allowed for data to be taken up to the point in which the sensor stopped responding. Disassembly of the sensor revealed that the fused ferrule had fracture at the point it was bonded into the sensor tip. It has been deduced that this was caused by excessive vibration of the sensor causing the ferrule to act as a cantilever beam, exceeding the fracture strength of the ferrule and causing failure. Figure 134 shows the tip of the ferrule after it had been removed from the sensor showing the breaking point. . This will be

addressed in the next development effort. Supports for the rear of the ferrule with respect to the sensor housing will be investigated.

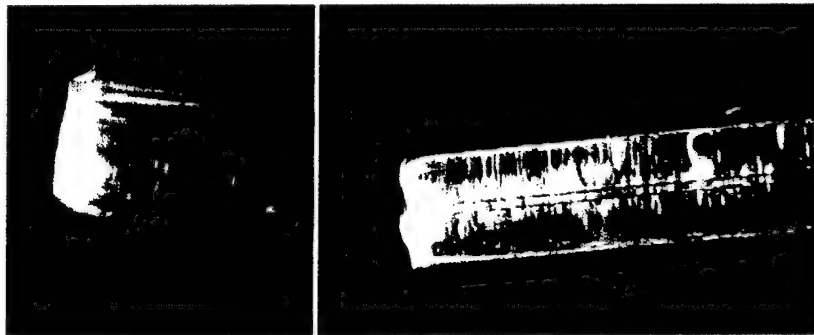


Figure 140. Broken ferrule from the first successful turbine test.

7. Sensor Testing

The combined project between Luna Innovations and Virginia Tech began March 1, 2003. The goal of the project was to test high temperature fiber-optic based sensors utilizing shock tube testing facilities, compressor inlet testing on an F109 turbine engine, and testing on a Pratt & Whitney JT-15D-1 engine. The shock tube is located in the cascade tunnel at Virginia tech, and the two engines are located at The Turbo Machinery and Propulsion Research Lab. The Garret F109, two spool, engine has a bypass ratio of 5:1, 30 blades in the first compressor stage, and it provides 1330 pounds of thrust. The JT-15D-1 Pratt and Whitney turbofan twin spool engine is capable of delivering up to 2200 pounds of thrust with a by-pass ratio of 3.3. The engine spool containing the first stage (high pressure) turbine (made up of 71 blades) has a design speed of 31,000 rpm. The engine was modified by Pratt and Whitney to accommodate pyrometers installed in custom ports for making dynamic surface temperature measurements at the high pressure turbine [Becker, 1988].

Temperature and Pressure measurements in the JT-15D-1

The modified wishbone section showing a typical pyrometer penetration is shown in Figure 141. The engine was altered to be able to harbor three pyrometer probes in custom ports at the three locations; port # 1 is shown in Figure 12. Locations 1 and 3 are 180° from each other; Location 2 is 45° from the vertical or 135° from location 3. Prior to testing of fiber optic probes two-temperature and one-pressure probes were used for this investigation to characterize the engine for the different test conditions. The assemblies mimic the pyrometer plugs (dummy probes) and are shown in Figure 13. The thermocouple (temperature) probes consist of 316 stainless steel tubes with an O/D of 0.352" and I/D of 0.27". The SS tube holds the thermocouple in the tubes and end caps are shown in Figure 14. The thermocouple probe end caps had the same thermal mass as the optical probes to be able to duplicate and measure the response time. The thermocouple wires (K type) from the two probes were connected to a temperature signal

conditioning module and were recorded continuously on a computer. The pressure probe end introduced in the engine was not sealed (with end caps) and pressure was measured through the other end using a 0 to 200 PSI digital pressure gage via a 1/16" stainless capillary tube. The pressure was recorded manually for every test condition.

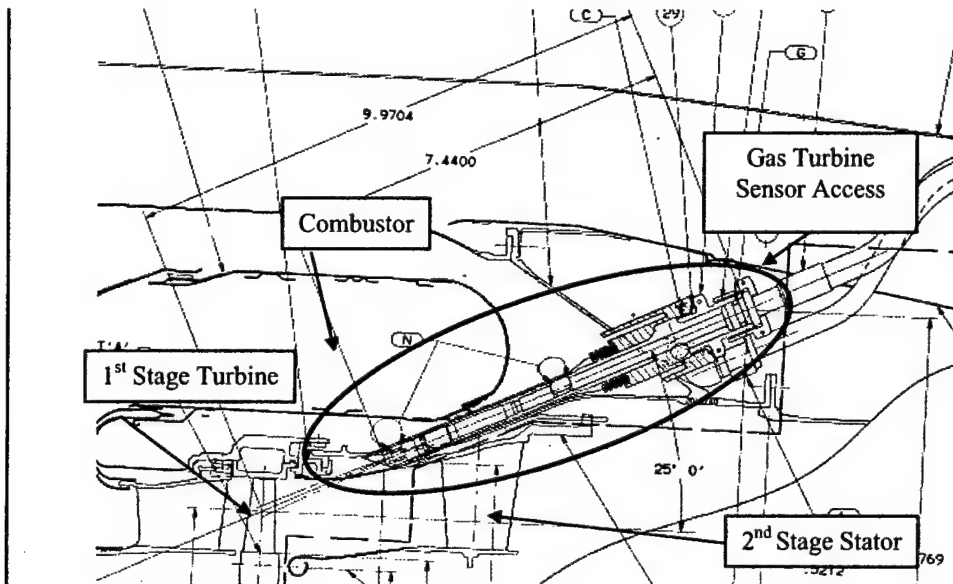


Figure 141 pyrometer installation for the JT-15D-1 engine [Pratt and Whitney, 1986]

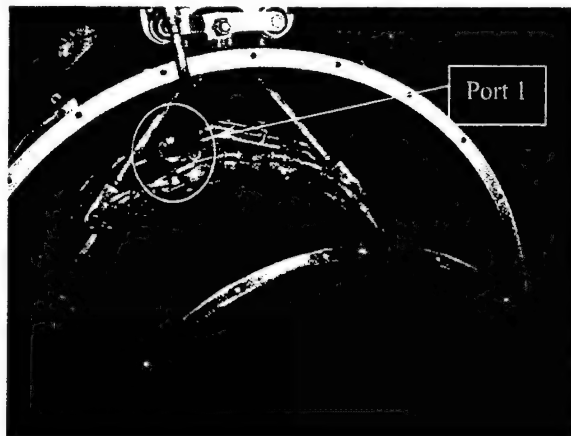


Figure 142: port 1 on the JT-15D-1 engine used for measuring temperatures and pressures in this investigation

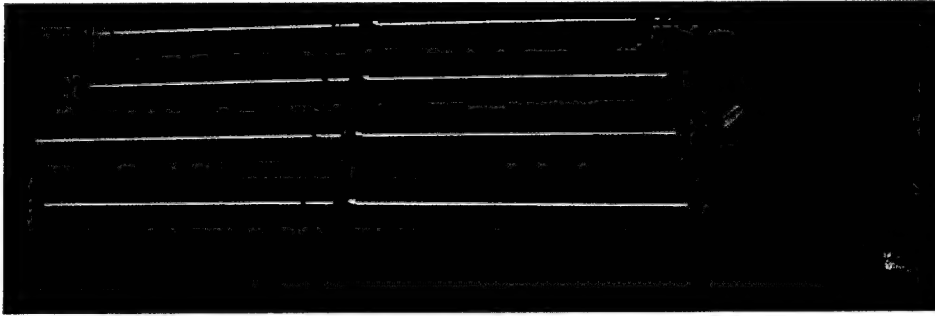


Figure 143: 3 temperature probes and one pressure probe (3 temperature probes were prepared to have one as a back up)

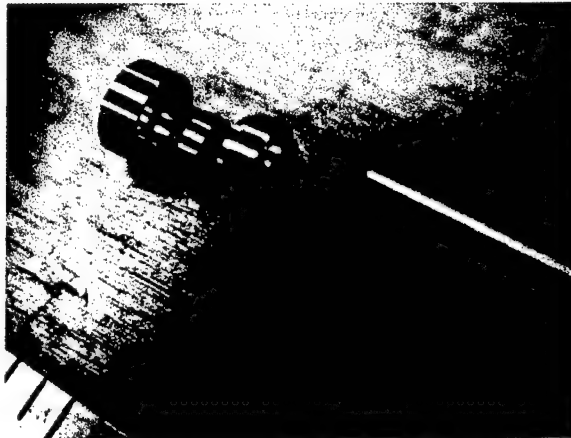
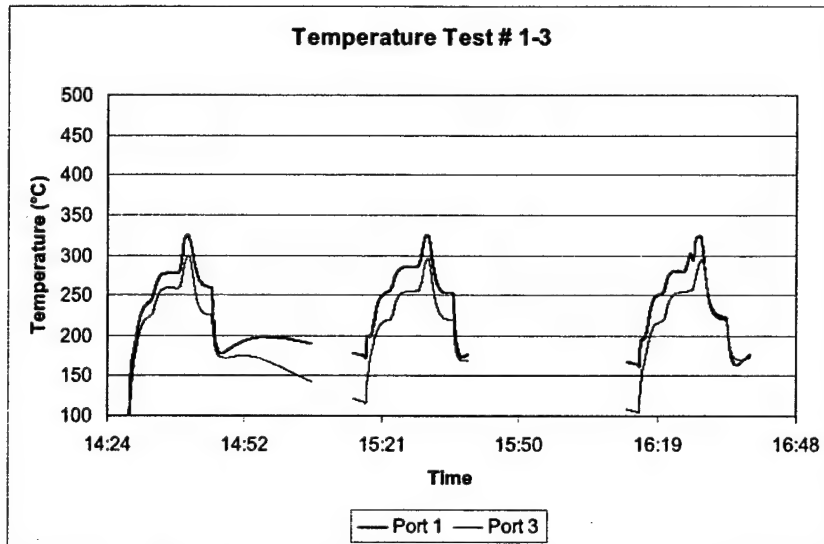


Figure 144: End caps for temperature probe along with thermocouple wire

The JT-15D-1 engine at Virginia Tech Airport is modified significantly leading to a limited operating speed of about 21,700 rpm or about 70 %. The preliminary tests consisted of starting the engine and running it till it achieved a constant temperature (warm-up), accelerating it to 60 % speed until steady temperatures were attained, increasing the engine speed to 70 % for a minute and then decreasing the speed back to 50 % before shut off. The engine was held at 50 % speed before shut off for about 5 minutes for it to cool down. The process was timed and was repeated for all subsequent runs.

The temperature probes were in ports at location 1 and 3 and the pressure probe was at location 2 for test numbers 1-3. The temperatures seen for the test numbers 1-3 are plotted in Figure 15 and show that they follow a consistent pattern with a peak of about 325° C for port 1 and about 300° C for port 3. The maximum pressure measured during the tests was about 5.4 PSI at 70 % speed.



145: temperature data at ports 1 and 3 for test numbers 1 thru 3

Capillary tubes were used during earlier testing [Becker, 1988] for calculating pressure required for cooling of pyrometer probes. Each port had two capillary tubes, one high and one low, thus giving a total of 6 capillary tubes. Figures 16a and 16b shows two such tubes, one flush with the engine (high pressure) and other connected to the pyrometer probe housing (low pressure). It was decided to measure the pressures at each of these 6 locations. The subsequent tests were performed with a pressure gage in port location specified in Table 1. During the capillary pressure measurement, the pressure probe installed in port number 2 was capped and the pressure gage was connected to the capillary tubes one at a time (all the other capillary tubes were capped). The engine was quickly ramped up to 70 % speed to record the peak pressure. Temperature data was also recorded during these tests.

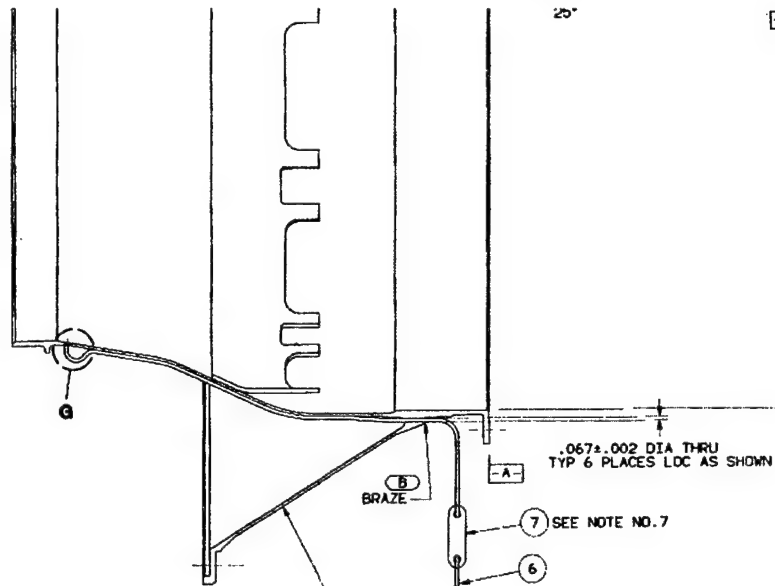


Figure 146: shows 1/16" capillary tube (no. 6) flush with the engine behind the high pressure turbine at location 'G' [Pratt and Whitney, 1986]

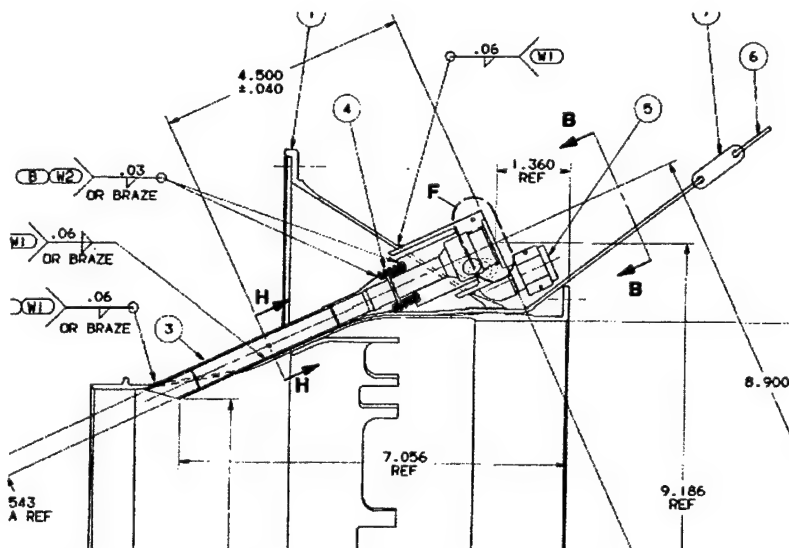


Figure 147: Illustrates 1/16" capillary tube (no. 6) connected to the pyrometer tube housing of one of the ports at low pressure location (section H-H) [Pratt and Whitney, 1986]

**Table 2 shows test matrix for experiments conducted at Virginia Tech from June 25 - July 8, 2004.
(Pressure probe and capillary tubes were capped when not connected to pressure gage)**

Test #	Temperature Probes	Pressure probe	Capillary Tube Pressure	Additional Comments
1	Ports 1 & 3	port 2	not measured	
2	Ports 1 & 3	port 2	not measured	repetition of test # 1
3	Ports 1 & 3	port 2	not measured	
4	Ports 2 & 3	port 1	not measured	
5	Ports 2 & 3	not measured	port 3 (low)	
6	Ports 2 & 3	not measured	Port 3 (low)	repetition of test # 5
7	Ports 2 & 3	not measured	Port 3 (high)	
8	Ports 1 & 2	port 3	not measured	
9	Ports 1 & 2	not measured	port 2 (low)	
10	Ports 1 & 2	not measured	Port 2 (high)	
11	Ports 1 & 2	not measured	port 1 (low)	
12	Ports 1 & 2	not measured	Port 1 (high)	
13	Ports 1 & 3 (extended probe)	port 2 (extended probe)	not measured	test aborted due to safety concern
14	Ports 1 & 3 (extended probe)	port 2 (extended probe)	not measured	

Test numbers 4-7 were done with temperature probes at locations 2 and 3 and pressure probe at location 1. The temperature measured during test numbers 4-7 are plotted in Figure 17 and show a peak of about 370° C at location 2. The peak pressure was again recorded to be about 5.7 PSI. During test 5 and 6 the pressure probe in port number 1 was capped and the pressure gage was attached to capillary tube leading to low pressure readings from port 3. The pressures measured at the capillary tubes were about 2.3 PSI. Test 7 measured pressure from high pressure capillary tube of port 3 which was about 20 PSI.

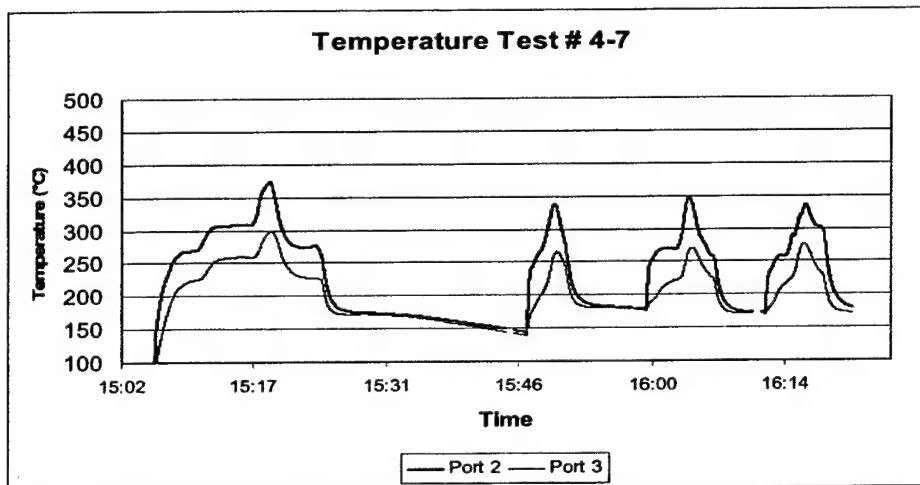


Figure 148: Temperature data at ports 2 and 3 for test numbers 4 thru 7

Tests 8-12 were done with temperature probes at locations 1 and 2 and pressure probe at location 3 and the results are plotted in Figure 18. The plots show a peak temperature for 70 % speed of about 370°C at location 2. The corresponding peak pressure was about 5 PSI. Test 9, 10, 11, and 12 measured capillary pressures at port 2; low pressure, high pressure and port 3; low pressure, high pressure, respectively. The pressures measured during these tests were about 5 PSI on the low side and between 7 and 9 PSI on the high side. These tests (# 1-12) were done with probes in initial position (about 2.5304" from the center of the blades at 60 % chord location) as shown in Figure 11.

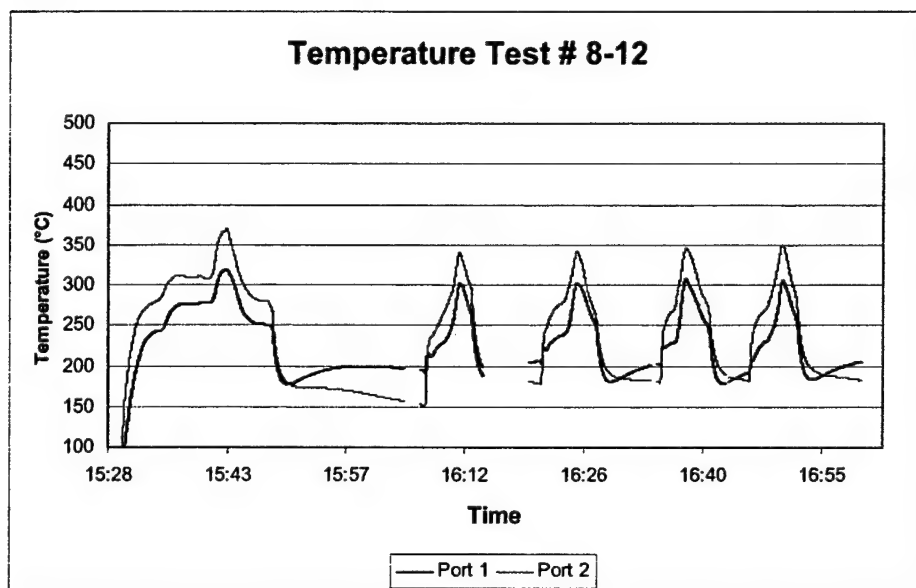


Figure 149: Temperature data at ports 1 and 2 for test numbers 8 thru 12

After looking at the results it was decided that to attain higher temperatures and pressures the probes needed to be extended in a hotter zone. The probe length was thus increased by 0.6" to be at the edge of the hole on the fishbone section seen in Figure 11. The engine was run for test numbers 13 and 14 with pressure probe at location 2 and temperature probes at locations 1 and 3. The temperatures in this extended probe position are plotted in Figure 19. They show an increase of about 100 °C from those seen in test # 1-3. The pressures measured were consistent with those seen in the previous tests (# 1-12). The temperature and pressure probes after the completion of the extended probe test (# 12-13) were observed to have additional soot/oxidation deposits. The soot deposit profile shown in Figure 20 was only seen where the probes extended out of the pyrometer tube housing, thus leading to the belief that the probes were exposed to the hot gases.

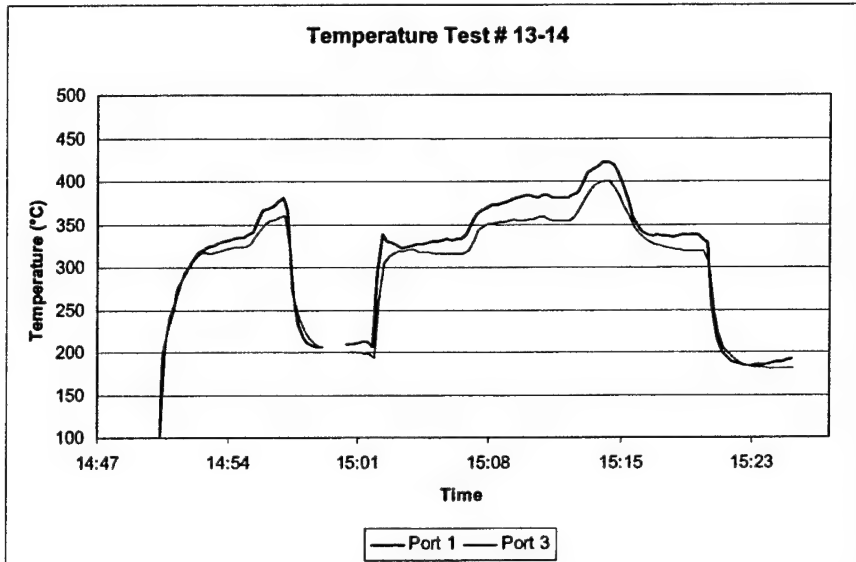


Figure 150: Temperature data at ports 1 and 3 for extended probe test (# 13 and 14). Test # 13 was aborted due to safety concerns

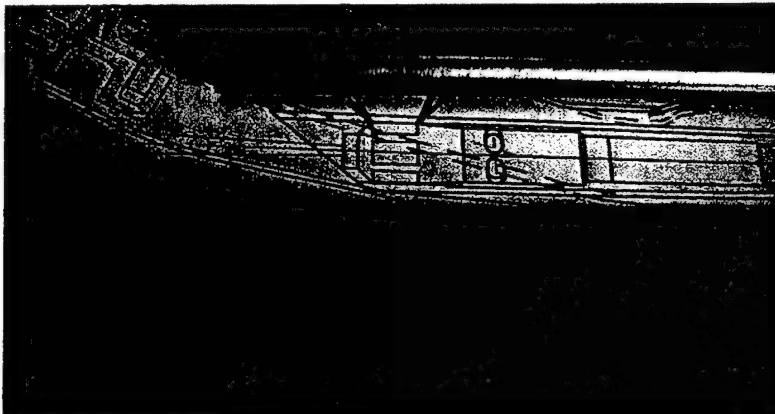


Figure 151: Soot deposit on the extended length of the probe outside the pyrometer housing

References

Becker W. A., "Dynamics Surface Temperature Measurements on the First Stage Turbine Blades in a Turbofan Test Engine Jet Rig," Masters of Science Thesis, Virginia Polytechnic Institute and State University, December 1988.

Jt-15D-1 Pyrometer Installation Drawings, Pratt and Whitney, Canada, 1986.

7.1 Fiber Optic Pressure Sensor Engine Testing

Testing with the fiber optic pressure probes was accomplished by inserting three identical probe housings consisting of one fiber-optic pressure probe, one static pressure probe, and one probe instrumented with a Type K thermocouple into the previously mentioned testing ports. The fiber-optic probe was located in the turbine as shown in Figure 153. The turbine was initially started and operated at 50% of its maximum operating speed for a period of six minutes in order to warm the engine. The turbine was then throttled to a maximum of 89% operating speed in increments of approximately 10% and run for 1 minute at each speed. Upon completion of the 89% run the turbine was allowed to cool at 50% and then testing was terminated by shutting down the turbine. Two one-second sets of data were recorded by the fiber-optic pressure probe, one static pressure data point was recorded, and the data from the thermocouple were logged at a frequency of 1 Hz. The engine speeds are shown below in Figure 152. The data were then removed to the Luna facility in Blacksburg, Va. for further analysis by the Luna testing and design team.

For this engine, the low pressure spool (or Rotor1) maximum speed is 16,000 rpm and the 1st stage turbine has 61 blades, so the maximum blade passing frequency is 16,267 Hz. The low pressure spool (Rotor 2) has a maximum speed of 31,000 rpm, 71 turbine blades and a maximum blade passing frequency of 36,683 Hz.

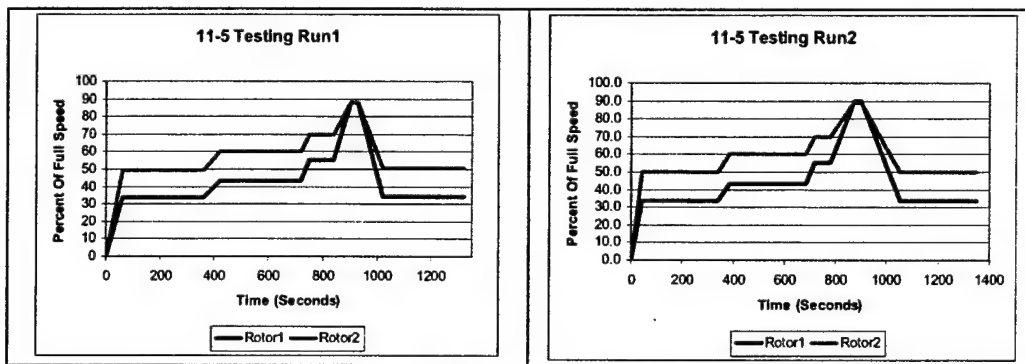


Figure 152. Engine Speed vs. Time for Both Trials

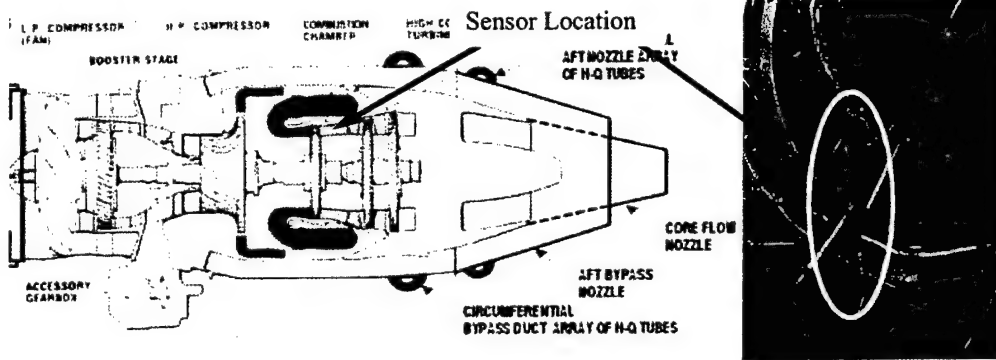


Figure 153. Fiber-Optic probe location during testing.

7.2 Results

Luna Innovations was able to design and build a high temperature fiber-optic sensor and use it to interrogate a Pratt and Whitney JT-15-D gas turbine engine in an attempt to measure the pressures corresponding to the rotor blade passing frequency. Upon completion of the testing it was observed that the sensor had failed. Evaluation of the data revealed that this did not occur until the time after the cool-down period for the turbine. Evaluation of the data has also shown that the resonating frequency of the sensor chamber, manufactured by Pratt and Whitney, was captured making interpretation of the blade passing frequency impossible from this test data. The temperature data logged over the time of the experiment is represented in Figure 154 showing the increase seen by the sensor at each engine speed. Figure 155 compares the temperature and static pressure data for each increase in engine speed. Dynamic pressure data was measured by the fiber-optic sensor for all engine speeds. A section of this data is shown in Figure 156 that was taken during the 89% test run. At all engine speeds analysis of the data in the form of a FFT plot revealed a frequency at 8400 Hz (shown in Figure 157 for the 89% throttle speed.) This frequency corresponds to the calculated resonance of the sensing chamber.

Upon evaluation of the test data the fiber-optic pressure sensor was inspected in order to determine the cause of the failure that occurred during testing. Initial inspection of the sensor revealed no obvious material failures. The swagelok fittings at the center of the sensor were loosened and the outer housing of the sensor was removed. This allowed for the internal sensor components to be inspected (shown in Figure 158) revealing that the ferrule assembly had cracked at its interface with the Kovar tip. It was determined that the reason for this failure was the vibration load that the sensor underwent as a result of the testing. The ferrule assembly extended approximately 1 1/2" beyond the end of the Kovar tip and acted as a cantilever beam. The forces induced on the beam during testing exceeded the material strengths of the fused silica ferrule causing the ferrule to crack. Future sensor iterations will account for this and will be constructed with a support for the ferrule.

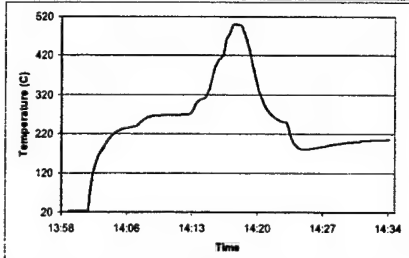


Figure 154. Approximate sensor temperature profile during test with an elevation visible at each engine setting change.

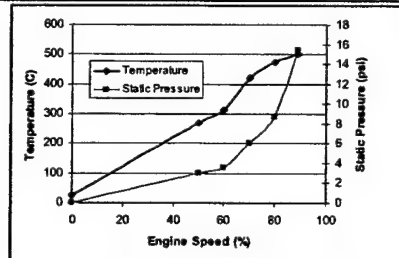


Figure 155. Engine static pressure and ITT temperature for each speed setting during test.

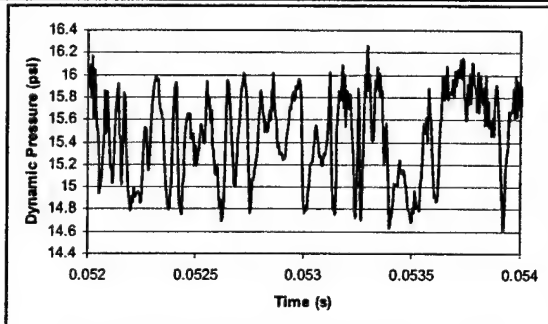


Figure 156. Pressure vs. time for 89% engine speed setting.

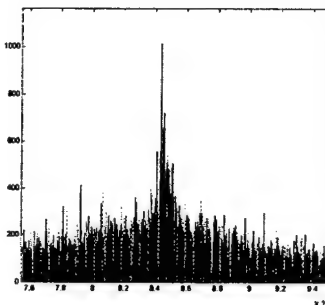


Figure 157. FFT of pressure signal for 89% engine speed.

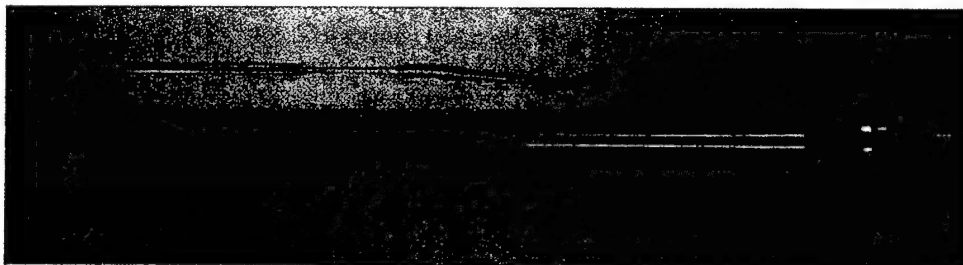


Figure 158. Sensor with fiber optic components removed

7.3 Second fiber optic pressure sensor testing

A second fiber optic pressure sensor (FO-2) was constructed and tested in the JT-15D turbine engine at Virginia Tech. This sensor was constructed in similar fashion as the first fiber optic

pressure sensor. However, for this sensor the tube that was used to insert the ferrule assembly was permanently bonded to the ferrule and to the sensor housing. The goal of this was to remove the vibrational load from the ferrule assembly. This sensor was installed into the Pratt & Whitney JT-15D and tested using the seam procedures as the first fiber optic pressure sensor.

Results

FO-2 survived three test runs in the JT-15D turbine engine without failure of the optical components or loss of optical signal. During all three runs the turbine was ramped up to approximately 90% and ramped down to the stop position. Data was taken for all three runs and evaluated using the Hyperscan software and Matlab code written for Hyperscan data evaluation. Inspection of the data and the sensor revealed that the sensor was thermally sensitive. The degree to which the sensor gap changed as a result of temperature was at a magnitude that yielded the initial calibration data void for operating conditions.

By taking the processed data sets from the third run, the FFT plots could be generated in Matlab for each data segment. Using the plots in the frequency domain the data shows the dominant amplitudes of pressure change.

While difficult to see, as the sensor data has significant thermally induced errors, the data from the second sensor shows correlation of frequency content with the approximate 1st stage turbine blade passing frequency. The Fourier transform data sets show that the peak frequency of fluctuation from the sensor increases with increasing engine speed. It is not likely that the sensor signal is due to vibration amplified by the design and testing.

Finally, the sensor was still very sensitive and operational at the beginning of the third test. Data was collected from the sensor during the engine start procedure, as can be seen in Figure 160. The sensor, still warm from test run 2, cooled during the start procedure as the rotors were spun up to start speed, then the sensor signal changed rapidly after ignition commenced. What is really interesting is that the sensor was able to capture the pressure signals from the surface discharge ignitors during the start procedure. The sensors show a small pressure signal that correlates well with the audible sparking sounds coming from the engine at start up. Those signals disappear after ignition. Careful examination of the raw sensor data from the two Hyperscan lasers confirms that the sensor output is due to a real pressure signal and not due to electromagnetic interference (EMI) being picked up by the electronics. As can be seen in Figure 159, the sensor return from channel 2, the green trace, increases in baseline level while the "spark" pressure signal is decreasing in amplitude. The spark signal in channel 1 stayed relatively constant during this time.

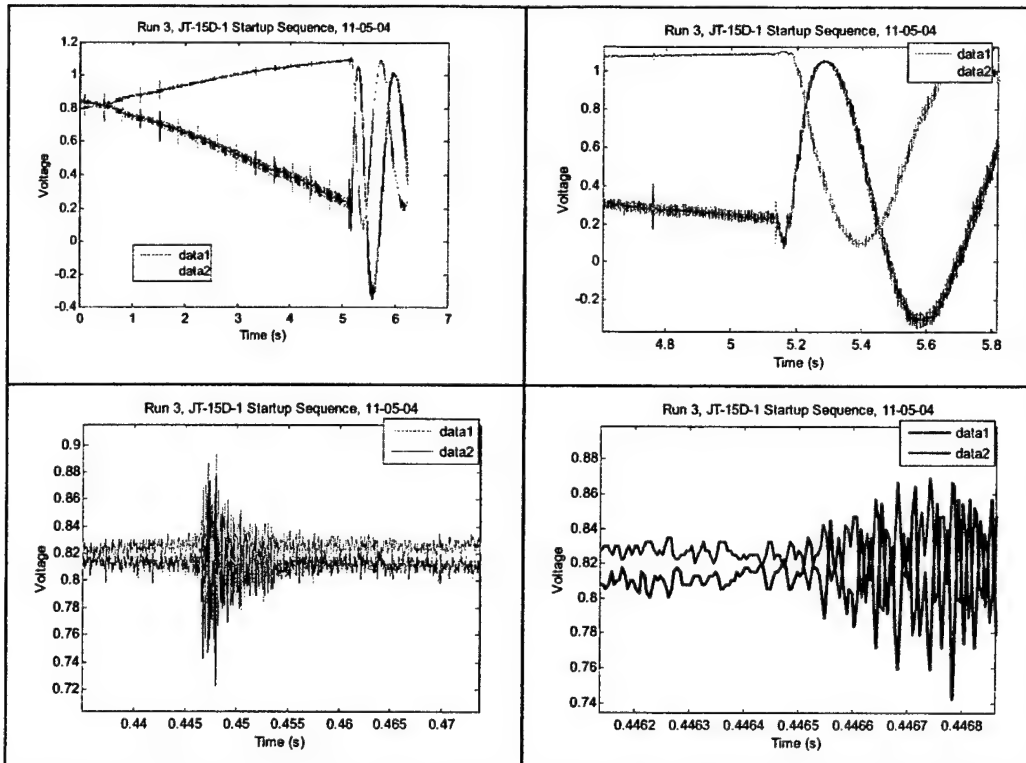


Figure 159. Raw Data from Hyperscan showing Pressure pulses at engine start up

As reported in section 3.1, the Hyperscan combines two single channel fiber instruments to eliminate directional ambiguity in the sensor measurement and to linearize and eliminate the insensitive region where the fringe reaches its maximum and changes direction. The insensitive region in the instrument readout is due to the nonlinear (sinusoidal) transform of sensor gap into optical signal amplitude.

Observation of the raw sensor data from the start-up sequence of the P&W JT-15D-1 engine shows that the raw data from laser 2 approaches the fringe turnaround point as the sensor cools back down. At the same time, the sensor “spark” signal decreases in channel 2 while staying relatively constant in channel 1. The observed signal change is consistent with the expected optical signal attenuation of a real pressure signal from the sensor. Further arguments can be made that a single detector and amplifier are used to convert the sensor optical return signal to electrical voltage from both lasers, so the relative signal amplitude due to EMI would not change between channels at any time.

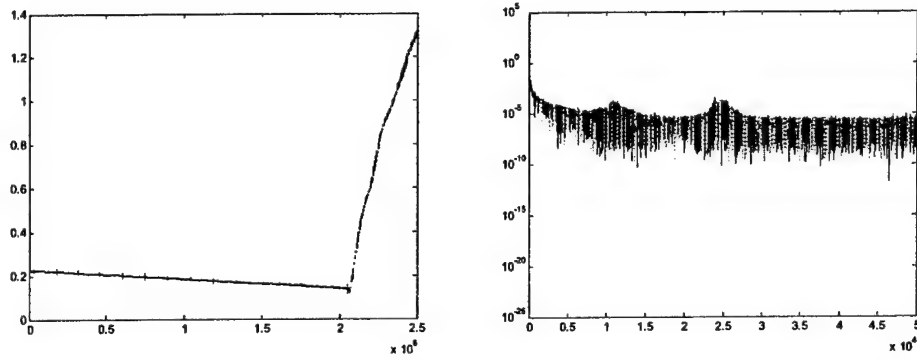


Figure 160: Run3 Ramp_CH1 processed gap and Run3 Ramp_CH1 processed fft

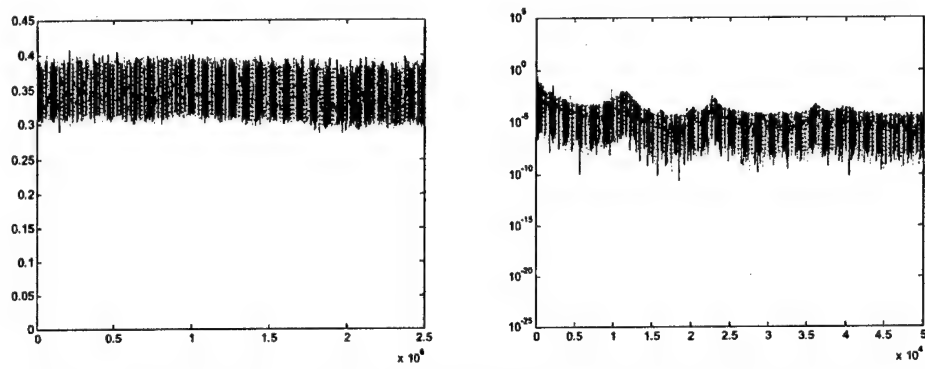


Figure 161: Run3 Scan-1 50%_Ch1processed gap and Run3 Scan-1 50%_Ch1processed fft

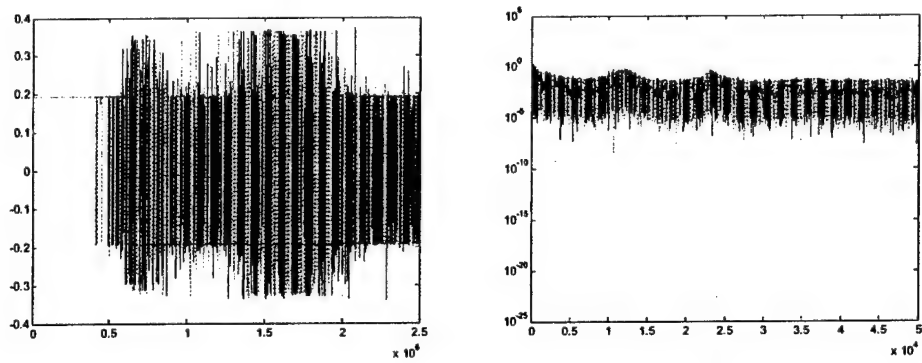


Figure 162: Run3 Scan-2 53%_Ch1processed gap and Run3 Scan-2 53%_Ch1processed fft

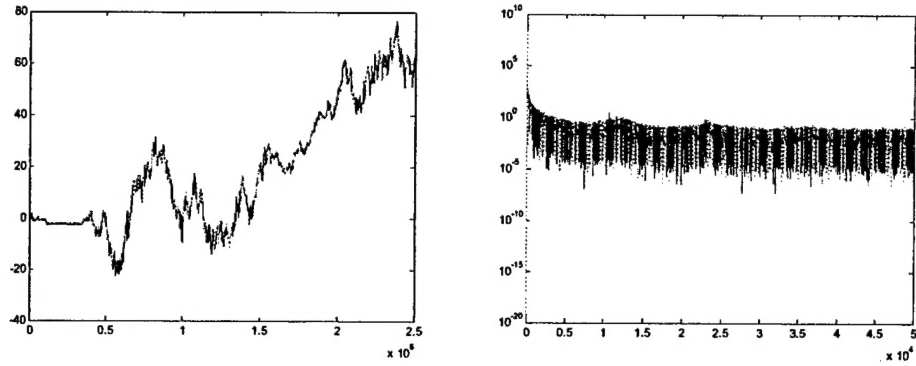


Figure 163: Run3 Scan-3 56%_Ch1processed gap and Run3 Scan-3 56%_Ch1processed fft

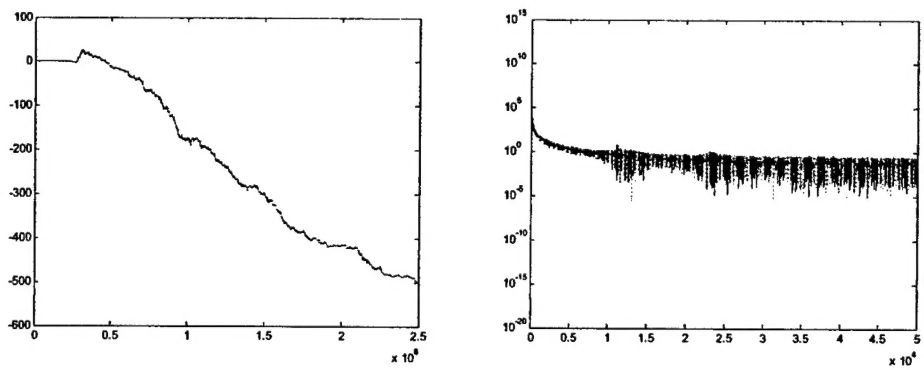


Figure 164: Run3 Scan-4 59%_Ch1processed gap and Run3 Scan-4 59%_Ch1processed fft

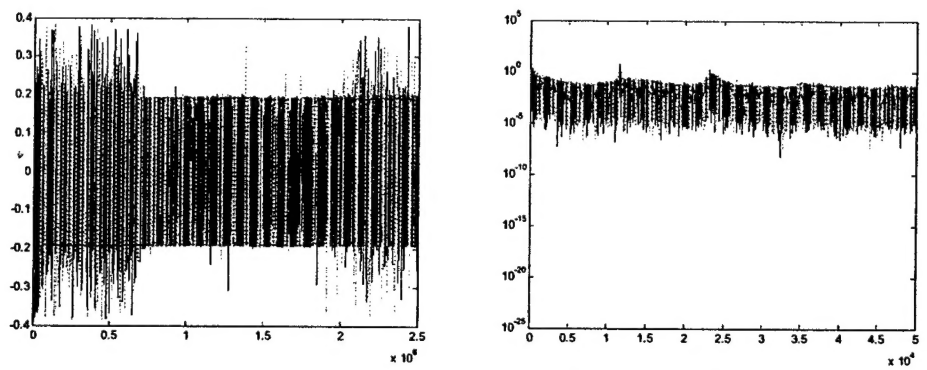
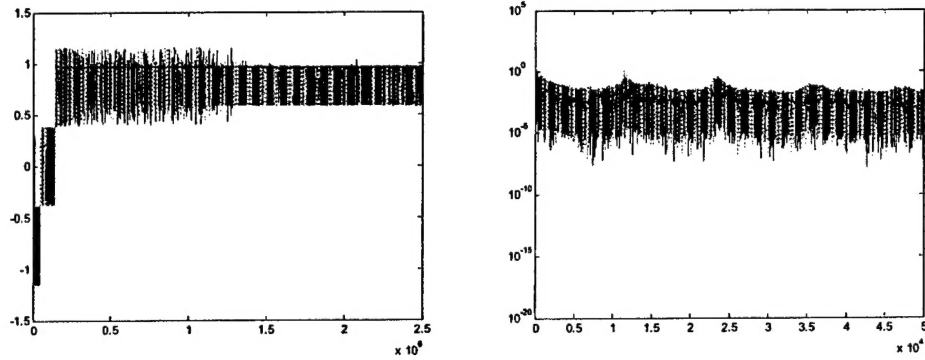


Figure 165: Run3 Scan-5 60%_Ch1processed gap and Run3 Scan-5 60%_Ch1processed fft



166: Run3 Scan-6 RD%_Ch1processed gap and Run3 Scan-6 RD%_Ch1processed fft

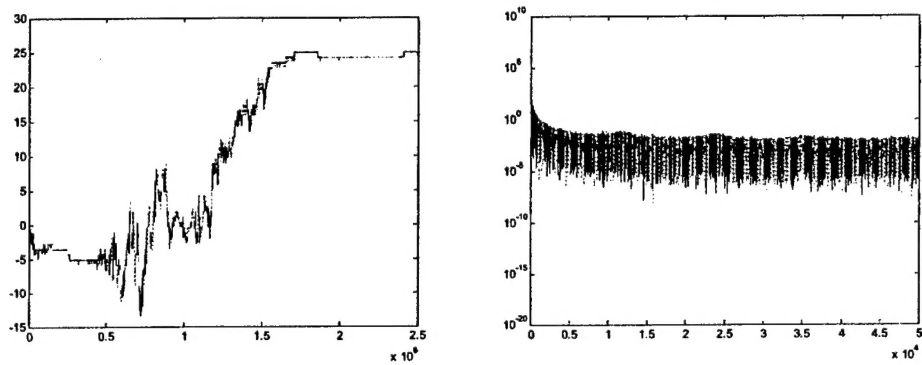


Figure 167: Run3 Scan-7 RD50%_Ch1processed gap and Run3 Scan-7 RD50%_Ch1processed fft

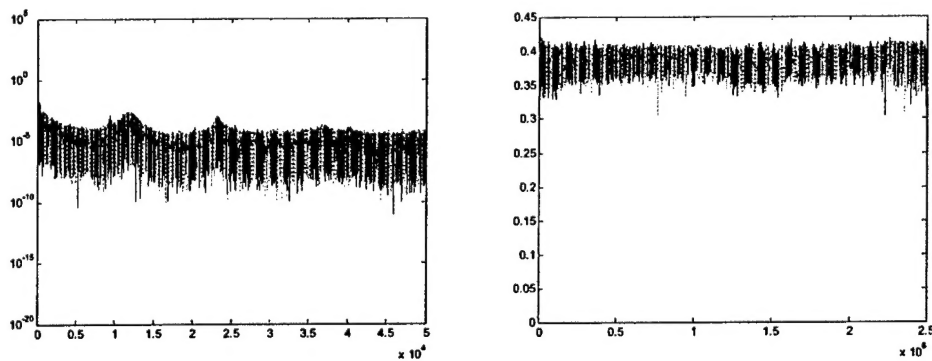


Figure 168: Run3 Scan-8 RD46%_Ch1processed gap and Run3 Scan-8 RD46%_Ch1processed fft

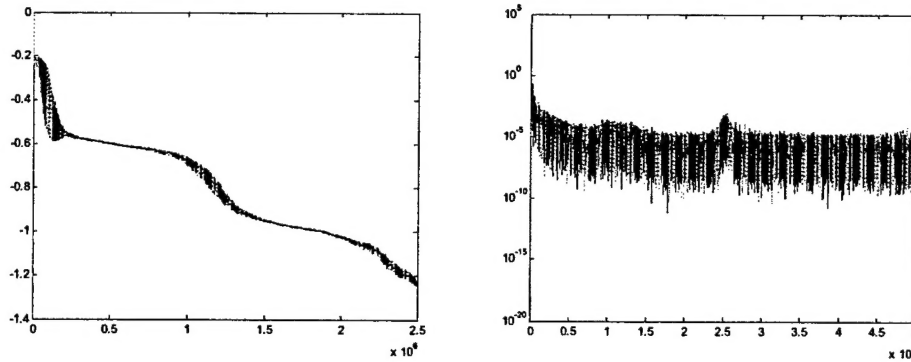


Figure 169. Run3 Scan-9 DeCel to stop_Ch1processed gap and Run3 Scan-9 DeCel to stop_Ch1processed fft

Sensor Post-Testing Evaluation

After the sensor has been tested in the turbine engine at Virginia Tech it was evaluated for the effects of variance due to vibration. The sensor was mounted on a vibration exciter and shaken at various gravitational levels while pressure data was taken using the Hyperscan system. Two frequencies of vibration appeared in the data. The lowest frequency can be attributed to the control valve on the pressure supplying unit while the high frequency is a result of the sensor being vibrated. The sensor was tested at only 10, 100 and 1000 Hz, and appears to hit its vibration resonance frequency around 100 Hz (shown in Figure 171), a frequency seen during the operating turbine tests. This seems to explain the highly noisy data captured during the second gas turbine test.

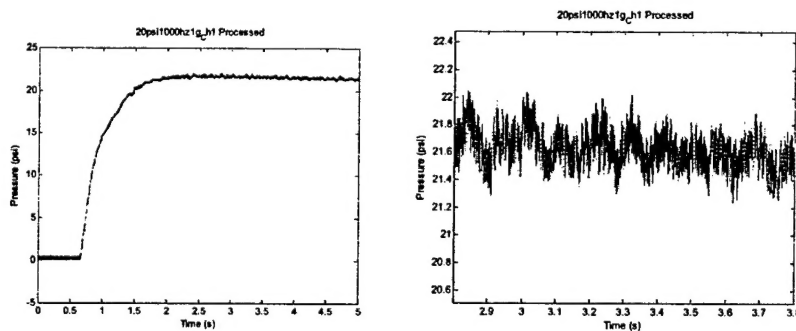


Figure 170 Sensor shaken at 1 G and 1000hz

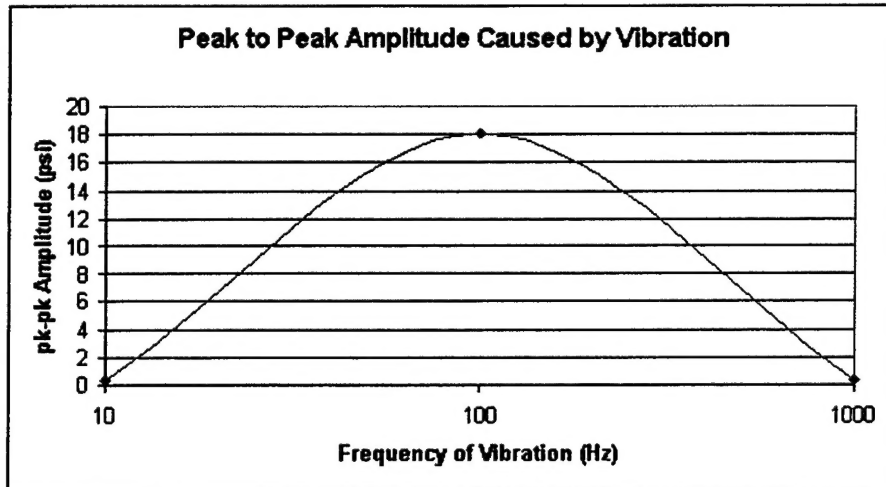


Figure 171. Peak to Peak Vibration amplitudes for post sensor testing

8. Conclusion

Luna Innovations and Virginia Tech have successfully completed this Phase II development effort. Luna and Virginia Tech have completed successful measurement of pressure within a gas turbine engine at temperatures exceeding 500 °C. In addition, Luna Innovations and VT have measured blade passing frequencies to an accuracy of better than 99% using fiber-optic sensors and instrumentation. Luna has shown that the sensor technology is capable of surviving at temperatures approaching 1400 °C and has shown pressure measurements of 500 psi at temperatures of 850 °C.

i. A. Ezbi and R. P. Tatam, "Passive signal processing of miniature Fabry-Perot interferometric sensors using a dual wavelength source," *10th Optical Fibre Sensors Conference*, pp. 335-338, 1994.